

POLITECNICO DI TORINO

Corso di Laurea Magistrale in

INGEGNERIA ENERGETICA E NUCLEARE

Master Thesis

TRIEX-II: modeling and qualification of a GLC mock-up for
HCLL/WCLL TBS of ITER



Advisor
prof. Massimo Zucchetti

Candidato
Edoardo Galli

Co-advisors
Eng. R. Testoni
Eng. L. Candido
Eng. M. Utili

Anno Accademico 2018/2019

SOMMARIO

La tesi ha lo scopo di caratterizzare sia dal punto di vista numerico sia dal punto di vista sperimentale, la tecnologia Gas Liqui Contactor - packed column proposta per l'estrazione del trizio nei reattori a Fusione. La caratterizzazione sperimentale è stata svolta con il supporto dell'impianto TRIEX-II presso il C.R. Brasimone. Questa tecnologia viene impiegata nei design del Breeding blanket di tipo HCLL e WCLL. Ai fini di analizzare dal punto di vista numerico l'efficienza di estrazione è stata eseguita una simulazione 2-D dove sono stati presi in esame i sensori a permeazione, impiegati per la misura della concentrazione nel breeder, e i principali componenti dell'impianto TRIEX-II. Per i sensori a permeazione è stata fatta una simulazione di trasporto. Per il saturatore, impiegato per solubilizzare l'idrogeno nella lega eutettica Pb-15.7Li utilizzata come breeder dell'HCLL e WCLL, e per il GLC è stata fatta prima un'analisi di tipo CFD per valutare le cadute di pressione e il profilo di velocità, che successivamente è stata integrata al modello di trasporto. Dopo di che grazie alla campagna sperimentale condotta da ENEA C.R. Brasimone, per valutare l'efficienza di estrazione delle packed column, è stata fatta la validazione delle simulazioni precedentemente sviluppate.

ABSTRACT

The Water-Cooled Lithium-Lead Test Blanket Module of ITER and the respective breeding blankets of DEMO needs to be efficiently characterized from the point of view of hydrogen isotopes inventory in Pb-15.7Li with an *in-situ* detection, in order to guarantee tritium self-sufficiency and to control the radiological hazards towards the external environment. In this framework, a reliable hydrogen isotopes permeation sensor is required both for tritium management at the several steps of the reactor fuel cycle and for the monitoring of tritium processing systems. One of the most complicate system of Pb-16Li loop is the Tritium Extraction system, from this points of view, an experimental facility, called TRIEX-II, was installed at C.R. ENEA Brasimone in order to qualify the main technologies devoted to extract hydrogen isotopes from the eutectic alloy. The technology analysed in this work is the Gas/Liquid Contactors, in particular the packed column. The experimental campaign on TRIEX-II facility has been carried out from mid-April to mid-June 2019.

In this thesis work, first of all the permeation sensors installed in TRIEX-II have been modelled in liquid phase condition, because the sensor is immersed in isothermal lithium-lead. Then, the permeation sensors have been characterized comparing experimental and modelling results.

Secondly, numerical models of saturator and extractor have been also implemented. The CFD analysis of these two components has been carried out, then the transport phenomena have been set up. Finally, the validation between numerical and experimental data has been performed.

ACKNOWLEDGMENTS

This turns out to be a more meaningful moment. This space gives me the opportunity to reflect on this experience and especially makes me reflect on the people who gave me the opportunity to participate in this experience and who have supported me throughout the time. Many thanks to my thesis advisor, Prof Massimo Zucchetti, for giving me the opportunity of this certainly very formative experience. I am grateful to my Co-Advisor, Eng Marco Utili, for having me first of all hosted at the research center ENEA C.R. Brasimone and for having guided me in the field of scientific research. I express my warm thanks to Eng. Luigi Candido for guiding me throughout the thesis project and assuring me both from the formative and moral point of view. Many thanks to Eng. Raffaella Testoni for having assisted me especially during the period of writing the thesis Perhaps the greatest thanks go to my family who allowed me with many sacrifices to live this experience and who supported me during difficult times. Last but not least a big thank you goes to all the technicians with whom I collaborated for the implementation of the facility TRIEX-II, and to my old roommate and deadbeat friend singer without whom this experience would have been much harder.

CONTENTS

Introduction	13
1 Nuclear fusion reactors	15
1.1 ITER.....	19
1.2 DEMO	20
1.3 Comparison between ITER and DEMO.....	21
2 Tritium extraction system from lead-lithium	22
2.1 Tritium extraction technologies for lead-lithium	26
2.1.1 PAV	26
2.1.2 GLC (Gas-Liquid Contactor)	27
2.2 Comparison between PAV and GLC	31
3 Design of a GLC-packed tower	32
3.1 Diameter.....	32
3.2 Height	33
3.3 Alternative method	33
3.4 Sizing.....	35
3.4.1 Main calculations	35
4 TRIEX-II facility.....	36
4.1 TRIEX and TRIEX-II facilities	36
4.2 Main components of TRIEX-II.....	37
4.2.1 Permanent magnet pump	38
4.2.2 Thermal mass flow meter	40
4.2.3 The storage tank.....	41
4.2.4 The Saturator.....	42
4.2.5 The gas injection system	43
4.2.6 The extractor	44
4.2.7 Permeation sensors.....	45
4.3 The gas system	46
4.3.1 The gas system Piping and instrumentation diagram	46
4.3.2 Vacuum system	47
4.3.3 The hydrogen generator	50
4.3.4 Mass Flow Controllers.....	51
4.3.5 Mass spectrometer	52
4.4 Differential pressure transducers	54

4.5	Pb-15.7Li valves	55
4.6	Thermocouples.....	56
5	Permeation sensors.....	57
5.1	Physical principles of permeation sensors	57
5.2	Design of permeation sensors.....	58
5.3	Liquid phase model description	62
5.3.1	Initial conditions.....	63
5.3.2	Boundary conditions	63
5.3.3	Mesh choice	64
5.3.4	Transport properties	65
5.3.5	Parametric analysis Sieverts' constant.....	65
5.3.6	Surface-to-Volume (S/V) ratio.....	67
5.3.7	Parametric analysis of the temperature	68
5.3.8	Sensor wall thickness	69
5.3.9	Parametric analysis of the Pressure	70
5.4	Verification of the model	71
5.4.1	The Experiment of 15 th April 2019	71
5.4.2	The experiment of 7 th - 8 th May	73
5.5	Experimental analysis.....	74
5.5.1	Evaluation of the extraction efficiency with the permeation sensors.....	74
6	Simulation of the saturator and extractor	77
6.1	CFD analysis of the extractor	77
6.1.1	Model description	77
6.1.2	Initial and boundary conditions	78
6.1.3	Mesh.....	79
6.1.4	Grid independence.....	80
6.1.5	Validation of CFD model.....	83
6.2	Transport analysis	86
6.2.1	Transport model description of the extractor and the saturator	86
6.2.2	Initial conditions.....	88
6.2.3	Boundary conditions	88
6.2.4	Validation of tritium transport model.....	88
	Conclusion.....	92
	Bibliography	94

LIST OF FIGURES

Figure 1 – Tokamak reactor [3].....	15
Figure 2 – Stellarator reactor [4].....	16
Figure 3 – θ pinch, z-pinch, spheromak magnetic confinement [7], [8], [9].....	17
Figure 4 – Road maps of the ITER and DEMO projects [12].....	18
Figure 5 – Fuel cycle in a fusion reactor [19].....	22
Figure 6– Phase diagram of Pb-Li [21].....	23
Figure 7 – Modul of WCLL breeding blanket configuration [23].....	24
Figure 8 – Modul of DCLL breeding blanket configuration [24].....	24
Figure 9 – Modul of HCLL breeding blanket configuration [24].....	25
Figure 10 – Scheme of the PAV system [26].....	26
Figure 11 – Different typologies of Gas Liquid Contactors [28].....	27
Figure 12 – Scheme of babble column [30].....	28
Figure 13 – Scheme of packed column whit an example of a structured packing [31].....	29
Figure 14 –Operating scheme of the pocked tower [25].....	30
Figure 15 – Concertation trend at the liquid-gas interface [25].....	33
Figure 16 – Graphically trend of m_{GM}/L_M [25].....	34
Figure 17 – The layout of the old TRIEX facility.....	36
Figure 18 – The layout of the upgraded TRIEX-II facility.....	37
Figure 19 – Permanent Magnet Pump.....	38
Figure 20 – Characteristic curve of the pump.....	39
Figure 21 – Thermal mass flow meter [35].....	40
Figure 22 – Storage tank.....	41
Figure 23 – Saturator tank.....	42
Figure 24 – The Mellapak 452/ structured packing.....	42
Figure 25 – Gas injection system.....	43
Figure 26 – Extractor tank.....	44
Figure 27 – Pressure sensor.....	45
Figure 28 – P&ID of the gas system.....	46
Figure 29 – View of the two skids. On the left: skid A; on the right: skid B.....	47
Figure 30 – Pfeiffer 80 Turbo vacuum station.....	48
Figure 31 – Edwards EV12 Vacuum pump.....	49
Figure 32 – View of the hydrogen generator.....	50
Figure 33 – View of the Bronkhorst mass flow controller [34].....	51
Figure 34 – Front view of the mass spectrometer.....	52
Figure 35 – View of the differential pressure transducer.....	54
Figure 36 – View of the Pb-15.7Li valve.....	55
Figure 37 – Type K thermocouples [36].....	56
figure 38 – permeation process through a membrane [18].....	57
Figure 39 – Cylindrical sensor of TRIEX.....	59
Figure 40 – On the left: final configuration of TRIEX II permeation sensor; on the right: matrix to build the helixes.....	59
Figure 41 – Helical sensor.....	60
Figure 42 – Swagelok connection of 1/8".....	60
Figure 43 – Cross connection with the permeation sensors.....	61
Figure 44 – Whole domain of the simulation.....	62
Figure 45 – Mapped mesh.....	64
Figure 46 – Pressure trend of the Sieverts' constant.....	66
Figure 47 – S/V trend.....	67
Figure 48 – Pressure trend with temperature sweep.....	68
Figure 49 – Pressure trend with thickness sweep.....	69
Figure 50 – S/V trend with pressure sweep.....	70
Figure 51 – Comparison between the theoretical trend with the Experimental value.....	72
Figure 52 – Comparison between the theoretical trend with the Experimental value.....	73

<i>Figure 53 – The trend of the permeation sensors.</i>	75
<i>Figure 54 – Trend of the permeation sensors.</i>	76
<i>Figure 55 – Implemented domain for the extractor, in the zoom there is a structured filling.</i>	78
<i>Figure 56 – Mesh zoom of the extractor.</i>	79
<i>Figure 57 – Grid convergence index.</i>	82
<i>Figure 58 – Speed calculated with different meshes.</i>	82
<i>Figure 59 – Pressure drop trend of the extractor.</i>	83
<i>Figure 60 – Validation of the simulation.</i>	84
<i>Figure 61 – Velocity field at the inlet [m/s]: on the left $L=0.68$ kg/s, on the right $L = 4.25$ kg/s.</i>	85
<i>Figure 62 – Velocity field at the outlet [m/s]: on the left $L=0.68$ kg/s, on the right $L = 4.25$ kg/s.</i>	85
<i>Figure 63 – Geometry of the saturator on the left and of the extractor on the right.</i>	86
<i>Figure 64 – Validation of the saturator.</i>	89
<i>Figure 65 – All inventory of the Saturator.</i>	90
<i>Figure 66 – Validation of the extractor.</i>	91

LIST OF TABLES

<i>Table 1 – Mean parameters of the stellarator reactor [6].</i>	16
<i>Table 2 – Main parameters of ITER [14], [15], [11].</i>	19
<i>Table 3 – Main parameters of DEMO [16].</i>	20
<i>Table 4 – Main difference between ITER and DEMO [17].</i>	21
<i>Table 5 – Main difference between PAV and GLC [22], [32].</i>	31
<i>Table 6– Main input parameter.</i>	35
<i>Table 7– Initial calculations.</i>	35
<i>Table 8 – Main characteristics of the permanent magnetic pump.</i>	38
<i>Table 9 – Thermal flow meter main characteristics [34].</i>	40
<i>Table 10 – Main parameters of the storage tank.</i>	41
<i>Table 11 – Main design parameters of the saturator.</i>	43
<i>Table 12 – Main design parameters of the extractor.</i>	44
<i>Table 13 – Design Characteristics of the pressure transducer Pfeiffer CMR-372.</i>	45
<i>Table 14 – Main characteristics of a molecular vacuum station.</i>	48
<i>Table 15 – Main characteristics of a rotative vacuum pump.</i>	49
<i>Table 16 – Operative parameters of the hydrogen generator.</i>	50
<i>Table 17 – Main characteristics of the mass flow controller.</i>	51
<i>Table 18 – Main characteristics of the mass spectrometer.</i>	53
<i>Table 19 – Operative Characteristics of the pressure transducer.</i>	54
<i>Table 20 – Characteristics of the Pb-15.7Li valve.</i>	55
<i>Table 21 – Main parameters of the cylinder sensor.</i>	59
<i>Table 22 – Main parameters of the three helices.</i>	60
<i>Table 23 – Preliminary properties for the simulation.</i>	65
<i>Table 24 – Sievert’s constant of H in Pb15.7Li [39]</i>	65
<i>Table 25– Value of t^* changing the Sieverts’ constant.</i>	66
<i>Table 26 – Value of t^* changing S/V ratio with the mass balance error.</i>	67
<i>Table 27 – Value of t^* changing the temperature.</i>	68
<i>Table 28 – Value of t^* changing the sensor thickness.</i>	69
<i>Table 29 – Value of WH changing pressure.</i>	70
<i>Table 30 – Value of t^* changing pressure and S/V ratio.</i>	71
<i>Table 31 – Error Values.</i>	72
<i>Table 32 – Errors values.</i>	73
<i>Table 33 – Initial values of the experiment.</i>	74
<i>Table 34 – Initial values of the experiment.</i>	75
<i>Table 35 – Initial conditions values.</i>	78
<i>Table 36 – Boundary conditions.</i>	78
<i>Table 37 – Chosen parameters for the estimation of Δy.</i>	79
<i>Table 38 – Main values for the skewed angle.</i>	80
<i>Table 39 – Test matrix for the characterization of the extractor.</i>	83
<i>Table 40 – Comparison between the simulation and experiment.</i>	84
<i>Table 41 – Errors results.</i>	89

Introduction

The aim of this thesis is to model and qualify the Gas/Liquid Contactors mock-up for HCLL/WCLL TBS of ITER. In particular, an experimental tritium extraction facility, TRIEX_II, has been built in C.R. ENEA Brasimone to qualify the extraction efficiency of the Gas/Liquid Contactors, the packed column technology. The experimental campaign on TRIEX-II facility has been followed and the results obtained have been analysed, in order to qualify the packed column configuration. In addition, the model of permeation sensors, extractor and saturator have been developed and have been compared with the experimental data to validate them.

In chapter 2, the breeding blanket design WCLL, HCLL, DCLL are analysed. Additionally, Tritium Extraction Systems from Pb-15.7Li are analysed. The more promising one include PAV and GLC.

In chapter 3, two methods are proposed for dimensioning the packed tower. A specific of dimensioning with verification of the flooding conditions is reported.

In chapter 4, the main components and all the components that allow the operation of the TRIEX-II facility are described. Particular emphasis has been placed on permeation sensors, which play a key role in the analysis of extraction efficiency.

In chapter 5, a model of transport in Liquid phase for the transport of the hydrogen through a membrane has been developed. The model has been used to characterize the main factors that influence the response time of the sensor itself. A validation of the developed model with two experimental tests is presented here.

In chapter 6, a CFD-coupled transport model for the transport of the hydrogen is proposed. The models are developed for the saturator and the extractor installed on TRIEX-II. The procedure by which the mesh was designed and verified is also explained. In addition, the validation of the model CFD through the values of pressure drops of the extractor is shown. The transport model of saturator and extractor has been also validated with the experimental results.

1 Nuclear fusion reactors

Nowadays, to respond to numerous climate changes, new forms of alternative energy are being developed. These new forms of energy must first of all be renewable and must not emit greenhouse gases into the atmosphere.

One of the main technology that has been examined today to solve this problem is a fusion reactor because it would be able to guarantee a high energy production without dangerous emissions for the environment, in fact, fusion reactors do not emit any substance into the atmosphere that could increase greenhouse gases and in addition, fusion reactors produce little radiative material and with low decay times [1], [2].

There are different typologies of fusion reactors. They differ according to how the plasma is confined: magnetic, inertial, electrostatic and gravitational. From the engineering point of view, the solutions adopted are mainly two: magnetic and inertial. The magnetic confinement is based on the fact that the fuel in the form of plasma is contained by the magnetic compound. a very small amount of fuel is strongly compressed and heated thanks to lasers [3], [4].

There are several typologies for the reactors that exploit the magnetic confinement as tokamak (Figure 1), stellarator (Figure 2), spheromak, RPF, levitated dipole, Z-pinch, θ – pinch (Figure 3) [1] [4].

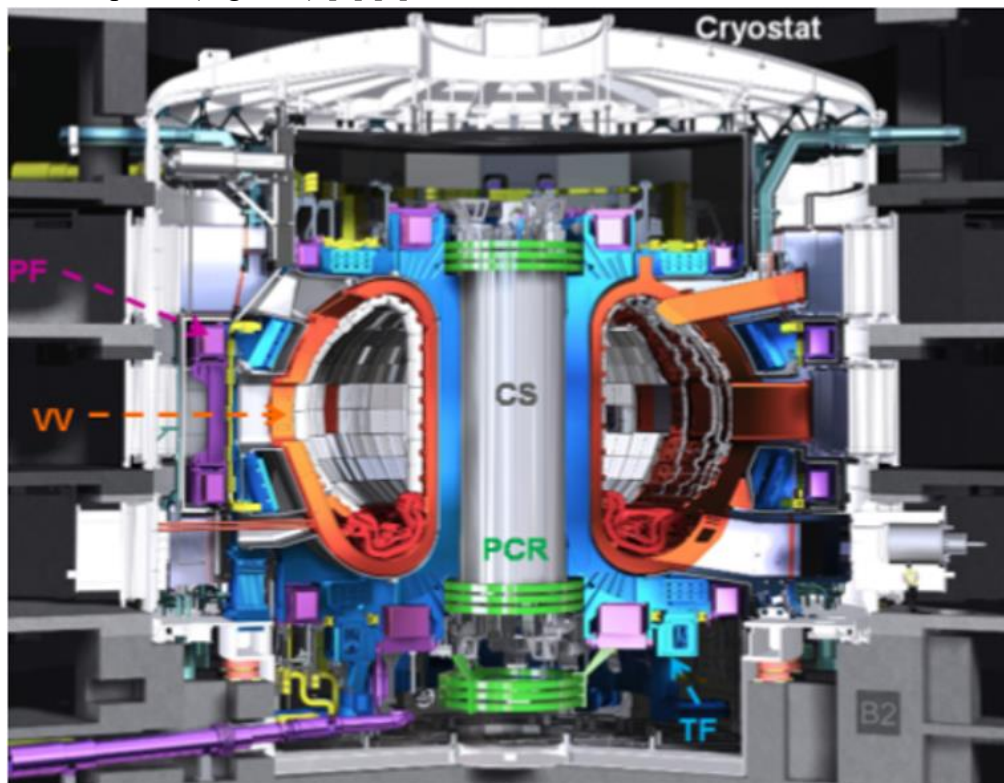


Figure 1 – Tokamak reactor [3].

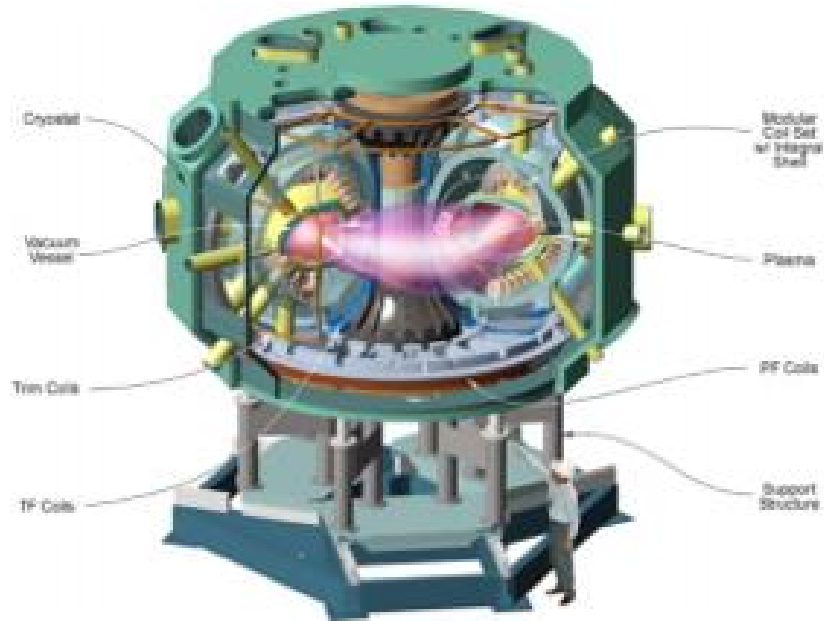


Figure 2 – Stellarator reactor [4].

The stellarator (Figure 2) has only one types on the magnets made of rigid copper rails and the system has a steady state configuration and no plasma current, the main characteristics are in Table 1 [5].

Parameter	Values	U.o.M.
Major radius	5.5	[m]
Minor radius	0.53	[m]
Pulse length	30	[min]
Plasma volume	30	[m ³]
Magnetic Field	3	[T]
Heating	14	[MW]
Plasma mas	5 – 30	[mg]

Table 1 – Mean parameters of the stellarator reactor [6].

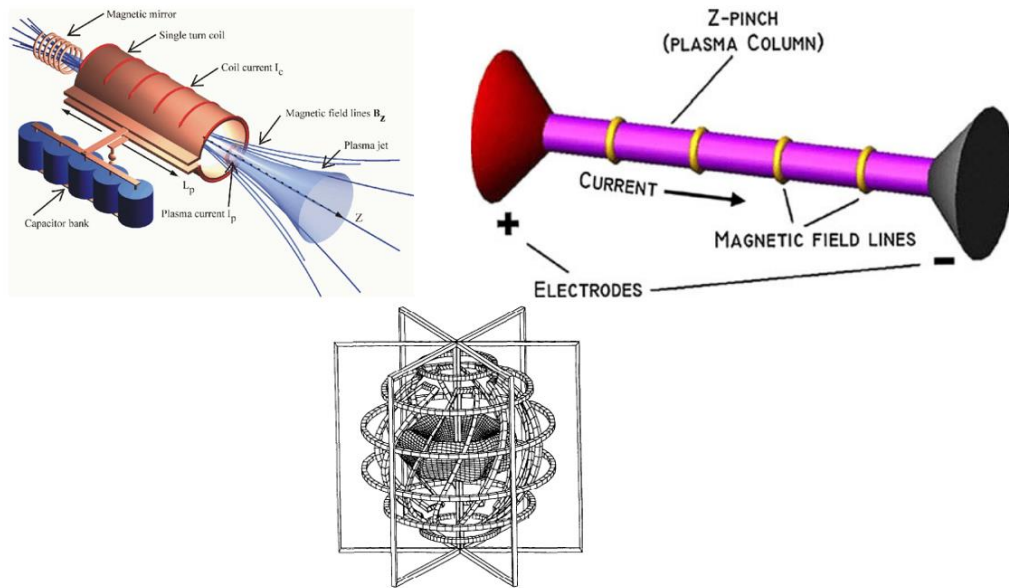


Figure 3 – θ pinch, z-pinch, spheromak magnetic confinement [7], [8], [9].

For the inertial confinement, there are two experiments under construction to demonstrate the feasibility: NIF (National Ignition Facility), and Laser Megajoule. The first one in the United States and the second one in France, there are others operating reactors and other reactors under construction. This system is based on the principle that very little balls made of deuterium and tritium are frozen and imploded by laser beams [10]. Tokamak and stellarator are the two typologies studied because they guarantee adequate plasma confinement for the realization of the fusion reaction.

The main differences between the two reactors are: on the typology of the magnets for the confinement and for type operation. The tokamak discharge is pulsed, and the current is inducted and it has four types of magnets: Toroidal, Poloidal, Correlation coils and central solenoid [1], [4].

For the nuclear fusion realization, two international projects ITER and DEMO are under development, these projects exploit the tokamak reactor: ITER project (International Thermonuclear Experimental Reactor) and DEMO project (Demonstration Fusion power reactor) [11]. The two projects are closely connected, in fact, the DEMO's design is influenced by future ITER experiments as reported in Figure 4.

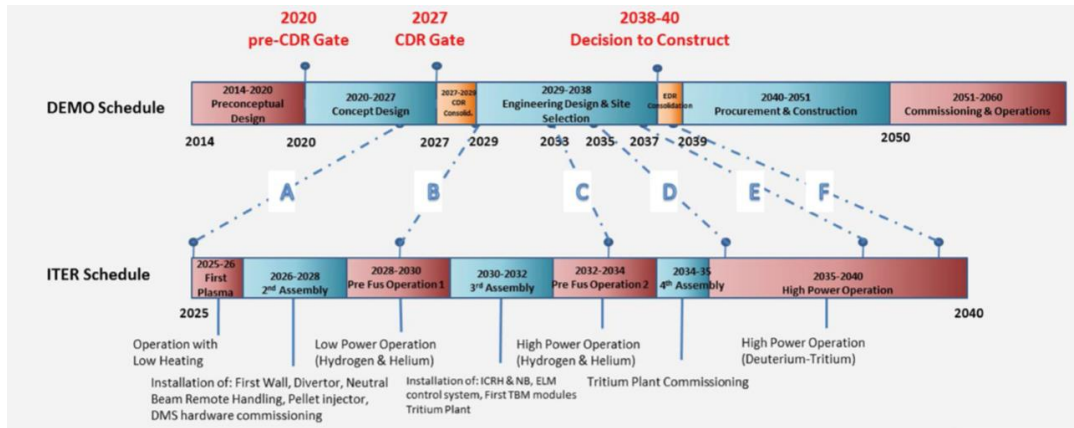


Figure 4 – Road maps of the ITER and DEMO projects [12].

The first plasma is expected to 2015. DEMO has just started the pre-conceptual design and before 2050 will begin the construction works [11].

1.1 ITER

ITER is the first step for using the fusion reaction to demonstrate the possibility to design, manufacturing and operate a fusion Thermonuclear reactor, demonstrating its feasibility. It was born thanks to the collaboration between the Soviet Union, United States, European Union, Japan, India, China and the Republic of Korea [11]. It wants to study all the aspects of nuclear fusion, both from the physical point of view (the physical principles that govern the fusion process) and from the engineering point of view. From the physical point of view, it wants produces a plasma dominated by particle heating α . It wants reaches a significant value of power amplification factor to guarantee a long pulse operation 400 [s]. From the engineering point of view, it wants to demonstrate the feasibility to integrate different technologies required by a fusion power plant, testing the different components that characterize a fusion reactor [13].

The main parts of ITER are:

- The magnet systems; the magnet system is composed of a central solenoid, toroidal field coils, poloidal field coils, and error coils.
- The vacuum vessel; The vacuum vessel serves to heat removal system while the reactor is in operation and for confinement barrier.
- The divertor; the divertor serves to reduce the impurity inside the plasma and serves to transfer the heat to the water.
- The cryostat; the cryostat serves to the thermal barrier.
- The heating system; the heating system serves to warm-up the plasma and it is composed by the NBI (neutral beam injection system), two cyclotrons one for the electron and one for the ions.
- The blanket. The blanket transfers the energy carried away to the plasma to a fluid.

The mean technical values of ITER are reported in Table 2.

Parameter	Values	U.o.M.
Total fusion power	500 – 700	[MW]
Plasma major radius	6.2	[m]
Plasma minor radius	2	[m]
Average pulsed duration	400	[s]
Plasma current	15	[MA]

Table 2 – Main parameters of ITER [14], [15], [11].

1.2 DEMO

DEMO wants to show at the world the possibility of using the energy produced with the fusion reaction. It is nothing more than the evolution of ITER. In fact, what is learned with ITER is used for the design and construction of DEMO.

Today there is no definitive project for the design and construction, but all aspects are still under study.

DEMO wants to propose to maintain the fusion reaction for much longer times (2 hours) than ITER, it wants to maximize the energy production yield, it wants to self-sustain the fusion reaction, it wants to produce in situ the fuel necessary for its operation. In fact, one of the main differences with ITER is the breeding blanket, which overcomes the internal production of tritium.

The main parameters of the DEMO are reported in Table 3.

Parameter	Values	U.o.M.
Total fusion power	2950	[MW]
Plasma major radius	5	[m]
Plasma minor radius	2.1	[m]
Average pulsed duration	2	[h]
Plasma current	16.7	[MA]

Table 3 – Main parameters of DEMO [16].

1.3 Comparison between ITER and DEMO

In Table 4, there are the main parameters that characterize the major differences between ITER and DEMO. Despite DEMO born thanks to ITER, the two projects differ both from the point of the structure and from the point functional.

ITER	DEMO
Fusion power = 3300 [MW]	Fusion power = 500 [MW]
Experimental facility, built to test all the components of a fusion reactor.	Test of the first commercial fusion reactor.
Pulsed system, with duration of each single pulse = 400 [s].	Pulsed system, with duration of each single pulse ~ 2 [h] or steady state condition.
Elevate number of the diagnostics.	Diagnostic needed only for the operating conditions.
No limit for the design, due to the high uncertainties.	Maximize design, keeping in mind the experience gained with ITER.
The cooling system is optimized for the minimum stress value.	Cooling system is optimized for the electricity generation efficiency.
No breeding blanket, tritium required is	The breeding blanket need to maintain the fusion reaction., tritium required
For the vessel, the 316 stainless steel is used	material with a low value of activation and material for the breeding blanket
Do not produce electric energy	Produce electric energy

Table 4 – Main difference between ITER and DEMO [17].

2 Tritium extraction system from lead-lithium

One of the main characteristics that differentiate the two facility ITER and DEMO is the breeding blanket. The breeding blanket problem is fundamental for the fusion reactor's operation. The blanket has three fundamental functions: power extraction (kinetic energy conversion of neutrons into heat), shielding and tritium production. These three different functions involve the blanket's design complication e.g. due to the different materials integration and compatibility [18].

Many aspects must be considered when designing the blanket:

- Nature of the breeder material; for the Breeder material it is possible to have different liquid-liquid, solid-liquid configurations.
- Structured materials (for the activation and compatibility with other material);
- Tritium removal systems; the tritium extraction system serves to extract the tritium from the Pb-Li.
- Fuel cycle (Figure 5); different sub-systems are connected to the fuel cycle.

To optimize the design must be featured in order to achieve low maintenance time to reduce the downtime due to failure, sufficiently long lifetime and high safety level [1].

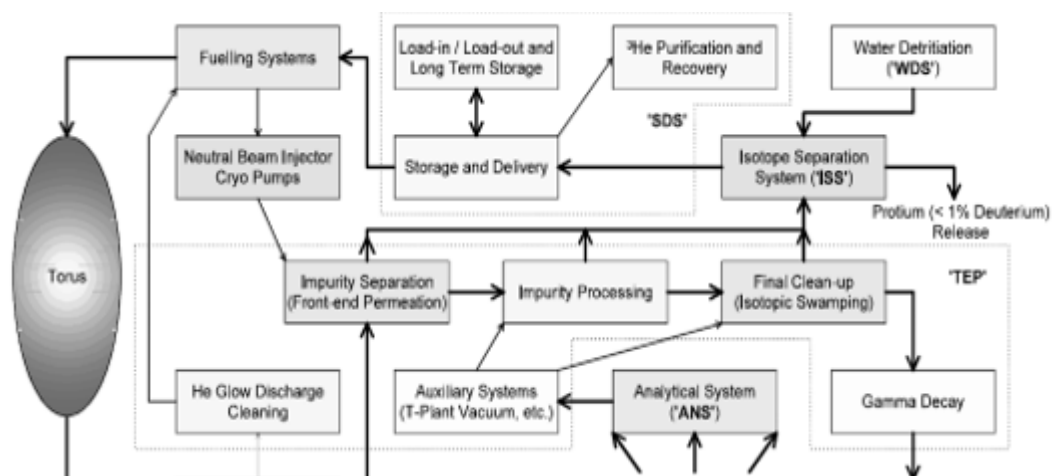


Figure 5 – Fuel cycle in a fusion reactor [19].

Nuclear fusion involves two light atoms such as Tritium and deuterium. Deuterium is very easy to procure, as it is naturally found in very small

percentages of the whole sea, while Tritium even if in minimal quantities. It is produced naturally in the atmosphere by cosmic rays. [20] so it must somehow procure it. The tritium can produce two ways: or from the CANDU reactors or to produce tritium inside the facility, the reactor must be used, the breeding blanket technology.

One of the most promising technology for the breeding is constituted by metal liquid, in particular, a metal alloy composed by lithium and lead. This metal alloy has a eutectic composition of 15.7 % of lithium and 84.3 % of lead (Figure 6). It combined the lithium property to produce tritium with the properties of lead as coolant and as neutron source.

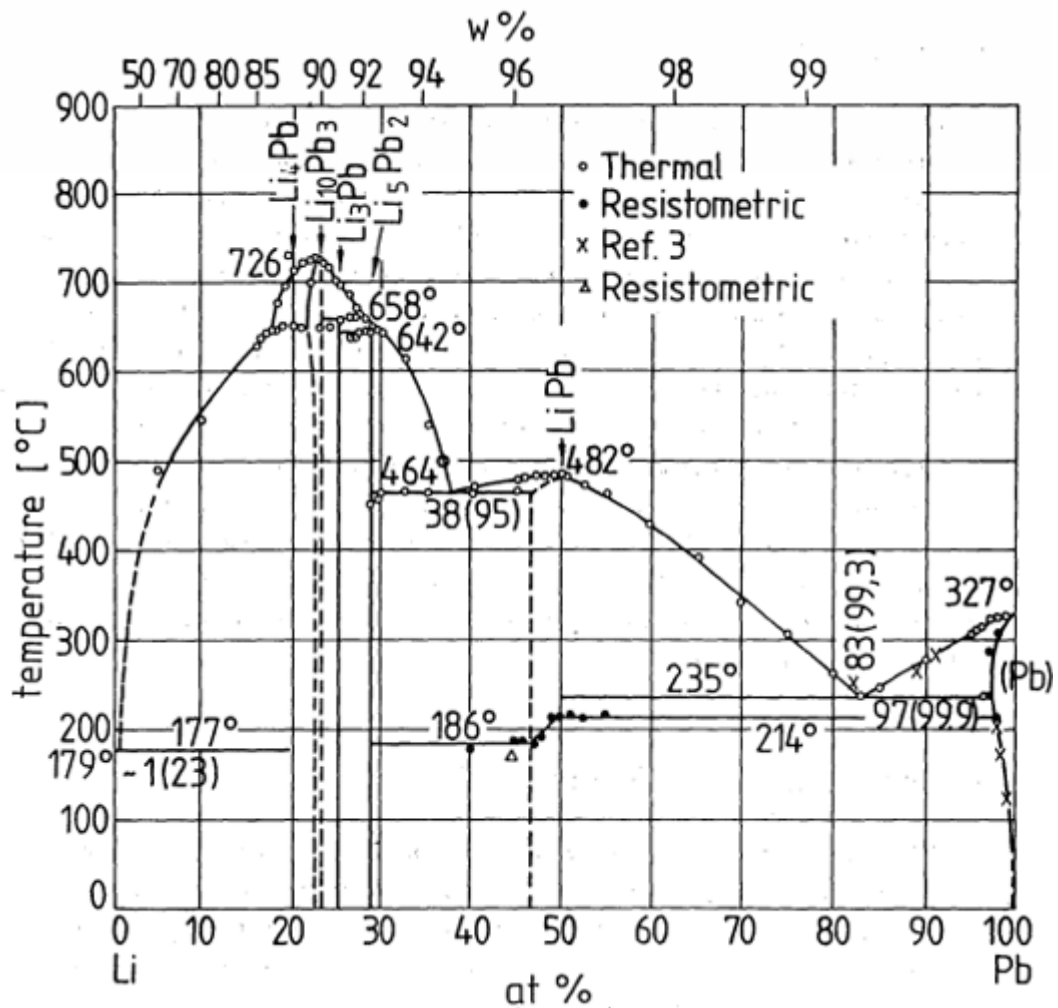


Figure 6– Phase diagram of Pb-Li [21].

There are three different possible configurations of BB which use lithium lead: WCLL, DCLL, and HCLL. All these configurations use liquid metal as breeder and multiplier [22].

The WCLL Water Cooled Lithium Lead (Figure 7) is developed by EURO fusion Breeding Blanket Project. This configuration has 18 Toroidal field coils, each coil corresponds to a sector. Each sector is composed of two inboard and three outboards. with an upper port and a lower port. The upper and lower port serves

as the outlet for the water and the PbLi. The WCLL configuration is composed by the integrated First Wall, the Breeding Zone, the Back-Supporting Structure. The segments are divided into seven modules with different sizes. each module is a steel box made of Eurofer, reinforced with an internal grid. The PbLi loop guarantees the circulation of the breeder in the tritium extraction system and the PbLi completely fills the breeder unit [23].

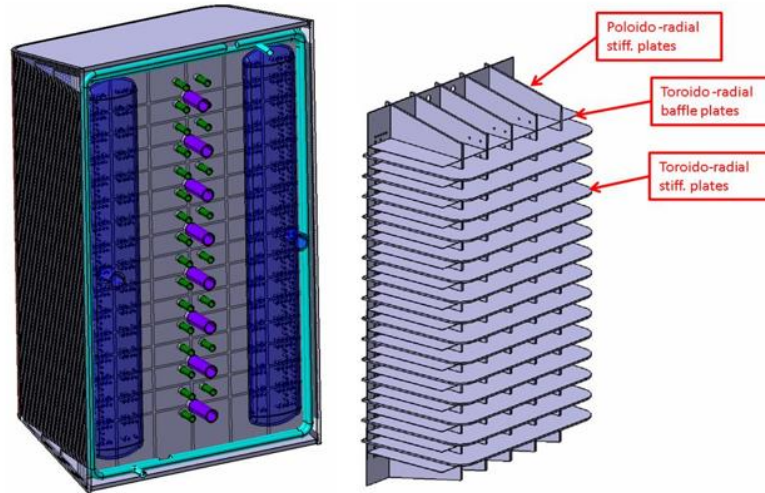


Figure 7 – Modul of WCLL breeding blanket configuration [23].

The DCLL Dual-Coolant Lead Lithium (Figure 8) is the most studied in European blanket development. The DCLL is composed on a multi-module segment configuration. Each segment has eight different modules attached to a common. The module has a circulation of PbLi in the poloidal direction in order to extract all the total reaction power. The breeding zone consists of four parallel PbLi circuits separated by grids to avoid pressure drops due to MHD effects [24].

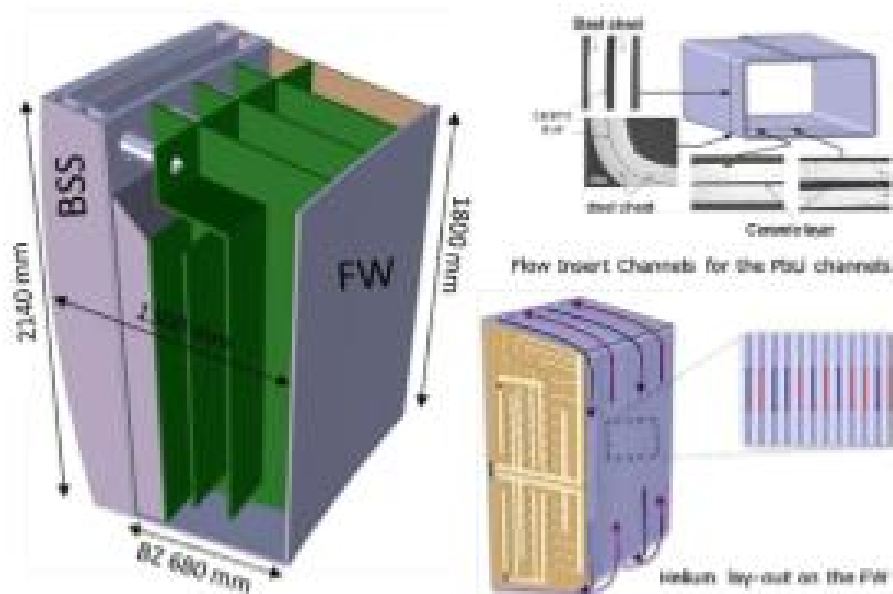


Figure 8 – Modul of DCLL breeding blanket configuration [24].

The HCLL Helium-cooled Lithium-Lead (Figure 9). In this configuration, the Pb-

Li is used as coolant, breeder, neutron multiplier half of transport for the tritium. The HCLL is constituted by a steel box with a U-shaped plate, closed thanks to a lateral plate and with a parallel plate on the backside. The structural material of the first wall, cooling plat, and stiffening plates are made of EUROFER [24].

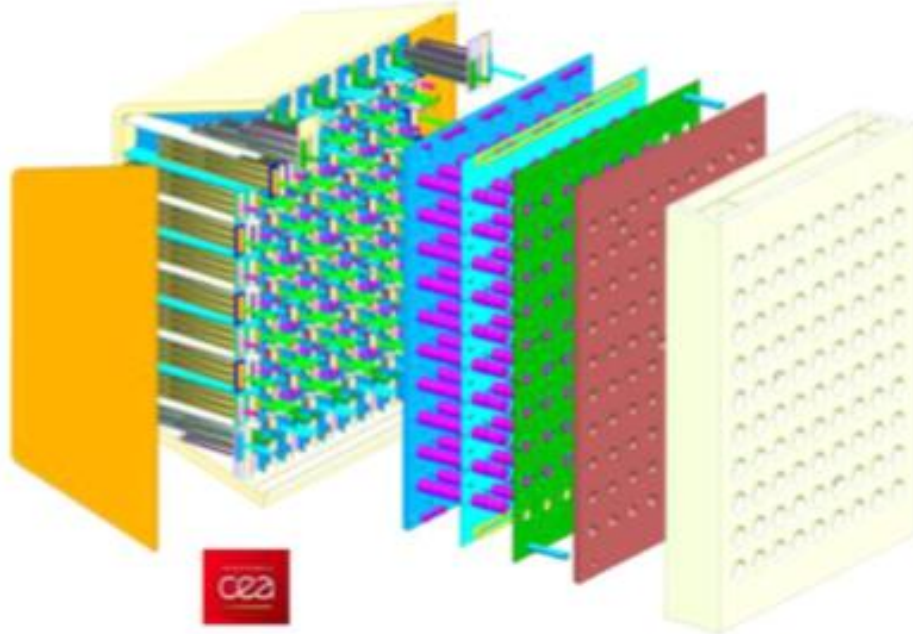


Figure 9 – Modul of HCLL breeding blanket configuration [24].

These units produce tritium, but in order to use tritium, it must be subjected to the process of purification and extraction from liquid metal. To extract tritium, the metal alloy requires an extraction system called (TES).

The TES is the entire extraction cycle of tritium that allows having tritium ready for use. The tritium extraction system is the system used to separate the tritium from the PbLi through the tritium extraction units (TEU).

TEU is the unit that allows extracting tritium from PbLi but is not yet ready for use because it is still mixed with stripping gas [25]. There are different typologies of tritium extraction units: PAV (Permeation against Vacuum), VST (vacuum sieve tray), regenerable getter and GLC (Gas-Liquid Contactors), these technologies exploit the permeation process.

2.1 Tritium extraction technologies for lead-lithium

2.1.1 PAV

This technology exploits the permeation process through a metal membrane (Figure 10). It divided the liquid metal (where a certain concentration of hydrogen is solubilized inside it) from the vacuum.

As the process of permeation of a gaseous substance through a membrane exploits the concentration gradient of the species between the two domains, this technology is able to maximize and speed up the phenomenon by always maintaining a certain concentration gradient by continuously pulling the vacuum (decreasing the concentration the permeates). The process takes advantage the gradient of tritium partial pressure on the two sides of the membrane, (Figure 10), in fact, thanks to the vacuum the gradient is maximized and the extraction process is accelerated considerably [26].

The material of with the membrane is made has a great influence on the permeation process, in fact for the choice of the material several parameters must be considered as high-temperature resistance, high permeability to tritium, high corrosion resistance to Pb-15.7Li, high mechanical resistance and malleability [22].

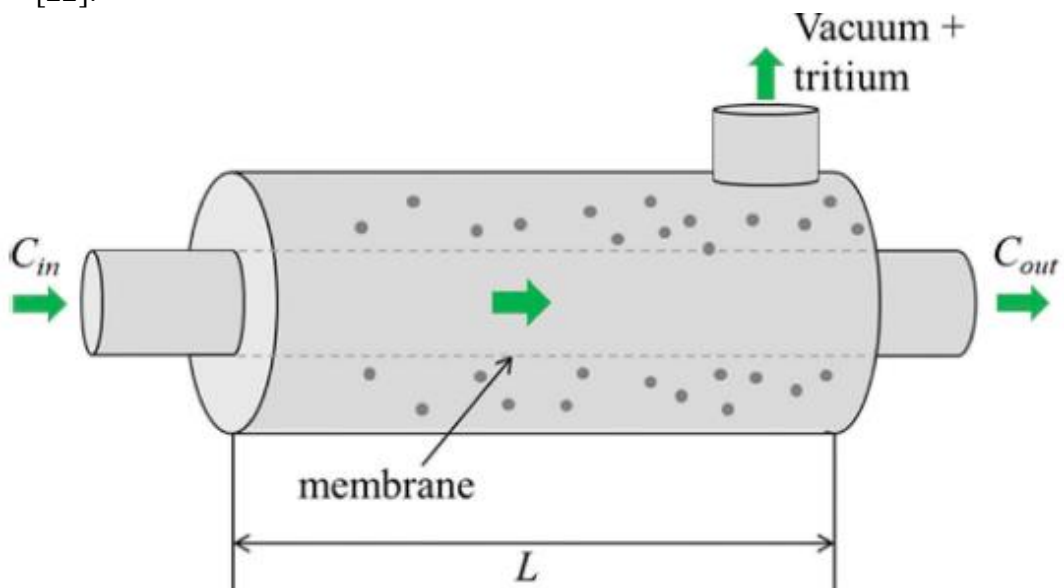


Figure 10 – Scheme of the PAV system [26].

2.1.2 GLC (Gas-Liquid Contactor)

The Gas-liquid contactors (Figure 11) are designed to characterize the mass and heat transfer between two different phases, liquid and gas phase. This technology is used for multiple applications, in many industrial applications chemical, petrol chemical, in many industrial sectors e.g. hydrodesulfurization, Hydrodesulfurization [27].

There are five different possible types of gas-liquid contactor: wetted-wall, bubble column, spray tower, plate column and packed column,

In the thesis, I focus only on the packed column and the bubble column.

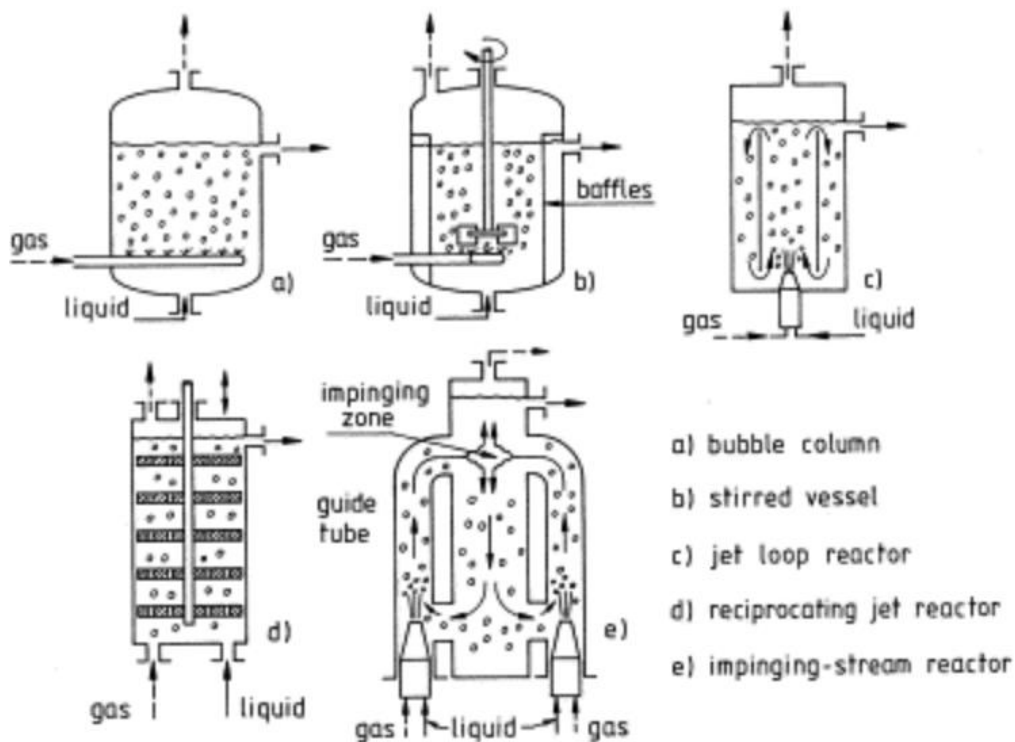


Figure 11 – Different typologies of Gas Liquid Contactors [28].

Bubbles columns

A bubbles column (Figure 12) consists of a cylindrical vessel with a gas distributor located at the bottom. The gas is distributed in the form of bubbles. Thanks to the bubbles the contact surface increase and consequently the heat transfer and the mass transfer improve. One other advantage of this technology is the low maintenance and low operating cost [29], but have a very low value of extraction efficiency [28].

This technology is used in many industries for example in chemical, petrochemical, biochemical and metallurgical [27].

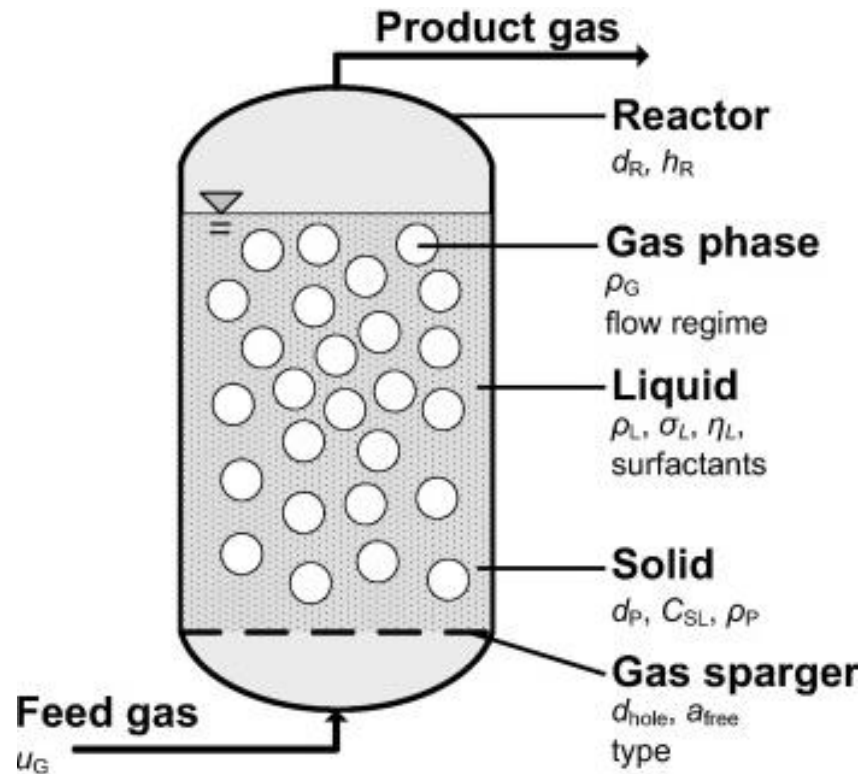


Figure 12 – Scheme of bubble column [30].

Packed column or packed tower

The Packed column or packed tower (Figure 13) consists of a cylindrical body with gas and liquid distributor. Inside there is the structured packing or random packing. The structured packing is composed by numerous metallic material sheets, perforated (since in the field of fusion uses the liquid metal which is a high-density fluid, perforation improves both the passage of liquid and gas). This design allows to increase the liquid-gas contact surface, slows the fluid speed, also increasing the contact time, further improving the mass exchange.

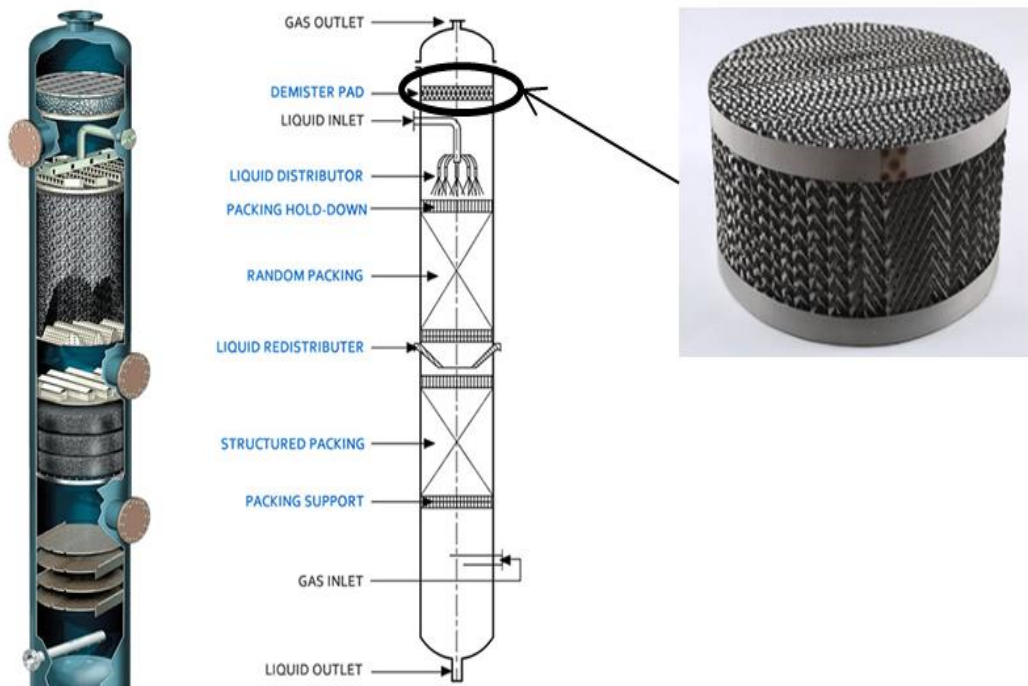


Figure 13 – Scheme of packed column with an example of a structured packing [31].

The working principle of the GLC is that the liquid enters from the top, while the gas enters from the bottom. The gas being lighter tends to go up the column while the liquid being heavier tends to go down Figure 14.

The main parameters that taking part in the physical process are (Figure 14): G_{M1} [kmol/s] is the gas mass flow rate at the inlet of the packed tower, G_{M2} [kmol/s] is the gas mass flow rate at the outlet, L_{M1} [kmol/s], y_1 [-] and y_2 [-] are the molar fractions of the solute in the gas at the inlet, x_1 [-] and x_2 [-] are the molar fractions of the solute in the liquid at the inlet, and x and y are the molar fractions of the solute in the liquid and in the gas at a certain height.

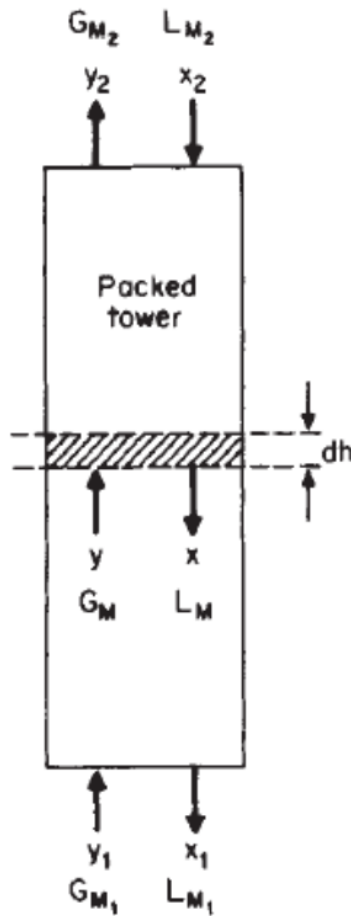


Figure 14 –Operating scheme of the pocked tower [25].

To avoid the non-uniform distribution of the two fluids, the gas, and liquid flow through the packed material. In fact, the fluid phase tends to flow to the wall, while the gas phase tends to flow in the center of the tower [31].

The packed material improves the surface contact between the two fluids. The greater contact surface and the longer residence time of the fluid increase the mass exchange considerably. The packed towers are applied in filtering, vacuum and purifying [31]. The packed tower is composed by tower body, tower packing (composed by structured packing, random packing, and demister pads) and the tower internals (liquid distributor, packing supporting grid, packing hold-down grid, liquid redistribute and gas distributor [31].

The main characteristics are large production capacity, high separating efficiency (30 %) that can be calculated with a simple mass balance of the concentration of the species that is extracted [27].

2.2 Comparison between PAV and GLC

Gas-liquid contactors (Figure 11) are used for the mass and heat transfer between two different phases, liquid and gas phase. This technology is used for multiple applications, in many industrial applications chemical, petrol chemical, in many industrial sectors e.g. hydrodesulfurization.

There are four technologies studied for the tritium extraction systems, all these technologies exploit the same physical principles but in a slightly way. The PAV, Vacuum Sieve Tray exploit the gradient of concentration of tritium between the fluid and the vacuum, while the GLC exploit the gradient of concentration of tritium between the fluid and the gas, the regenerable getters exploit the gradient of concentration of tritium between the fluid and the solid material with is used to the stripping of the tritium.

For the extraction of tritium technology, the GLC is the most promising technology, because it has a higher level of extraction efficiency than the other technologies, it is a technology already widely used in the industrial field and consequently having already been studied, so the construction is more simplified as there are numerous companies in the sector.

The other three technologies still present high difficulties from the technological point of view and above all fail to guarantee high levels of extraction efficiency.

In Table 4 there are comparisons between the different typologies for the tritium extraction.

Technology	Characteristic	Advantage	Drawback	Efficiency
PAV	Permeation vacuum-membrane	Continuous vacuum	Developing technology	80-90 [%]
GLC	Permeation gas-liquid phase	High surface contact Low pressure drop	Large system High energy consumption	20-30 [%]

Table 5 – Main difference between PAV and GLC [22], [32].

3 Design of a GLC-packed tower

To design a GLC-packed tower, it is necessary to evaluate the height and the diameter of it.

First of all, the flooding conditions are calculated to estimate the range of the diameter as wide as possible, after which the height is calculated based on the diameter chosen.

3.1 Diameter

The diameter is hypothesized by the one values of flow rate and speed of the fluid using the following formula:

$$d_t = \sqrt{\frac{4 \cdot L}{\rho_j v \cdot \pi}} \quad (1)$$

Where L is the flow rate of the liquid [kg/s], ρ_j is the density of the liquid and v is the velocity of the fluid.

After which the flooding conditions must be respected for which, and they are evaluated, with the following equation. The flooding conditions determines the minimum possible diameter.

$$F_{LG} = \frac{L}{G} \cdot \frac{\sqrt{\rho_i}}{\sqrt{\rho_j}} \quad (2)$$

the parameters that are involved for the calculation of flooding conditions are: G is the flow rate of the gas [kg/s], ρ_i is the density of the gas $\left[\frac{\text{kg}}{\text{m}^3}\right]$.

F_{LG} is needed to evaluate the flooding specific mass flow rate of the gas with the following formula: [9]

$$G'_{\text{flood}} = \sqrt{\frac{g \rho_j \rho_i \varepsilon \left(\frac{\mu_i}{\mu_j}\right)^{-0.2}}{a} \exp(-4 F_{LG}^{0.25})} \quad (3)$$

$$v_{\text{flood}} = \frac{G'_{\text{flood}}}{\rho_{Ar}} \quad (4)$$

Where μ_j is the viscosity of the fluid, and μ_i viscosity of the gas.

The flooding conditions determines the minimum possible diameter, and they are used to verify whether the value of velocity and flow assumed at the beginning is acceptable. In general, the design is for 60 % to 80 % of the flooding condition.

3.2 Height

The second step for the design of the packed tower is how to calculate the height. To calculate it, it is possible to use the following formula:

$$h_t = \int_{y_2}^{y_1} \left(\frac{G_M dy}{k_G a (1-y)(y-y_i)} \right) \quad (5)$$

where k_G is local mass transfer coefficient of the gas, y is the molar fraction of the gas in the operating curve, y_i is the molar fraction in the equilibrium curve.

3.3 Alternative method

Here, the HTU · NTU method will be described. It is featured by the necessity to know the equilibrium concentration point by point [25]. The height can be calculated as:

$$h_t = \text{HTU} \cdot \text{NTU} \quad (6)$$

Where HTU [m] is the height of a single Transfer unit and NTU [–] is the Number of Transfer Units and can be evaluated both from gas and side or liquid side.

HTU is calculated through the mass transfer coefficient and the packing surface:

$$\text{HTU} = \frac{L}{k_L C_t a A_c} \quad (7)$$

where C_t [kmol/m³] is the molar concentration of the fluid [33].

NTU is more difficult to evaluate because the following integral must be solved:

$$\text{NTU} = \int_{x_{in}}^{x_{out}} \frac{dx}{x_i - x} \quad (8)$$

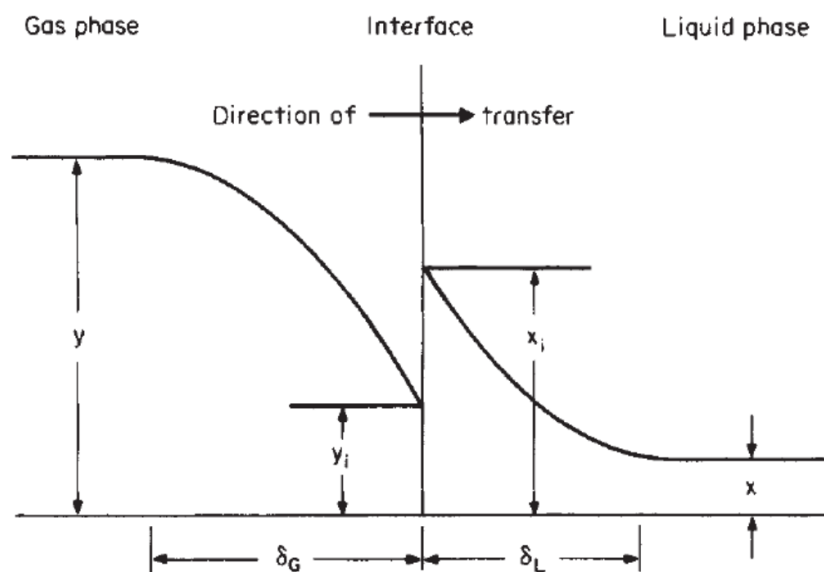


Figure 15 – Concentration trend at the liquid-gas interface [25].

The concentration at the interface between the liquid and the gas is reported in Figure 15.

In the case of dilute systems, heat effects neglect and straight operating condition the equilibrium line can be described with the following simplified equation for NTU can be written:

$$NTU = \frac{1}{1 - \frac{L_M}{mG_M}} \ln \left[\left(1 - \frac{L_M}{mG_M} \right) \left(\frac{x_2 - \frac{y_1}{m}}{x_1 - \frac{y_1}{m}} \right) + \frac{L_M}{mG_M} \right] \quad (9)$$

where m is the slope of the equilibrium line.

From the point of view of the gas, the equation for NTU is:

$$NTU = \frac{1}{1 - m \frac{G_M}{L_M}} \ln \left[\left(1 - \frac{mG_M}{L_M} \right) \left(\frac{y_1 - mx_2}{y_2 - mx_2} \right) + \frac{mG_M}{L_M} \right] \quad (10)$$

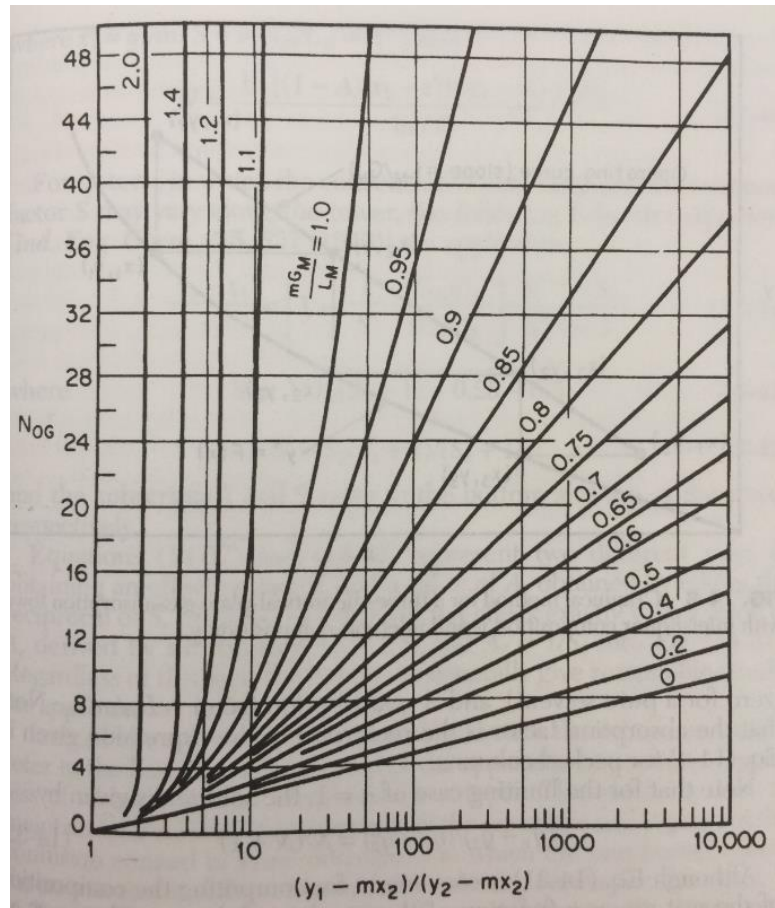


Figure 16 – Graphically trend of mG_M/L_M [25].

The ratio $\frac{mG_M}{L_M}$ can be calculated graphically by means of Figure 16.

3.4 Sizing

A sizing calculation was made of a packed filling installed the TRIEX plant, which will be described in chapter 5. This plant used as fluid the Pb-15.7Li, while as stripping gas it used the argon.

For the total height was considered a safety factor equal to 2. This parameter was chosen to be able to be sure to meet the required efficiency value.

The main input parameters are shown in Table 6.

Data	Values	U.o.M.
Efficiency, η	0.30	[-]
Inlet molar fraction of H ₂ in argon, y_1	0	[mol _{H₂} / mol _{Ar}]
Inlet molar fraction of H in Pb-15.7Li, x_2	$3.86 \cdot 10^{-5}$	[mol _{H₂} / mol _{PbLi}]
Flow rate of Pb-15.7Li, L	0.2	[kg/s]
Flow rate of argon, Q _L	100	[Nl/h]
Temperature, T	723	[K]
Pressure, p	7	[bar]

Table 6– Main input parameter.

3.4.1 Main calculations

Through the. eq. 4 has been calculated the flooding velocity which turns out to be 0.0066 [m/s]. With the speed of flooding has been calculated, the diameter of the packed filling in flooding conditions which turns out to be 5 [cm].

The data shown in the Table 7 are the parameters needed for the flooding conditions.

Data	Values	U.o.M.
Section of the column, A _c	0.0129	[m ²]
Specific molar flow rate of Pb-15.7Li, L _M	0.0884	[kmol/m ² /s]
Specific molar flow rate of argon, G _M	$1.47 \cdot 10^{-4}$	[kmol/m ² /s]
Velocity of Pb-15.7Li, v _{Pb-15.7Li}	0.0016	[m/s]
Velocity of argon, v _{Ar}	$8.99 \cdot 10^{-4}$	[m/s]
Mass-transfer coefficient of Pb-15.7Li, K _{Pb-15.7Li}	$1.51 \cdot 10^{-5}$	[m/s]

Table 7– Initial calculations

To calculate the height of the Column, the HTU NTU method was used, which has been described in 3.3., The total height result equal to h=66.24 [cm].

4 TRIEX-II facility

4.1 TRIEX and TRIEX-II facilities

In the research center of ENEA Brasimone, in 2006 TRIEX (Tritium Extraction facility) facility has been built to test and qualify the Gas-Liquid Contactor (GLC) as a candidate technology for tritium extraction from the liquid metal alloy Pb-15.7Li of Helium-Cooled Lithium-Lead Test Blanket Module (HCLL-TBM) of ITER. In Figure 17 the Piping and Instrumentation Diagram (P&ID) is shown.

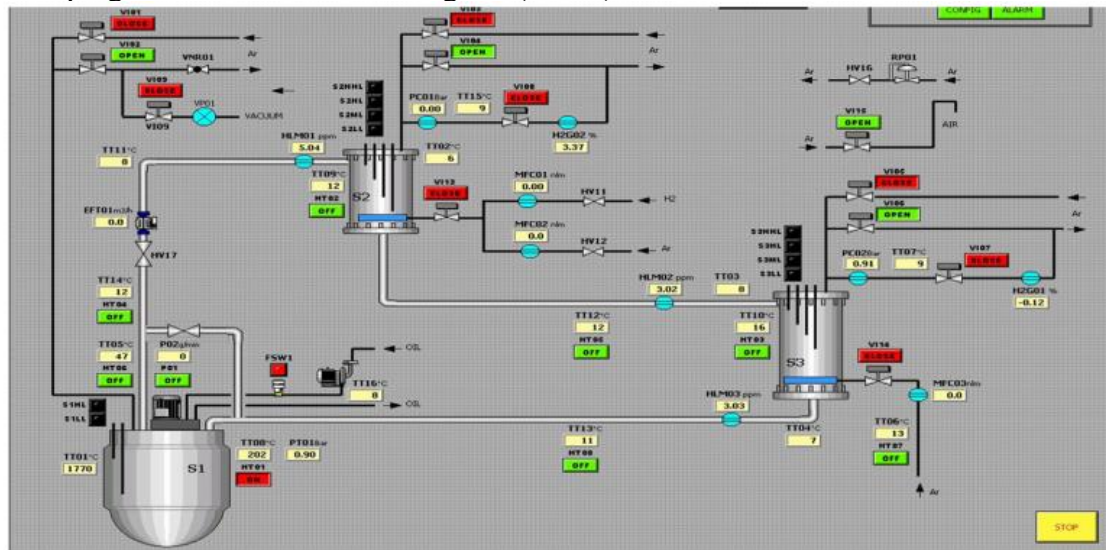


Figure 17 – The layout of the old TRIEX facility.

TRIEX was characterized by a ring design; this kind of design was chosen because in that way only the pressure drops had to be overcome. The main components were:

- The recirculation tank, S1;
- The liquid metal pump;
- The instrumentations;
- The hydrogen saturator, S2, to saturate the hydrogen inside the metal alloy;
- The hydrogen extractor, S3, to extract the hydrogen from the metal alloy;
- The sensors to measure the concentration of hydrogen inside the metal alloy;

In TRIEX, there were two separated loops: one for the Pb-15.7Li and one for the gas. The Pb-15.7Li loop was closed, whilst the gas loop was open. The saturator allowed the alloy to reach the desired hydrogen concentration, which simulated the HCLL-TBM outlet composition of Pb-15.7Li. The extractor allowed the extraction of the hydrogen concentration previously saturated to simulate the tritium extraction from the HCLL. The saturator and the extractor were equipped with a structured packing Baretta B1, characterized by a specific interface area between liquid and gas phase equal to $350 \text{ [m}^2/\text{m}^3]$ [34]. The operational conditions were characterized by helium as stripping gas and hydrogen to simulate tritium [34].

During the experimental campaign, three major drawbacks were presented. Firstly, it was not possible to check the closure of the hydrogen mass balance due to the low accuracy

of the instrumentation. Moreover, only in few cases, the equilibrium between the gas and liquid phases was reached before starting the hydrogen extraction: one of the causes was the very long response time of the permeation sensors, but also the impossibility for the saturator to replace the hydrogen extracted. Last but not least, a correlation between the efficiency and the ratio L/G (ratio of the liquid mass flow rate, L , and the gas mass flow rate, G) was not found, due to the low number of experiments performed. Due to these problems, an upgrade was designed, named TRIEX-II. It was designed with a dual function: primarily, to address the problems highlighted with TRIEX and secondly, to increase the extraction efficiency and at the same time to work with lower concentrations which should be representative of DEMO fusion reactor.

TRIEX-II maintains the same concept design of TRIEX but with considerable improvements for all the components, which will be analysed in detail in Section 5.2. **Errore. L'origine riferimento non è stata trovata.** The new layout of the facility is shown in Figure 18.

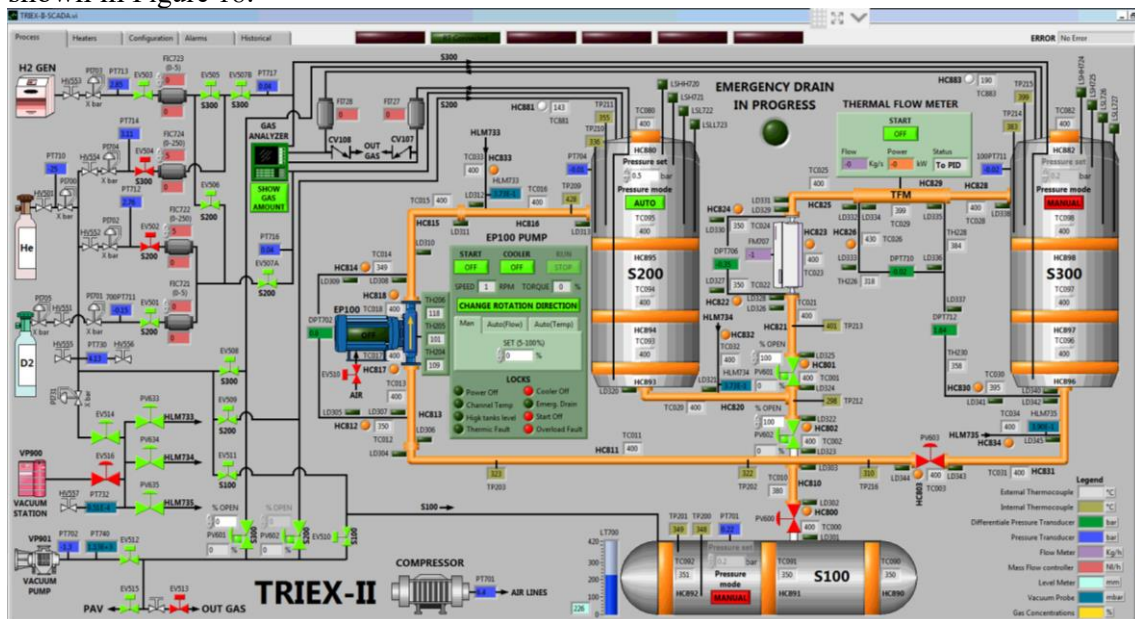


Figure 18 – The layout of the upgraded TRIEX-II facility.

4.2 Main components of TRIEX-II

In this section, an overview of all the components that characterise the new facility TRIEX-II for tritium extraction from Pb-15.7Li is made. The main components of characterizing TRIEX-II are:

- Permanent magnet pump (100-EP-100);
- Thermal mass flow meter (100-FM-708);
- Storage tank (100-S100);
- Saturator (100-S200);
- Extractor (100-S300);
- Permeation sensors (100-HLM-733, 100-HLM-734, 100-HLM735);
- Mass spectrometer (700-HGA-001);

TRIEX-II is more complex than TRIEX: for example, one of the main differences between TRIEX and TRIEX-II is the gas analysis system. The complexity regards not

only the gas analysis system but also the main components (the saturator and the extractor have been complexity redesigned) and the instrumentation for the operation and the control of the facility itself.

4.2.1 Permanent magnet pump

In TRIEX there was a mechanical pump, that presented several issues such as the high-pressure drops due to the friction and problems of corrosion because the impeller immersed in the Pb-15.7Li had high levels of corrosion. To avoid these problems in TRIEX-II a new Permanent Magnet Pump (100-EP-100) (Figure 19) has been installed. The Permanent Magnet Pump (PMP) is based on the physical principle that when a current conductor (in this case, the Pb-15.7Li) is placed in a magnetic field, a Lorentz' force is exerted on it; this allows the liquid alloy to be pumped. Moreover, the electric current creates an ohmic resistance, keeping the internal channel hot. This pump was made by SAAS Gmbh and it has the characteristics indicated in Table 8.



Figure 19 – Permanent Magnet Pump.

<i>Characteristic</i>	<i>Values</i>
<i>Model</i>	<i>PMP 300 Pb-15.7Li</i>
<i>Temperature range</i>	<i>250-350 [°C]</i>
<i>Type</i>	<i>Disk type (PMP)</i>
<i>Maximum head</i>	<i>4 [bar]</i>
<i>Minimum Head</i>	<i>0.3 [bar]</i>
<i>Maximum mass flow rate</i>	<i>5 [kg/s]</i>
<i>Flange connection</i>	<i>ASA 300 ANSI B16.5 1" for inlet/ outlet</i>
<i>Mass flow control</i>	<i>Inverter</i>
<i>Electrical motor</i>	<i>5.5 [kW]</i>
<i>Security equipment</i>	<i>Thermocouples</i>
<i>Design pressure</i>	<i>10 [bar]</i>
<i>Electrical heating cuffs</i>	<i>400 [W]</i>

Table 8 – Main characteristics of the permanent magnetic pump.

The typical p – Q characteristic of the pump as given by the provider is reported in Figure 20.

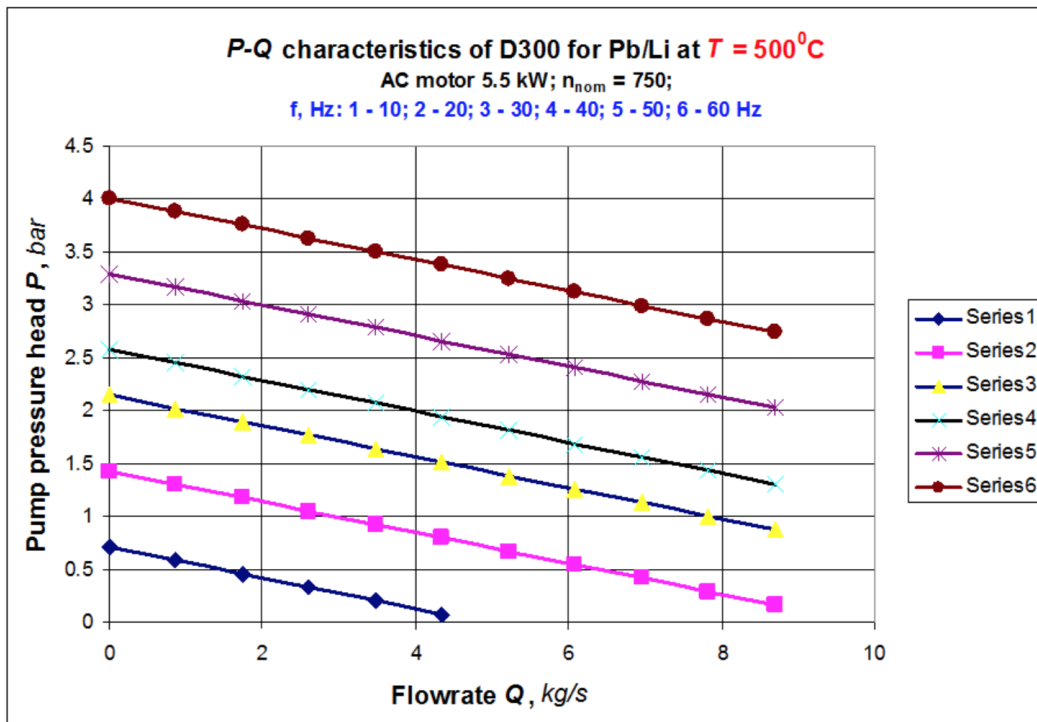


Figure 20 – Characteristic curve of the pump.

4.2.2 Thermal mass flow meter

To measure the lead-lithium mass flow, a thermal flow meter (Figure 21) is used. It can measure the flow rate of Pb-15.7Li by measuring the gradient of the temperature. The thermal mass flow meter is provided at the entrance of a propeller that serves to break the vortices of the fluid to have an unfair distribution of the fluid.

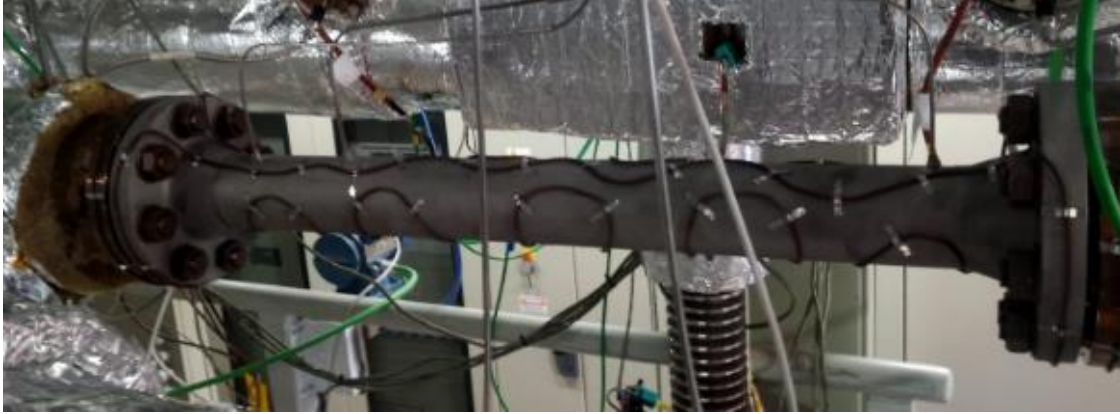


Figure 21 – Thermal mass flow meter [35].

The main characteristics are reported in Table 9.

Characteristic	Value	U.o.M.
Measuring rate	0.2-5	[kg/s]
Nominal mass flow	3.6	[kg/s]
Declared flow accuracy	0.1	[kg/s]
Heating element power	6	[kW]
Maximum operative T	530	[°C]
Maximum operative P	10	[bar]

Table 9 – Thermal flow meter main characteristics [34].

4.2.3 The storage tank

The storage tank (100-S100), shown in Figure 22, is a vessel dedicated to contain the Pb-15.7Li needed to fill the system (including the extractor, the saturator, and all the pipes). It has penetrations needed to measure the Pb-15.7Li level. To charge and discharge the Pb-15.7Li in the facility, the Pb-15.7Li pipe line is placed in the bottom part of the tank, the liquid metal is loaded by pressurization or depressurization of the storage tank. The vessel is wrapped by heating cables in order to warm up to operational temperature. It is also equipped with thermocouples (type K) to detect the inner temperature.



Figure 22 – Storage tank.

The main design parameters of the storage tank are reported in Table 10.

Characteristic	Value	U.o.M.
Operative temperature	500	[°C]
Design temperature	530	[°C]
Design pressure	10	[bar]
Operative pressure	5	[bar]
Material	2 1/4 – Cr-Mo	[-]
Total volume	400	[dm ³]
Hydraulic test pressure	32	[barg]
Empty weight	400	[kg]

Table 10 – Main parameters of the storage tank.

The material is ferritic-martensitic steel and it was chosen to reduce the corrosion by the liquid metal.

4.2.4 The Saturator

The saturator (100-S100) has the function to solubilize the hydrogen contained in a mixture with helium in the lead-lithium eutectic alloy; it is constituted by a vertical cylinder with a structured filling inside. The saturation column (Figure 23) has a hybrid nature, in the sense that in the lower part a packed column solution with structured filling is adopted, whereas the upper part is a bubble column, for which the operating principle has been shown in Chapter 3. With respect to the extractor GLC mock-up, the saturator is 765 [mm] higher, in order to accommodate these two technologies.



Figure 23 – Saturator tank.

The Sulzer Mellapak, shown in Figure 24, is chosen as packing material; to allow the Pb-15.7, the 425 Y model with a surface ratio of $450 \text{ [m}^2/\text{m}^3]$ has been selected. A higher surface-to-volume ratio has been not suggested by the provider because of the high surface tension of the Pb-15.7 with respect to the water. Two Mellapak packings have been installed in the saturator; the positioning has been performed by means of distancer bars.

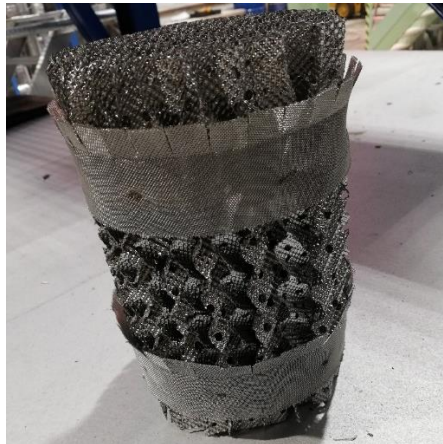


Figure 24 – The Mellapak 452/ structured packing.

The gas injection system (Figure 25) is located at the bottom of the saturator. The heating cables are placed in contact with the vessel, to warm up the liquid metal to the operational temperature. The saturator is equipped with thermocouples to detect the temperature at different positions. At the top there are four level meters to measure the liquid metal level and, in case of high-level signal, the emergency draining is activated. The saturator operating principle is explained in detail in Chapter 3. The operative conditions are summarized in Table 11.

Parameter	Values	U.o.M.
Design pressure	10	[barg]
Operative pressure	5	[barg]
Design temperature	530	[°C]
Operative temperature	500	[°C]
Nominal Pb-15.7Li flow rate	1.2	[kg/s]
Saturator flow rate	10 – 250	[Nl/h]
Pb-15.7Li mass flow rate	0.2 – 4.5	[kg/s]
Pb-15.7Li temperature	400 – 500	[°C]
Purge/stripping gas	He+H ₂ or He + D ₂	[-]
He stripping composition	He + H ₂ (1000 ÷ 5000)	[vppm]
Material	2 ¼ C – Mo	[-]
Column internal diameter	154.1	[mm]
Height of Pb-15.7Li in the column	1.69	[m]
Bubble column height	765	[mm]
Structured packing height	426	[mm]
Empty weight	360	[kg]

Table 11 – Main design parameters of the saturator.

4.2.5 The gas injection system

The gas injection system (Figure 25) is like a multi-layer cake. Each layer has been perforated to allow the passage of gas. It is positioned at the bottom, to guarantee uniform distribution of the gas. It is injected in counter-current respect to the liquid metal and from the bottom to the top, and it is continuously introduced to prevent the obstructions. The flow is controlled thanks to the mass flow controllers, (Figure 33) and the pressure is controlled thanks to a pressure reducer.



Figure 25 – Gas injection system.

4.2.6 The extractor

The extractor (100-S300), shown in Figure 26, was designed and built to characterize the GLC mock-up. The function of the extractor is to remove the hydrogen/deuterium from the liquid metal alloy.



Figure 26 – Extractor tank.

The structured packing chosen for the extractor is Sulzer Mellapak (Figure 24), with a gas-liquid interfacial surface area of $450 \text{ [m}^2/\text{m}^3]$ for a height of 856 [mm] . Each block of Mellapak is mounted with spacers to keep it in position inside the vessel. There are four modules, twice with respect to the saturator. This choice was made to increase extraction efficiency. The injection system (Figure 25) is located at the bottom.

The heating cables serve to warm up at the operational temperature and they are located on the external surface. The thermocouples are positioned at a different level to detect the temperature of the extractor. The main design parameters are reported in Table 12.

Parameter	Values	U.o.M.
Design pressure	10	[barg]
Operative pressure	5	[barg]
Design temperature	530	[°C]
Operative temperature	500	[°C]
Nominal Pb-15.7Li flow rate	1.2	[kg/s]
Saturator flow rate	10 – 250	[Nl/h]
Pb-15.7Li mass flow rate	0.2 – 4.5	[kg/s]
Pb-15.7Li temperature	400 – 500	[°C]
Purge/stripping gas	He+H ₂ or He+D ₂ (5%) max)	[-]
He stripping composition	He + H ₂ (1000 ÷ 5000)	[vppm]
Material	2 ¼ C – Mo	[-]
Column internal diameter	154.1	[mm]
Height of Pb-15.7Li in the column	1.69	[m]
Bubble column height	765	[mm]
Structured packing height	856	[mm]
Empty weight	330	[kg]

Table 12 – Main design parameters of the extractor.

4.2.7 Permeation sensors

The permeation sensors are the instrument with which the concentration of hydrogen in the Pb-15.7Li is measured. In TRIEX-II, there are three helical sensors called 100-HLM-733, 100-HLM-734, 100-HLM-735. The 100-HLM-733 is at the inlet of the saturator, the 100-HLM-734 is positioned at the outlet of the extractor and at the inlet of the extractor, and the 100-HLM-735 is positioned at the outlet of the extractor. During the normal operation conditions, the sensors are immersed in liquid metal where the hydrogen is dissolved at a certain concentration for the construction of sensors, will be explained in detail in 0.

Three pressure transducers (Figure 27) are used to measure the partial pressure of hydrogen permeated through the helical sensors. They must guarantee a higher accuracy and for this reason; Pfeiffer pressure transducers have been selected. They can guarantee an uncertainty of $\pm 0.15\%$ of the measurement. The main technical characteristics are reported in Table 13.



Figure 27 – Pressure sensor.

The main characteristics of the pressure transducers are in Table 13.

Characteristic	Values	U.o.M.
Model	CMR 372	[-]
Type	Capacitance	[-]
Pressure range	From 10^{-2} to 110	[hPa]
Accuracy	$\pm 0.15\%$ of measured value	[-]
Protection category	IP40	[-]
Flange connection	DN 16 ISO-KF	[-]
Pressure max	2	[bar]
Output signal	1 – 9.8	[V]
Response time	< 3	[ms]
Power consumption	< 12	[W]
Membrane material	Aluminium	[-]
Pipe and flanges	Stainless steel	[-]

Table 13 – Design Characteristics of the pressure transducer Pfeiffer CMR-372.

4.3 The gas system

4.3.1 The gas system Piping and instrumentation diagram

The P&ID is reported in Figure 28.

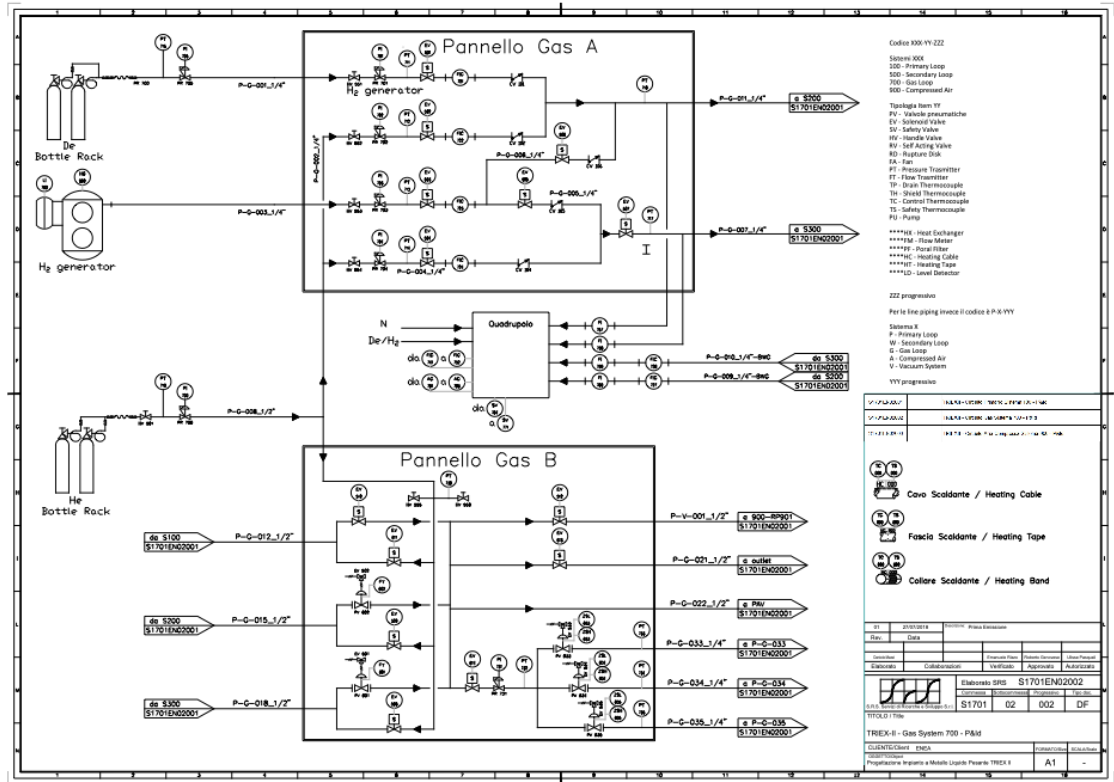


Figure 28 – P&ID of the gas system.

The components that characterize the gas system is positioned on two different skids (Figure 29, Figure 34): the first one named skid A is dedicated to manage and control the vacuum system, while the skid B is dedicated to managing the different gases. The skid B is composed of two mass flow controllers and two mass flow meters, respectively for inlet and outlet of the saturator and the extractor. Also, the skid B is equipped with five manual pressure reducers, to reduce the pressure at the inlet of the gas injection system. The skid A is composed of two vacuum pumps described in the following paragraph, and valves to control the gas line of the whole plant.



Figure 29 – View of the two skids. On the left: skid A; on the right: skid B.

4.3.2 Vacuum system

The vacuum system is composed of two different lines. The first line manages the permeation sensors line; in this case, the vacuum is made thanks to a diaphragm rotary pump, until a certain vacuum degree is reached, then the turbo molecular pump intervenes to reach higher vacuum degree (Figure 30). The main characteristics are reported in Table 14. The second line allows to create the vacuum inside the saturator, extractor and all the pipes the characterize TRIEX-II except for 100-S100, thanks to a rotative pump (Figure 31). The main characteristics are reported in Table 15.



Figure 30 – Pfeiffer 80 Turbo vacuum station.

Characteristic	Values	U.o.M.
Type	Diaphragm-Turbomolecular	[-]
Electrical requirements	110/230	[V]
Pumping speed for N ₂	35	[l/s]
Flange connection	KF40 flange	[-]
Ultimate vacuum	10 ⁻⁷	[mbar]
Output signal	4 – 20	[mA]
Relative humidity	50 % 40 < T < 90	[-]
Noise level	< 52	[dB]
Cooling method	Air cooled	[-]

Table 14 – Main characteristics of a molecular vacuum station.



Figure 31 – Edwards EV12 Vacuum pump.

Characteristic	Values	U.o.M.
Model	EV12	[-]
Type	Rotary vane	[-]
Electrical requirements	220/240	[V]
Pumping speed for N ₂	12	[m ³ /h]
Flange connection	KF40 flange	[-]
Ultimate vacuum	10 ⁻²	[mbar]
Output signal	4 – 20	[mA]
Relative humidity	90 % 40 < T < 90	[-]
Noise level	42	[dB]
Oil capacity	1	[l]
Protection index	IP44	[-]

Table 15 – Main characteristics of a rotative vacuum pump.

4.3.3 The hydrogen generator

For safety reasons, a hydrogen generator (Figure 32) has been purchased: in fact, in order to use cylinders a dedicated outdoor area would be required; moreover, this would have needed an additional gas line to bring hydrogen to the plant with permeation through the pipes. The hydrogen generator is connected to skid B, and the main characteristics are reported in Table 16.



Figure 32 – View of the hydrogen generator.

Characteristic	Values	U.o.M.
Model	AD 300	[-]
Type	Hydrogen generator	[-]
Flow rate	0 – 300	[cc/min]
Minimum pressure	1	[bar]
Maximum pressure	10.7	[bar]
Standard purity	99,9999 at STP	[-]
Input voltage	230	[V]
Power consumption	160	[W]
Noise level	40	[dB]
Pressure accuracy	0.1 (\pm 0.5 %)	[bar]
Protection category	IP20	[-]

Table 16 – Operative parameters of the hydrogen generator.

4.3.4 Mass Flow Controllers

Two mass flow controllers (Figure 33) were installed on TRIEX-II to manage the gas flow rate coming from the saturator and extractor, one for helium and the other for hydrogen.

The mass flow controller is equipped with a regulation valve that allows operating in a range of 0 – 400 [Nl/h]. The valve is controlled by an actuator, composed of a solenoid.



Figure 33 – View of the Bronkhorst mass flow controller [34].

In Table 17, there is the main characteristic of the mass flow controller.

Characteristic	Values	U.o.M.
Model	F201	[-]
Temperature range	10-70	[°C]
Setting time	1-2	[s]
Pressure range	Up to 10	[bar]
Flow rate range	0-400	[Nl/h]
Application	Pure gases	[-]
Supply	24	[V]
Output signal	4-20	[mA]
Material	AISI 316 L	[-]

Table 17 – Main characteristics of the mass flow controller.

4.3.5 Mass spectrometer

A mass spectrometer (Figure 34) is used to analyse the concentrations of hydrogen saturated or extracted. Thanks to the mass spectrometer, the extraction efficiency is verified (Figure 34). The efficiency can be calculated in two ways: indirect way with the permeation sensors and an indirect way with the spectrometer. With the spectrometer is possible calcite the extracted flux. The quadrupole was chosen for the lowest value of Limit of Detection (LOD), respect the others mass spectrometer, of 1 ppb as reported in Table 18. The mass spectrometer is characterized by rapid acquisition times, small sample gas consumption and above all the ability to distinguish the hydrogen from the deuterium. The detection is made by dual Faraday/Channeltron detector, after the detection, the quadrupole uses ventilation out and this allows the system to remain in safety thus avoiding possible breakage. The quadruple uses a turbomolecular pump (TMP) to evacuate the chamber from impurities. The quadrupole mass spectrometer is connected to the plant in six points: at the inlet and outlet of the extractor, at the inlet and at the outlet of the saturator and the last two points are used to the calibration of the spectrometer and for the zero-adjustment (it eliminates gas traces that cannot be removed by the vacuum pump). The gas entering in the quadrupole should not have a pressure higher than the values of atmospheric pressure; moreover, the quadrupole is equipped with heating cables to prevent the formation of condensate inside it that could affect the measurement.



Figure 34 – Front view of the mass spectrometer.

The main parameters that characterize the mass spectrometer are reported in Table 18.

Characteristic	ESS GenesSVs 200 D	U.o.M.
Mass analyser	Quadrupole	[-]
Filament	[not specified]	[-]
Detector	Dual Faraday/Channeltron	[-]
Power	170	[W]
Pumping system	TMP + scroll pump	[-]
Gas intake system	1 capillary of 2 m heated Si	[-]
Inlet gas pressure	750 – 1500	[mbar]
Inlet gas temperature	200 – 350	[°C]
Consumption at the capillary	10 – 200	[sccm]
Mass detection	1– 100	[amu]
Limit of detection	1	[ppb]
Max. detectable concentration	not specified	[-]
Response analysis time	120	[msec]
Chemical species detectable	not specified	[-]
Precision	± 5	[%][
Stability	Not specified	[-]

Table 18 – Main characteristics of the mass spectrometer.

4.4 Differential pressure transducers

The differential pressure transducer (Figure 35) serves to measure the pressure drops in different parts of the system. This also serves to characterize the plant, to calculate the pressure drops in the extractor that will be used to validate the CFD model. The main parameters are reported in Table 19.



Figure 35 – View of the differential pressure transducer.

Characteristic	Values	U.o.M.
Pressure	± 20.7	[bar]
Process connection	flanged	[-]
Electrical connection	2 cables	[-]
Accuracy	± 20	[%]
Response time	500	[ms]
Capillary length	1.5	[m]
Output signal	4 – 20	[mA]

Table 19 – Operative Characteristics of the pressure transducer.

4.5 Pb-15.7Li valves

The Pb-15.7Li valves (Figure 36) are used to control the mass flow rate of Pb-15.7Li during the drainage phase of the plant and to control the mass flow rate to the extractor. These two valves are placed in the primary loop of TRIEX-II. The drain valve is positioned in the pipeline connecting the storage tank to saturator and the extractor.

The two valves which are proportional can be opened or closed by an actuator. The actuator is also provided reading to know the degree of opening or closing.



Figure 36 – View of the Pb-15.7Li valve.

The main characteristics of the Pb-15.7Li valves are reported in Table 20.

Characteristic	Technical characteristics
Model	Technoflow i-FGS
Type	Ball valve
Positioner	Electro-pneumatic
Actuator	Pneumatic
Position	Normally open

Table 20 –Characteristics of the Pb-15.7Li valve.

4.6 Thermocouples

Type k thermocouples (Figure 37) are used to measure the temperature in TRIEX-II. The operating principle is based on the variation of the electrical resistance of a metal to the variation of the temperature, so in according to the resistance variation the thermocouples sends an electrical signal to a CPU.

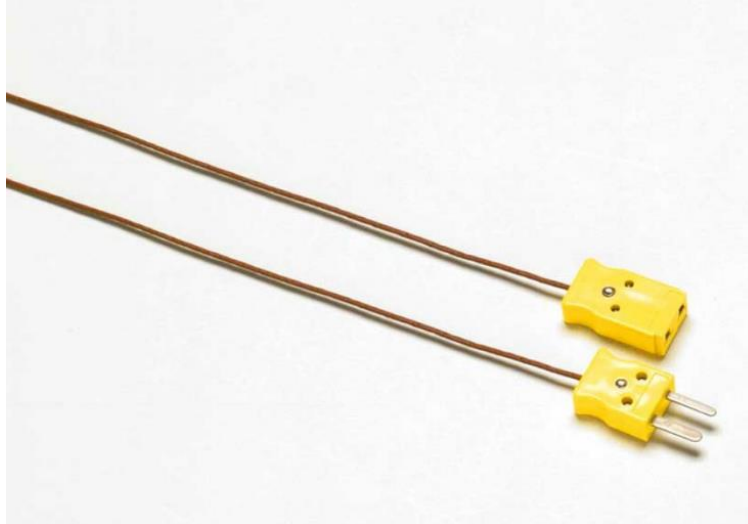


Figure 37 – Type K thermocouples [36].

5 Permeation sensors

The permeation sensors play a key role in the characterization of the efficiency of the Gas-Liquid contactor. Therefore, it is important to study them in depth to better understand how to design and build them. For the construction and design of the sensors, several technical requirements that will be listed and explained in figure 38. To identify the technological requirement, first of all, it is necessary to understand what its function will be. Once the function has been identified, it is important to understand the physics of the problem and consequently, all the physical parameter that will be essential for its functioning.

5.1 Physical principles of permeation sensors

The permeation sensors exploit the permeation process (figure 38). The permeation process involves tritium passing through a metal membrane. It is characterized by several physical phenomena as diffusivity, permeability, surface adsorption, desorption [22].

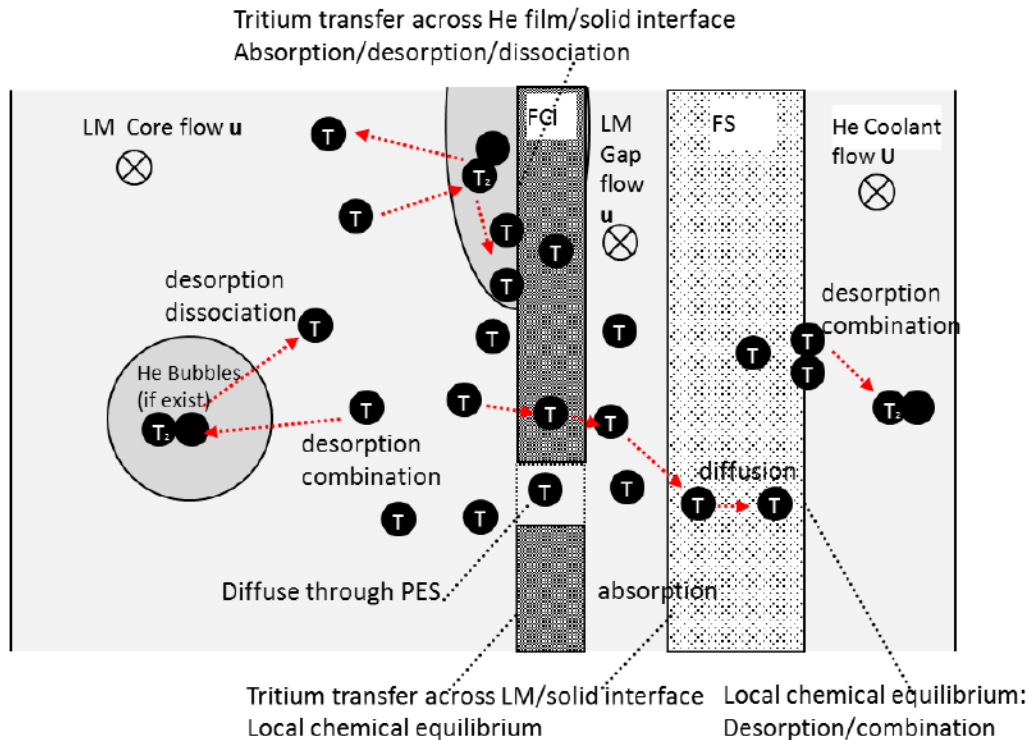


figure 38 – permeation process through a membrane [18].

The permeability through the membrane is based on two different regimes: Diffusion Limited Regime (DLR) and the Surface Limited Regime (SLR). A characteristic parameter named permeation parameter W [-] is used to distinguish the two types of regime, if $W \ll 1$ the regime is surface limited, while if $W \gg 1$ the regime is diffusion limited. Limited means that high partial pressure of the species i [37].

The permeation parameter manages to group in a single value all the physical parameters

that come into play in the permeation process, and it is defined:

$$W = \frac{K_r K_s}{D_i} t_0 \sqrt{p_i} \quad (11)$$

where k_r is the recombination constants [$m^4/(s \text{ mol})$], k_d is the dissociation constant [$(s \cdot mol)/(kg \cdot m)$], D_i is the diffusion constant of the species [m^2/s], t_m is the thickness of the membrane [m] and p_i [Pa] is the partial pressure of the species.

Technological requirements

The technical requirement for the choice of the best material for the construction of the permeation sensors are:

- High permeability;
- High resistant to the temperature;
- High diffusivity;
- Low value of K_s ;
- Corrosion resistance;
- Malleability;

The sensor membrane must be characterized by high permeability, to facilitate the passage of the hydrogen. It is having a low value of Sieverts' constant because the hydrogen does not solubilize within the membrane. The hydrogen must have high diffusivity, to make that the substance moves quickly inside the metal. The membrane must have a high value of adsorption and desorption because the substance must be absorbed before diffusing and must be released to exit once it has travelled across the membrane. For the material of the membrane must have high resistance to the corrosion at high temperature because the Pb-15.7Li erodes the metals. A fundamental role is the malleability of the material because the sensors must be easily machinable.

5.2 Design of permeation sensors

In TRIEX there were three cylindrical sensors (Figure 39), developed at ENEA C.R. Brasimone. The sensors have been designed to minimize the volume occupied by hydrogen with a S/V (Surface [m^2], Volume [m^3]) = 416 [-]. The internal filler has been made of aluminium coated with gold. These materials have been chosen to respect the technological requirement reported in 0, it has the characteristics indicated in Table 21 [38].

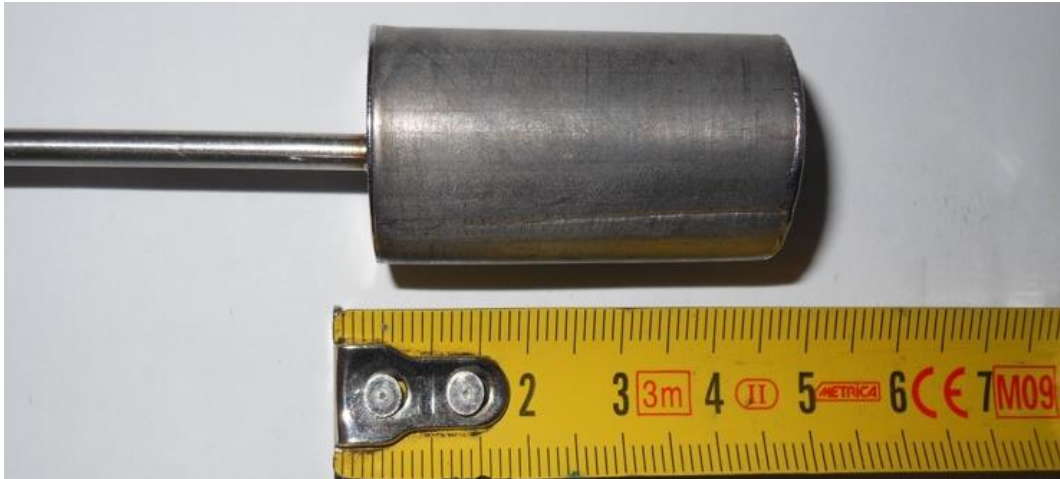


Figure 39 – Cylindrical sensor of TRIEX.

Parameter	Values	U.o.M.
Height	40	[mm]
Outer diameter	20	[mm]
Wall thickness	0.2	[mm]
Base thickness	0.2	[mm]
Top thickness	0.2	[mm]

Table 21 – Main parameters of the cylinder sensor.

New permeation sensors have been developed in TRIEX-II to speed up the response time by maximizing the L/G ratio. To maximize L/G a new configuration is chosen, from a cylindrical geometry to a helical geometry. The final sensor configuration consists of three concentric helices with different diameters and number of windings and with S/V ratio =3125.

The final sensor configuration (Figure 40, on the left) consists of three concentric helices with different diameters and number of windings. The helical sensor is made by routing a thin cylinder around a matrix (Figure 40, on the right).

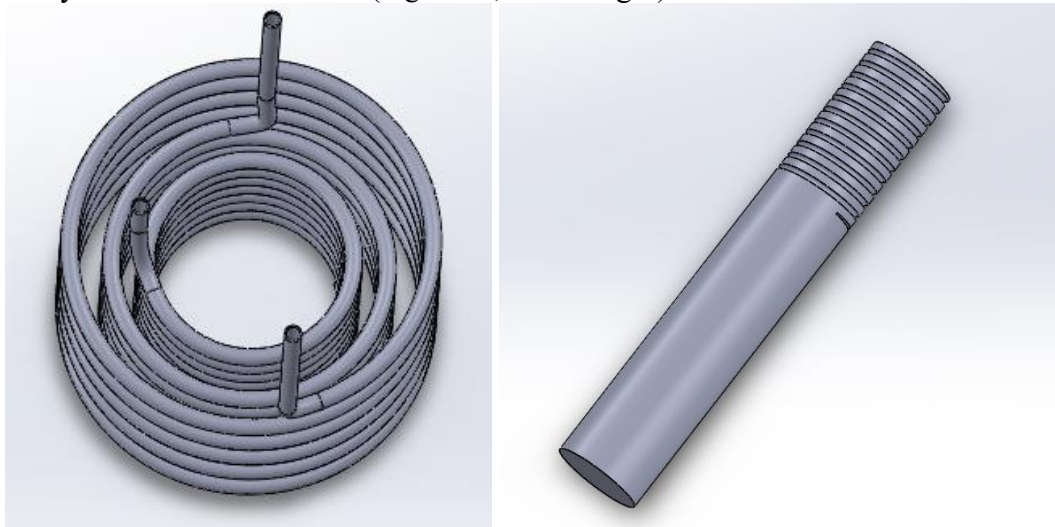


Figure 40 – On the left: final configuration of TRIEX II permeation sensor; on the right: matrix to build the helices.

The Table 22, shows the geometry data of the three helices.

Parameter	Values	U.o.M.
Height	40	[mm]
Outer diameter	30, 35, 42	[mm]
Wall thickness	0.2	[mm]
Total length	700, 400, 700	[mm]
Number of coils	7.5, 5.5, 5.5	[-]

Table 22 – Main parameters of the three helices.

In the Figure 41 is represented the smallest propeller that will go to brush the sensor.



Figure 41 – Helical sensor.

The three helices are connected to a Swagelok cross (Figure 43) to be related to the vacuum pump and pressure sensors. A Swagelok pipe of 1/8" is used to connect the helices with the cross. It is composed of two elements the rings (Figure 42), which serves to screw to the cross, and the ferula that serves to ensure the vacuum seal. The lower part of the helices has been welded, using a special technique using the laser.



Figure 42 – Swagelok connection of 1/8".

Thanks to the cross (Figure 43) it is possible to interconnect the three sensors and positioned them in the correct position to carry out their task.

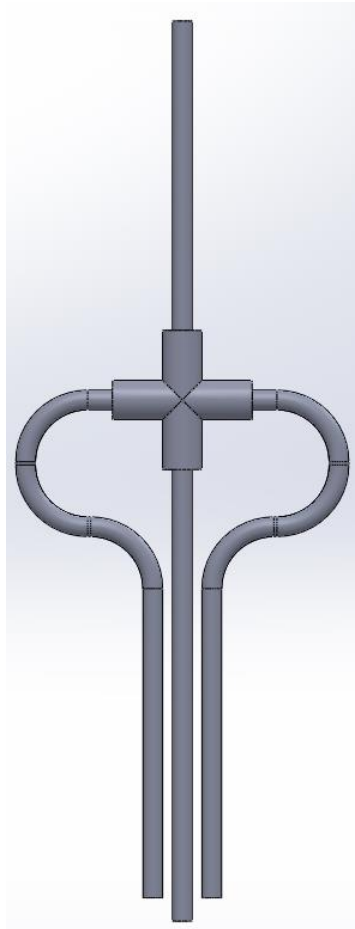


Figure 43 – Cross connection with the permeation sensors.

5.3 Liquid phase model description

In order to perform different analyses for different possible configurations a numerical simulation has been implemented. Creating a numerical model makes it possible to study other possible geometries of permeation sensor.

A liquid phase model has been implemented because the sensors have to go to measure the concentration of hydrogen in the Pb-15.7Li.

In the liquid phase, the sensor is immersed in isothermal lithium lead and hydrogen diffuses through it to reach the vacuum side. In Figure 44 the geometry used for the model is shown. The whole domain is assumed as 2D-axisymmetric to simplify the simulations.

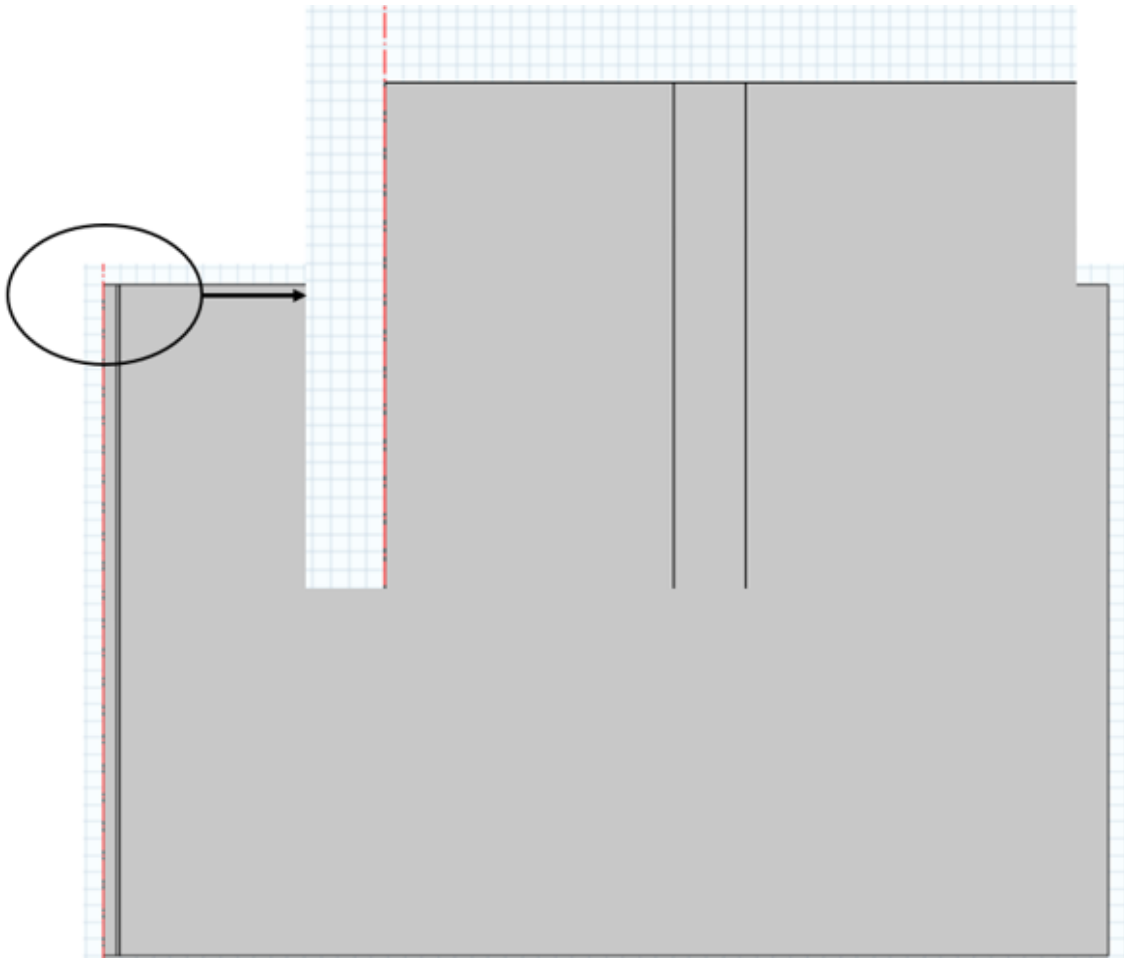


Figure 44 – Whole domain of the simulation.

The iron sensor works in equilibrium mode: starting from vacuum conditions, the pressure inside the chamber of the sensor increases due to the hydrogen permeation from the Pb-15.7Li through the sensor walls. The sensor wall is 0.2 mm thick and H₂ permeates through it to fill the chamber. A passive scalar transport equation can be written for the hydrogen species:

$$\frac{\partial c_i}{\partial t} = \nabla(D_i \nabla c_i) - \vec{u} \nabla c + S_i \quad (12)$$

where c_i [mol/m³] is the concentration in the i -th domain (Pb-15.7Li, α -iron, hydrogen gas), D_i [m²/s] is the diffusivity, \vec{u} [m/s] is the velocity and S_i [mol/(m³s)] is the source term. In this case, $\vec{u} = 0$ and $S_i = 0$, so the equation for each domain becomes:

Hydrogen is monoatomic in solution with the metals and it recombines on the iron surface in contact with the vacuum side.

where $c_{H,PbLi}$ [mol/m³] is the concentration of hydrogen in the metal, K_s [mol/(m³ Pa^{0.5})] is the Sieverts' constant and p_{H_2} [Pa] is the partial pressure of hydrogen in the metal. To solve the diffusion equation, the diffusivity of hydrogen in the different materials is needed.

5.3.1 Initial conditions

At $t = 0$ lithium lead is saturated with hydrogen at a partial pressure of 500 [Pa] and concentration can be evaluated from Sieverts' law. Instead, in iron concentration is equal to zero and inside the sensor a non-perfect vacuum is supposed, evaluating a starting concentration as:

$$C_{sens} = \frac{p_0}{RT} \cdot 500 \quad (13)$$

where p_0 [Pa] is the ultimate vacuum pressure of the pump.

5.3.2 Boundary conditions

At the interface Pb-15.7Li/Fe a pressure continuity condition between hydrogen in Pb-15.7Li and hydrogen in iron is imposed and it can be written as follows [1]:

$$\frac{C_{H,Fe}}{C_{H,PbLi}} = \frac{K_{S,Fe}}{K_{S,PbLi}} = K \quad (14)$$

In this way a partition coefficient K [–] is defined as the concentration of hydrogen in iron divided the concentration of hydrogen in Pb15.7Li, so the concentration at the iron side of the interface can be evaluated. Initially there is a vacuum inside the sensor, after permeating through the iron thickness, the hydrogen goes to inside the sensor thanks to a self-diffusion process. The net flux of hydrogen at Fe/gas interface can be written:

$$J_H = K_{d,H_2} p_{H_2} - K_{r,H} c_H^2 \quad (15)$$

$$J_H = 2 J_{H_2} \quad (16)$$

where J_H [mol/(m² s)] is the net flux of monoatomic hydrogen, K_d [mol/(m² s Pa)] is the dissociation constant, p_{H_2} [Pa] is the pressure of hydrogen in the gas phase, K_r [m⁴/(mol s)] is the recombination constant, $c_{H,Fe}$ [mol/m³] is the concentration of hydrogen in iron at the boundary. Pressure in the gas domain can be calculated from the ideal gas law, assuming that the temperature is constant during the whole process:

$$p = \frac{n}{V} RT = cRT \quad (17)$$

where p [Pa] is the pressure of the gas, V [m³] is the volume, n [mol] is the number of moles, R [J/(mol K)] is the universal gas constant and T [K] is the temperature, c is the

concentration of the gas [mol/m³].

The solubility of hydrogen in metals obeys the Sieverts' law.

$$c_{H,PbLi} = K_s \sqrt{p_{H_2}} \quad (18)$$

5.3.3 Mesh choice

For the simulation, the mapped mesh (Figure 45) has been chosen because of:

- The physics: this type of mesh is better for solving species transport problems;
- Geometry: the geometry is rectangular;
- Quality mesh parameter: the skewness angle is equal to 1, the warped cells are $\alpha < 75^\circ$, there are not a non-orthogonal cells near the boundary, there are non-tetrahedral elements in boundary layers because the mesh is 2D, there are not discontinues, there are not a presence of arbitrary mesh coupling because COMSOL imposes an algorithm to avoid this problem;
- the number of cells is considerably lower and so it is possible to decrease the numbers of elements by reducing the computational cost;

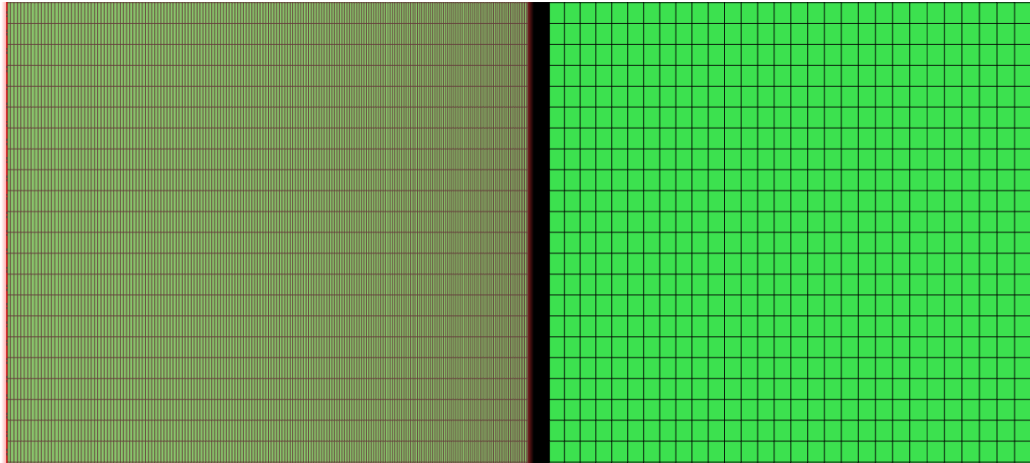


Figure 45 – Mapped mesh.

On the left, the internal domain of the sensor is represented, in the center, there is the iron thickness, on the right, there is the Pb-15.7Li domain. It is possible to notice that the mesh is denser near the edge between iron-hydrogen and between iron-Pb-15.7Li to ensure that in those areas there are more cells. This has been done to ensure a more precise calculation near the edge between iron-hydrogen and between iron-Pb-15.7Li.

5.3.4 Transport properties

In Table 23 there are the main transport parameters that were used in the 2-D simulation.

Property	Correlation	Value	U.o.M.	Ref.
Sieverts' constant	$K_{PbLI} = 0.0013 \cdot \exp\left(-\frac{1350}{R \cdot T}\right)$	0.0011	[mol/m ³]	[4]
Self-diffusivity H ₂	$D_{H_2} = 1.123 \cdot 10^{-5} \frac{T^{\frac{3}{2}}}{T^{\frac{3}{2}}}$	4.4·10 ⁻⁴	[m ² /s]	[5]
Diffusion coefficient	$D = 2.5 \cdot 10^{-7} e^{-\frac{27000}{RT}}$	2.8·10 ⁻⁹	[m ² /s]	[6]
Diffusion coefficient	$D_{Fe} = 5.12 \cdot 10^{-8} \cdot \exp\left(-\frac{500}{T}\right)$	2.58·10 ⁻⁸	[m ² /s]	[7]
Permeability of H in Fe	$\Phi = 4.1 \cdot 10^{-8} \cdot \exp\left(-\frac{4200}{T}\right)$	1.2·10 ⁻¹⁰	[mol/mPa ^{0.5}]	[8]
Recombination constant	$K_r = 3 \cdot 10^{-27} \cdot N_A$	0.0018	[m ⁴ /mol]	[9]

Table 23 – Preliminary properties for the simulation.

5.3.5 Parametric analysis Sieverts' constant

One of the most important parameters of the transport model is the Sieverts' constant. To the parametric analysis on the Sieverts' constant are chosen, three different correlations are chosen, and they are shown in Table 24. The trend of the different pressures is reported in Figure 46 and the values are reported in Table 24.

Correlation	Correlation	Value at T = 673 [K]	U.o.M.
Reiter	$K_{PbLI} = 0.0013 \cdot \exp\left(-\frac{1350}{R \cdot T}\right)$	0.0011	[mol/(m ³ · Pa ^{0.5})]
Chan-Veleckis	$K_{PbLI} = 0.0258 \cdot \exp\left(-\frac{9000}{R \cdot T}\right)$	0.0058	[mol/(m ³ · Pa ^{0.5})]
Aiello	$K_{PbLI} = 0.237 \cdot \exp\left(-\frac{12844}{R \cdot T}\right)$	0.0280	[mol/(m ³ · Pa ^{0.5})]

Table 24 – Sievert's constant of H in Pb15.7Li [39].

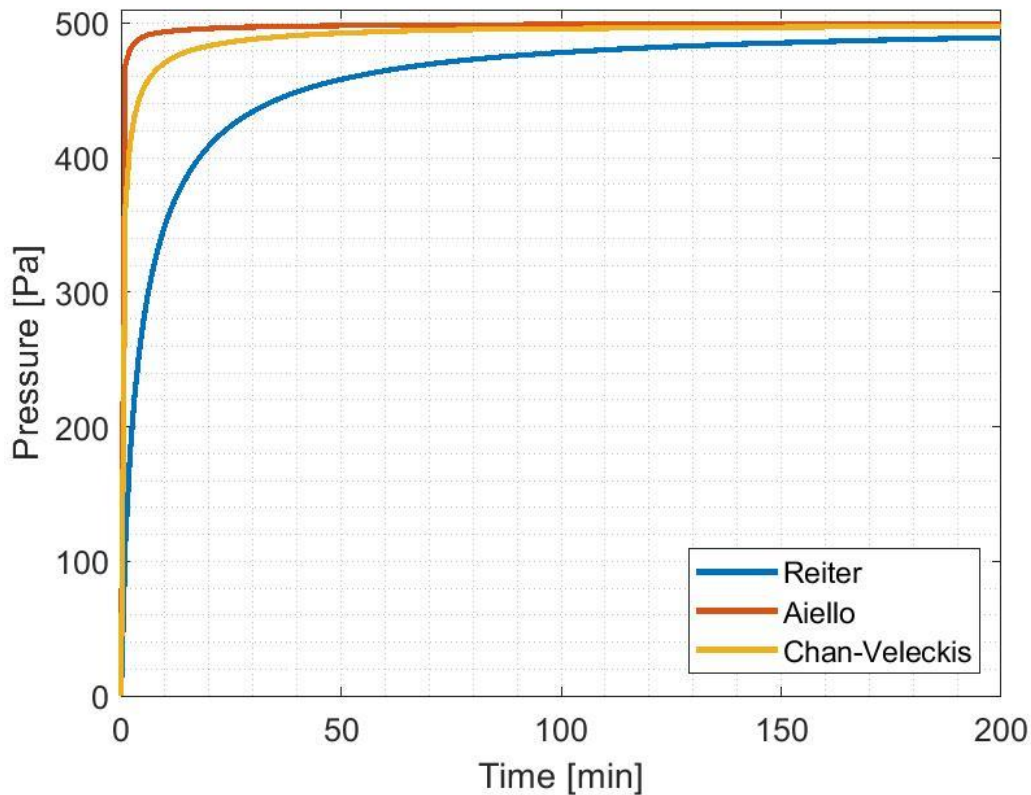


Figure 46 – Pressure trend of the Sieverts' constant.

The sievert's constant is linked to a very high uncertainty, as shown in Table 25, The values of the constant can vary in orders of magnitude, this entails a considerable difference on the t.

$K_{s, H-Pb15.7Li}$ [mol/(m ³ · Pa ^{0.5})]	Value [mol/(m ³ · Pa ^{0.5})]	t* [min]
Reiter	0.0011	40
Chan-Veleckis	0.0058	5
Aiello	0.0280	1

Table 25– Value of t* changing the Sieverts' constant.

The results obtained with Reiter's correlation for Sieverts' constant differ considerably from the other two. For the following analyses, it has been chosen Reiter's correlation because the time to reach it is the one closest to the values obtained with the experiment.

5.3.6 Surface-to-Volume (S/V) ratio.

The ratio S/V is an important parameter to analyse different geometries and response time of the sensor. From the ideal gas law, it resulted that Eq. 21 so, if the value S/V is low, the value of pressures will remain lower, and it takes more time to reach the desired pressure's value (Figure 47).

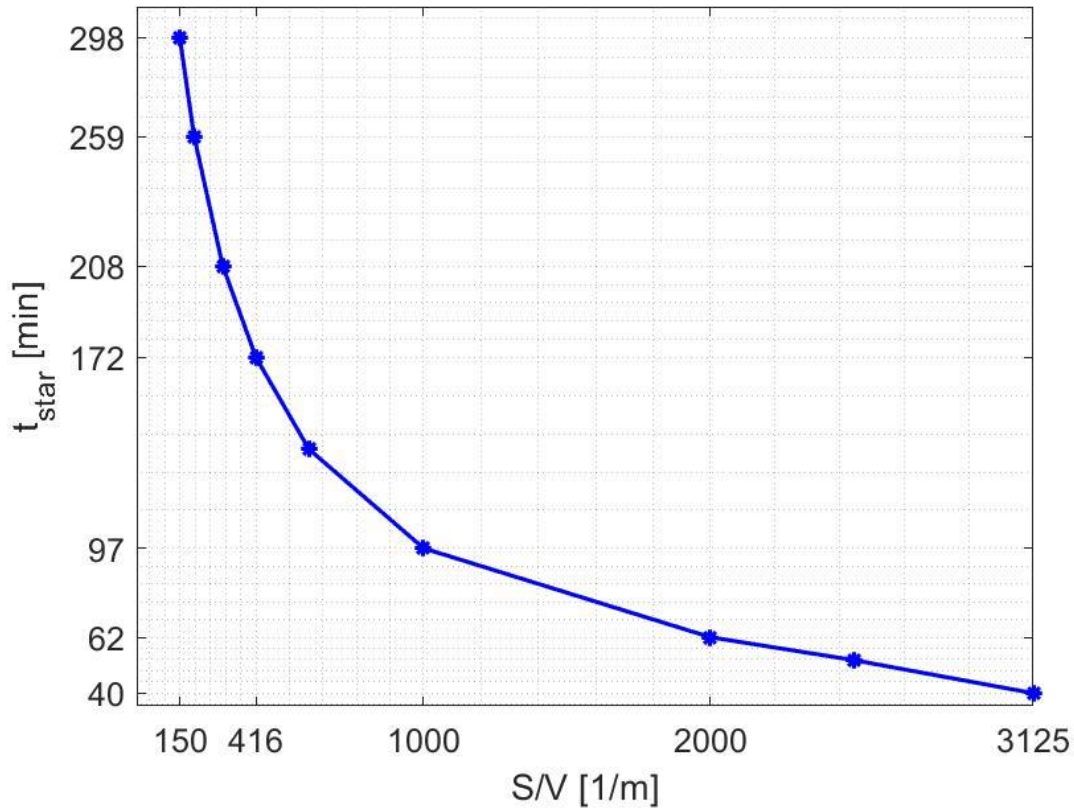


Figure 47 – S/V trend.

In Table 26, the values of 90% of the equilibrium pressure with the mass balance error in the sensor side and the mass balance error in Pb-15.7Li domain are reported. This analysis has served to verify, how the response time of the helical sensor is lower about 130 [min] respect to the cylindrical sensor (Figure 47).

S/V [1/m]	t* [min]	M.B Sensor [%]	M.B Pb-15.7Li [%]
150	298	2.77	2.5
200	259	0.616	0.56
300	208	0.35	0.31
416	172	3.47	3.15
600	136	2.27	2.03
1000	97	2.29	2.11
2000	62	0.34	0.2
2500	53	1.03	0.81
3125	40	2.03	1.02

Table 26 – Value of t^* changing S/V ratio with the mass balance error.

If the S/V ratio increases, the time to reach 90% of the equilibrium pressure decreases: this is the reason for which helical sensors will be used.

5.3.7 Parametric analysis of the temperature

Another parameter is the temperature, because of influences transport phenomena. For the analyses, three different temperatures 603 (DEMO operation), 623, 673 (TRIEX II operation), 773 [K] (Figure 48) are been chosen. The values of t^* are reported in Table 27.

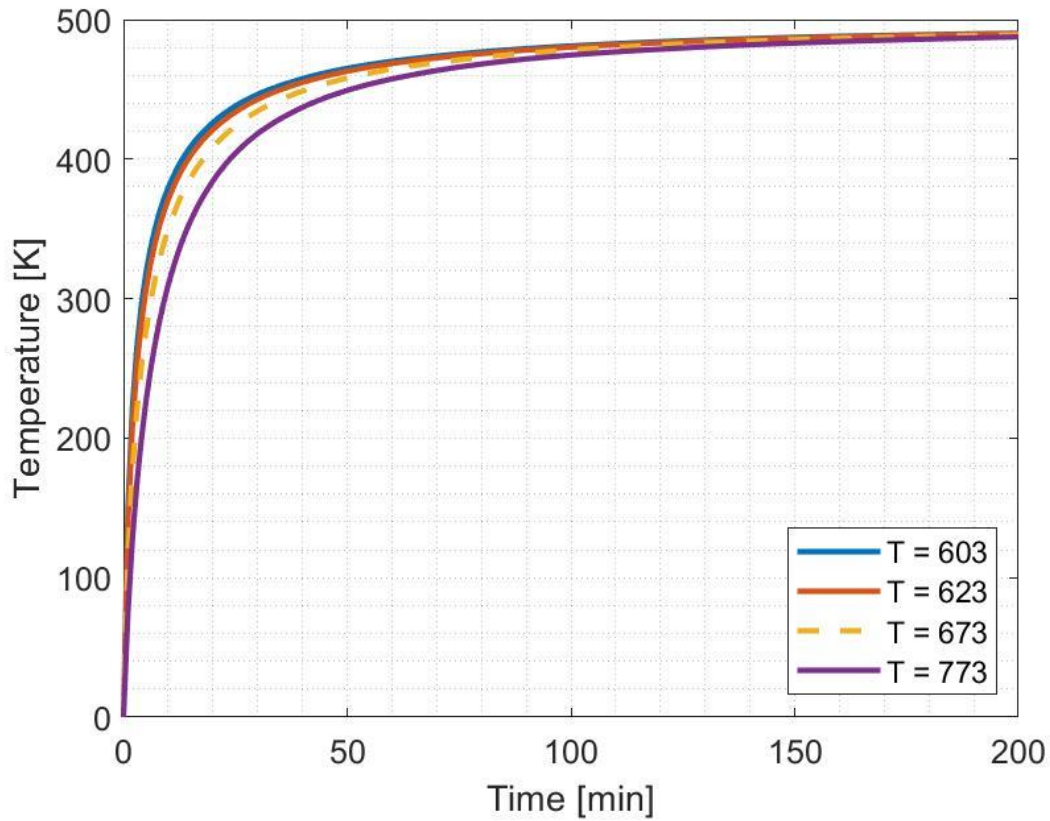


Figure 48 – Pressure trend with temperature sweep.

Temperature [K]	t^* [min]
603	30
623	36
673	40
773	50

Table 27 – Value of t^* changing the temperature.

The t^* increases with the temperature, this is due to the fact that iron diffusivity and iron permeability increase with the temperature, this involves that Sieverts' constant increases with the temperature because the Sieverts' constant is calculated as the ratio between the permeability divided the diffusivity.

5.3.8 Sensor wall thickness

the sensor wall thickness has a greatly influences in the transport phenomena. For the analysis, three different thicknesses 0.1, 0.2, 0.4, 0.5 [mm] are chosen. The t^* values and trends are reported respectively in Figure 49 and in Table 28.

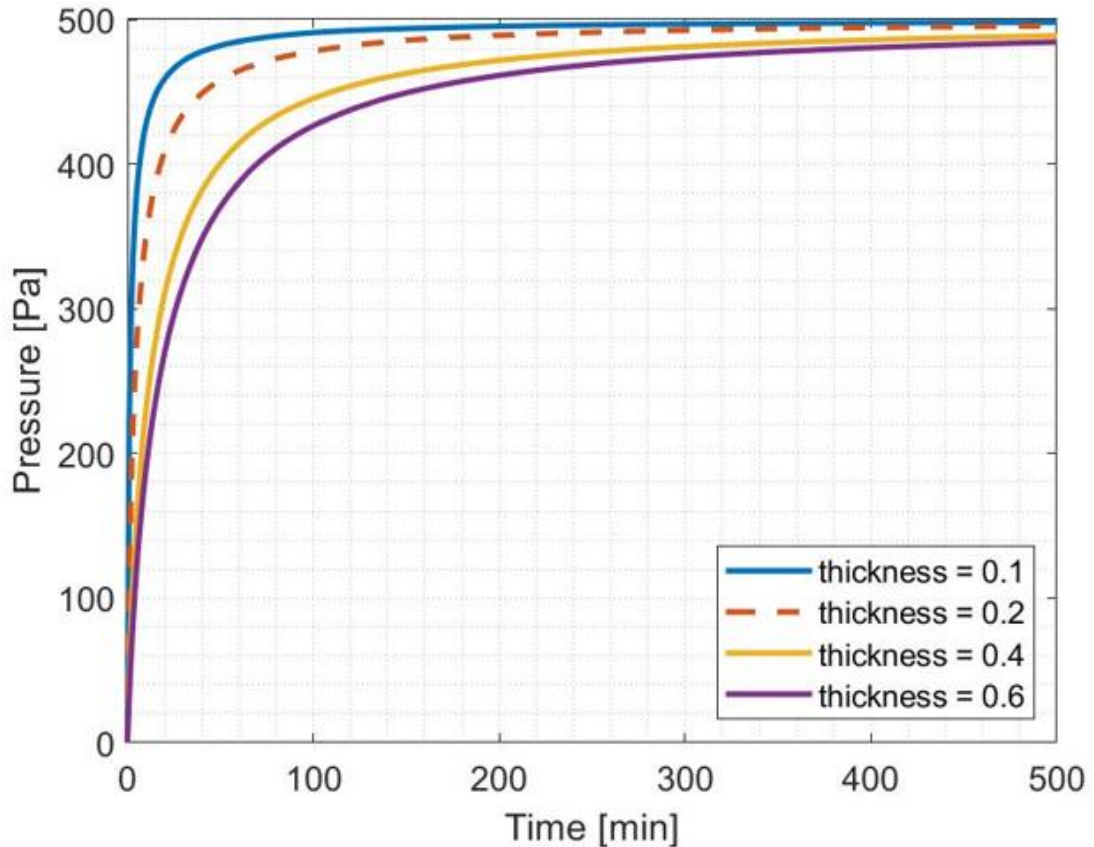


Figure 49 – Pressure trend with thickness sweep.

analysis, three different thicknesses 0.1, 0.2, 0.4, 0.5 [mm] are chosen. The t^* values and trends are reported respectively in Figure 49 and in Table 28.

Thickness [mm]	t^* [min]
0.1	40
0.2	40
0.4	110
0.6	141

Table 28 – Value of t^* changing the sensor thickness.

Increasing the thickness of the wall, the time to reach 90% of the equilibrium pressure increases, because the hydrogen will have to diffuse in a bigger thickness.

5.3.9 Parametric analysis of the Pressure

This analysis was made changing the value of the hydrogen pressure 100 [Pa], 500 [Pa], 100000 [Pa] 5.1. Changing the hydrogen pressure changes the type of transport regime: SLR (surface limited regime), DLR (diffusion limited regime) or mixed regime, because of the change of the permeation parameter W_H 5.1. The permeation parameters are reported in Table 29.

Pressure [Pa]	W_H
100	0.68
500	1.51
10000	21.34

Table 29 – Value of W_H changing pressure.

The choice of these three pressures is made to analyse the three possible surfaces: surface limited $W_H = 0.68$, mixed regime $W_H = 1.51$, and diffusion limited $W_H = 21.34$.

The S/V ration in function of the different pressures is in Figure 50.

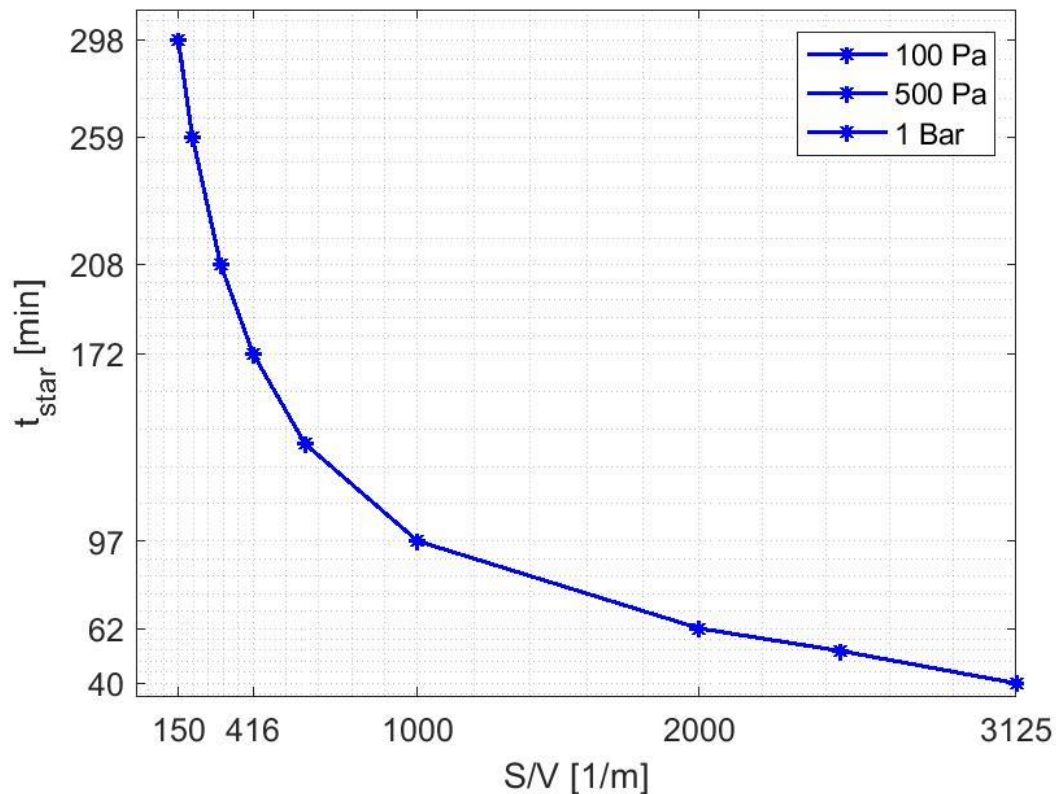


Figure 50 – S/V trend with pressure sweep.

S/V [1/m]	t* [min], p=100 [Pa]	t* [min], p=500 [Pa]	t* [min], p=1 [bar]
150	298	298	298
200	259	259	259
300	208	208	208
416	172	172	172
600	136	136	136
1000	97	97	97
2000	62	62	62
2500	53	53	53
3125	40	40	40

Table 30 – Value of t* changing pressure and S/V ratio.

Changing the type of diffusion regime t* does not change, this is due to the fact that increasing the value of pressure, the number of the interstitial sites that participate in hydrogen transport increase Table 30.

5.4 Verification of the model

To validate the simulation two meaningful experiments are take into account, in particular, the experiment of 15th April and the experiment of 7th-8th.

To validate the simulation three types of error are taken into account:

- The integral error, that is calculated as the absolute value of the ratio between the area under the experimental curve and the area under the theoretical one:

$$e_{\text{int}} = 100 \cdot \left| 1 - \frac{\int_{t_{\text{start}}}^{t_{\text{end}}} p_{\text{H}_2,\text{th}}(t) \cdot dt}{\int_{t_{\text{start}}}^{t_{\text{end}}} p_{\text{H}_2,\text{exp}}(t) \cdot dt} \right| \quad (19)$$

where $p_{\text{H}_2,\text{th}}$ [Pa] is the theoretical values of the hydrogen pressure, while $p_{\text{H}_2,\text{exp}}$ is the hydrogen pressure of the experiment.

- The response time error, that is calculated as the absolute value of the ratio between the response time to reach 90% of the equilibrium value of the sensor t_{exp}^* , and the time to reach 90% of the equilibrium value of the simulation t_{th}^* :

$$e_t = 100 \cdot \left| 1 - \frac{t_{\text{th}}^*}{t_{\text{exp}}^*} \right| \quad (20)$$

- Accuracy error, this error indicates the accuracy of the value to reach the equilibrium between the experimental value $p_{\text{end,exp}}$ and the simulation value $p_{\text{end,th}}$:

$$e_{\text{acc}} = 100 \cdot \left| 1 - \frac{p_{\text{end,th}}}{p_{\text{end,exp}}} \right| \quad (21)$$

The experimental value of Sieverts' constant has been found, thanks to a sweep parametric analysis. The obtained Sieverts' constant is one order of magnitude lower than the value calculated by Reiter.

5.4.1 The Experiment of 15th April 2019

The permeation sensor HLM 734, start from zero up to the hydrogen partial pressure

of 433 [Pa] in the Pb-15.7Li, while the characteristic parameters of the simulation are listed in Table 23. The permeation parameter is equal to 1.014, this means that the permeation regime is in a mixed regime. In the (Figure 51) there is a comparison between the theoretical trend with the experimental trend, while the three errors are reported in Table 31.

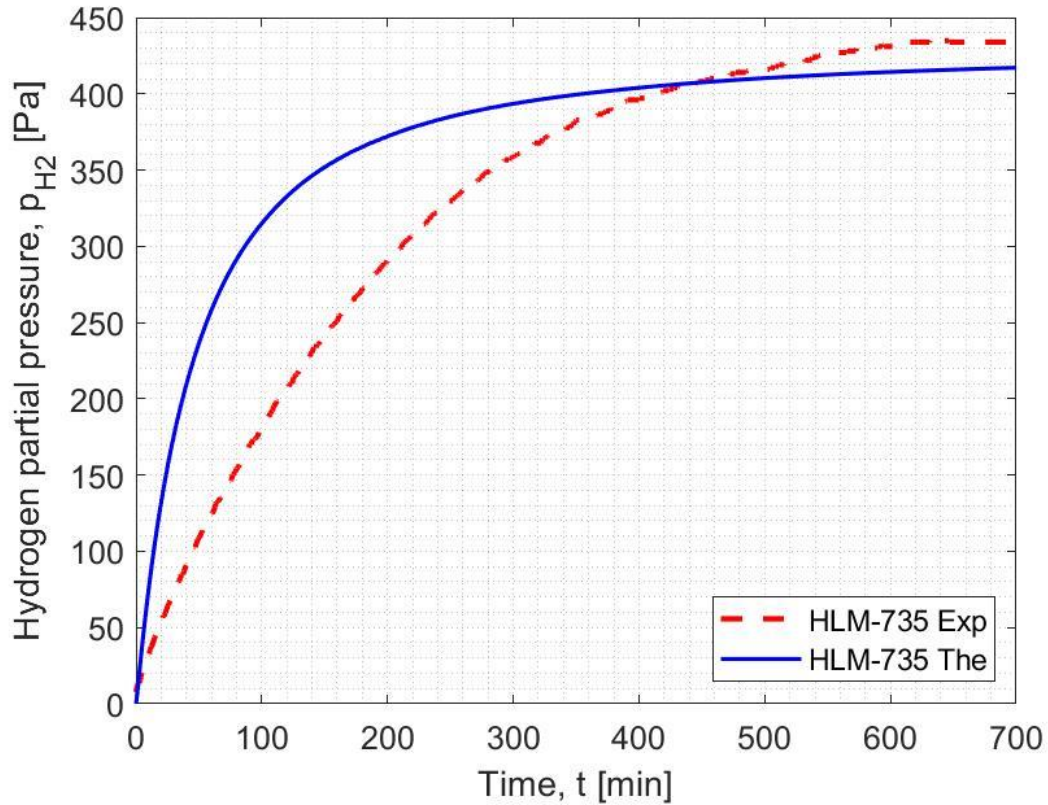


Figure 51 – Comparison between the theoretical trend with the Experimental value.

e_t [%]	e_{int} [%]	e_{acc} [%]
2.94	4.56	6.2

Table 31 – Error Values.

5.4.2 The experiment of 7th- 8th May

The permeation sensor HLM 734, start from zero up to the hydrogen partial pressure of 48 [Pa] in the Pb-15.7Li, while the characteristic parameters of the simulation are listed in Table 23. The permeation parameter is equal to 0.34, this means that the permeation parameter is near to the surface limited regime. The comparison between the theoretical trend with the experimental trend (Figure 52) and in Table 32.

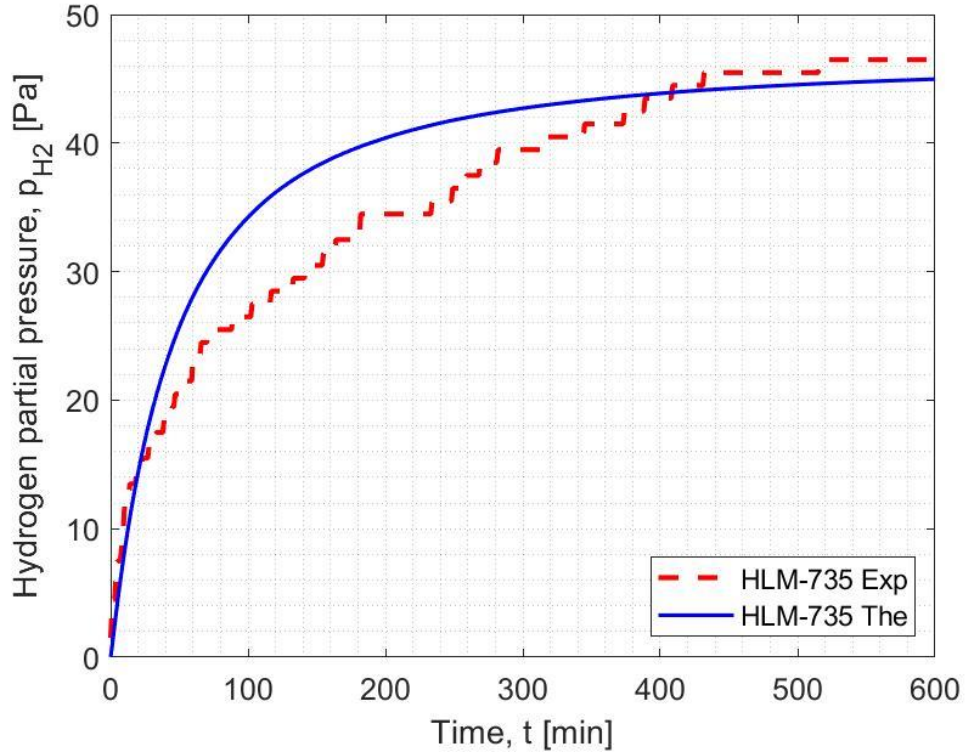


Figure 52 – Comparison between the theoretical trend with the Experimental value.

e_t [%]	e_{int} [%]	e_{acc} [%]
15.6	4.25	4.15

Table 32 – Errors values.

5.5 Experimental analysis

The experimental campaign was conducted at two reference temperatures of 400 [°C], and 450 [°C], respectively. For each temperature, the stripping port has been changed as this was done to be able to evaluate if there is a correlation between the stripping flow and the extraction efficiency. The stripping port has been changed. The extraction efficiency has been calculated using the permeation sensors installed in TRIEX-II.

5.5.1 Evaluation of the extraction efficiency with the permeation sensors

To calculate the extraction efficiency through permeation sensors the basic definition of extraction efficiency is used:

$$\eta = \frac{C_{in} - C_{out}}{C_{in}} = 1 - \frac{C_{out}}{C_{in}} \quad (22)$$

where C_{in} is the concentration of hydrogen at the inlet of the extractor $\left[\frac{\text{mol}}{\text{m}^3\text{s}}\right]$, C_{out} is the concentration at the outlet of the extractor $\left[\frac{\text{mol}}{\text{m}^3\text{s}}\right]$. Thanks to the Sieverts' constant the equation 1 can be rewritten:

$$\eta = 1 - \frac{K_s \sqrt{P_{in}}}{K_s \sqrt{P_{out}}} \quad (23)$$

Where the K_s is the Sieverts constant $\left[\frac{\text{mol}}{\text{m}^3\text{Pa}^{0.5}}\right]$, P_a is the pressure of hydrogen [Pa] at the inlet and at the outlet of the extractor.

Simplifying the Sieverts' constant gives the final formula of efficiency. It is the only function of the pressure at the inlet and at the outlet of the extractor.

$$\eta = 1 - \frac{\sqrt{P_{in}}}{\sqrt{P_{out}}} \quad (24)$$

The efficiency does not depend on the Sieverts' constant, so the efficiency is free of the great uncertainty linked to the constant.

To evaluate the extraction efficiency are taken two significant experiments: the first one is of 18/19 April. In Table 33, the mean parameters of the experiment are reported.

Parameters	Value	U.o.M.
Component	Extractor	[-]
Pressure in 100HLM733	1.971	[mbar]
Pressure in 100HLM734	1.87	[mbar]
Pressure in 100HLM735	1.32	[mbar]
Pb-15.7Li Temperature	403	[°C]
Pb-15.7Li mass flow rate	1.35	[kg/s]
Gas stripping flow rate range S300	179	[NI/h]

Table 33 – Initial values of the experiment.

The efficiency is evaluated as:

$$\eta = 1 - \frac{\sqrt{100\text{HLM735}}}{\sqrt{100\text{HLM734}}} \quad (25)$$

The mean value of efficiency for the entire experiment is = 16.2 % (Figure 53).

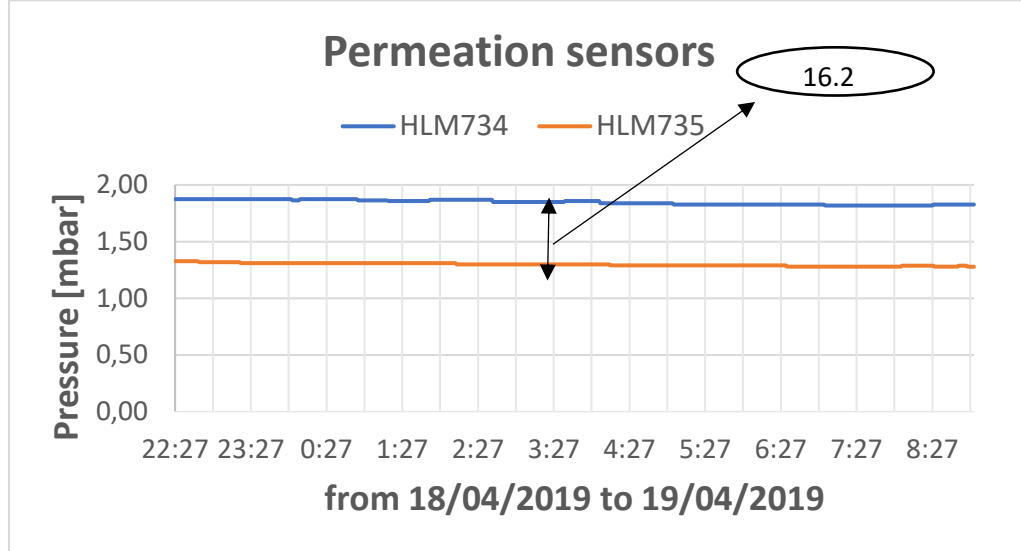


Figure 53 – The trend of the permeation sensors.

The pressure trend for the experiment 18/19 April is shown in Figure 53.

The second test considered is the one of 14 May. In Table 34, the mean parameters of the experiment are reported.

Parameters	Value	U.o.M.
Component	Extractor	[-]
Pressure in 100HLM733	0.98	[mbar]
Pressure in 100HLM734	1.227	[mbar]
Pressure in 100HLM735	1.12	[mbar]
Pb-15.7Li Temperature	403	[°C]
Pb-15.7Li mass flow rate	1.12	[kg/s]
Gas stripping flow rate range S300	130	[Nl/s]

Table 34 – Initial values of the experiment.

The mean value of efficiency for the entire experiment is = 6.5 % (Figure 54).

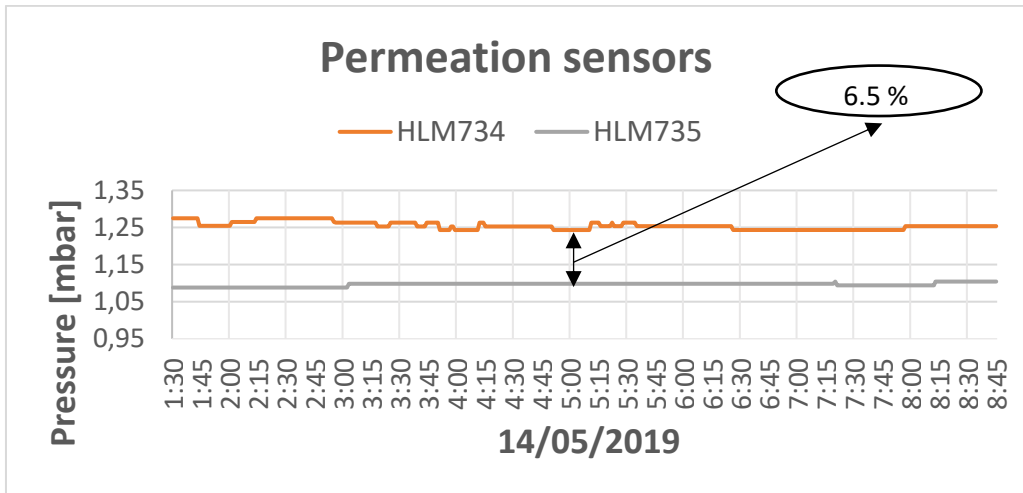


Figure 54 – Trend of the permeation sensors.

6 Simulation of the saturator and extractor

6.1 CFD analysis of the extractor

The aim of the CFD analysis is to evaluate the pressure drop and compare the results obtained to the experimental values. In this analysis is used RANS models K- ϵ to evaluate pressure drops and the velocity field.

A fluid dynamic model is based on the resolution of the Navier-Stokes equations. In particular, it is based on the resolution of two equations: conservation of mass and conservation of momentum. The mass and momentum equation can be written in general form as: [40]:

$$\frac{\partial \rho}{\partial t} + \frac{\partial(\rho u)}{\partial x} + \frac{\partial(\rho v)}{\partial y} + \frac{\partial(\rho w)}{\partial z} = 0 \quad (26)$$

$$\frac{\partial(\rho u)}{\partial t} + \frac{\partial(\rho u^2)}{\partial x} + \frac{\partial(\rho v u)}{\partial y} + \frac{\partial(\rho w u)}{\partial z} = -\frac{\partial p}{\partial x} + \frac{1}{\text{Re}} \left(\frac{\partial \tau_{xx}}{\partial x} + \frac{\partial \tau_{xy}}{\partial y} + \frac{\partial \tau_{xz}}{\partial z} \right) \quad (27)$$

Where ρ is the density of the fluid [kg/m³], u, v, w are the velocities of the fluid along x, y, z [m/s], wall stress along x, y, z, [Pa], Re is the Reynold number [-]

6.1.1 Model description

For the CDF analysis, only the Pb-15.7Li volume is considered, neglecting the cover gas, considering the steady state conditions. In Figure 55, the modelled domain is shown. It has been implemented as a 2D geometry to simplify the simulations. This type of simplification is possible because the motion of the fluid is vertical from the bottom to the top, so it is possible to neglect the component of the third dimension.

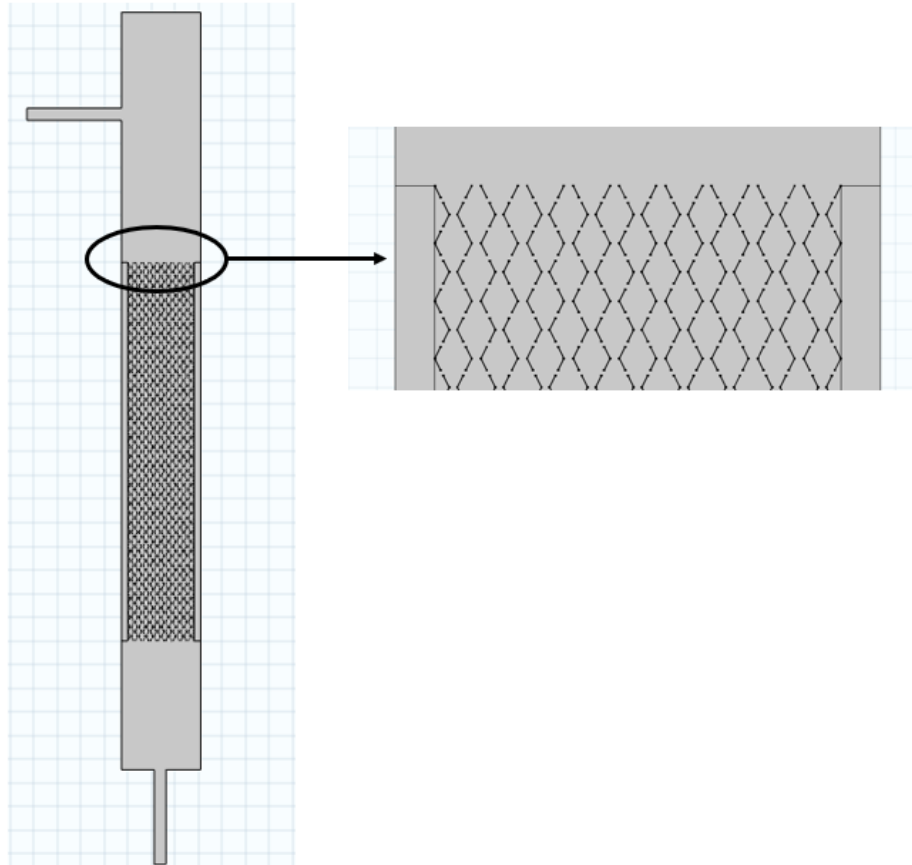


Figure 55 – Implemented domain for the extractor, in the zoom there is a structured filling.

6.1.2 Initial and boundary conditions

As an initial condition, the inlet velocity was set in Table 35. It derived from the flow rate of TRIEX-II. The fluid is considered isothermal and also gravity force acting along the length of the domain was imposed.

Initial conditions	Values
Temperature	673 [K]
Inlet velocity	0.13 [m/s]

Table 35 – Initial conditions values.

The boundary conditions are reported in Table 36.

Boundary conditions	Values
Outlet pressure	1.47 [barg]
Inlet velocity	0.13 [m/s]

Table 36 – Boundary conditions.

6.1.3 Mesh

In this paragraph, the details on the mesh construction will be described. First of all the size of the first cell near the wall must be calculated, which is calculated using the following formula:

$$\Delta y = \frac{y^+ \mu}{\rho U_T} \quad (28)$$

where y^+ is the distance from the wall [-], calculated in function of the viscosity, μ is the viscosity of the fluid [$Pa \cdot s$], ρ is the density of the fluid [kg/m^3], and U_t is the velocity of the fluid [m/s].

For the performed simulations, y^+ must be between 0 and 100, to calculate Δy an intermediate value of y^+ of 50 has been taken. The main parameters for the evaluation of Δy are reported in Table 37.

μ	Y^+	ρ	U_T
0.013	50	9720	0.16

Table 37 – Chosen parameters for the estimation of Δy .

The dimension of the first cell is = 0.00066 [mm]. Once the first cell size has been calculated, then the mesh can be calculated as a function of the latter. The mapped mesh and tetrahedral meshes (Figure 56) are used to construct them. The mapped mesh is used to simulate the extractor parts where the structured packing is not present, instead, the region near the structured packing has meshed with a tetrahedral mesh. For the mapped and tetrahedral mesh, a greater thickening is done near the wall.

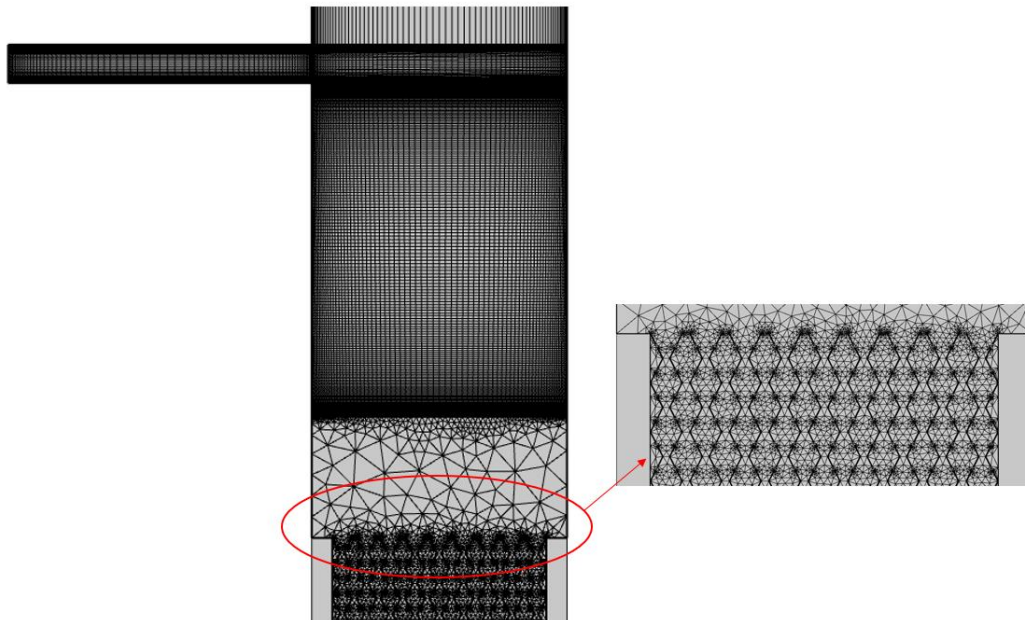


Figure 56 – Mesh zoom of the extractor.

Additional considered issues to construct correctly the mesh are:

- 1) Avoid high skewed cells, $40^\circ < \alpha_s < 140^\circ$ to prevent numerical instability: the skewed angle is $> 140^\circ$;

It is possible to calculate with the following formula

$$\theta_{sk} = \max \left[\frac{\theta_{\max} - \theta_e}{180 - \theta_e}, \frac{\theta_e - \theta_{\min}}{\theta_e} \right]$$

Where θ_e angle for an equiangular face/cell = 60, θ_{\max} is largest angle in the face or cell, θ_{\min} is smallest angle in the face or cell [41].

θ_e [deg]	θ_{\max} [deg]	θ_{\min} [deg]
60	82	0

Table 38 – Main values for the skewed angle

- 2) Avoid the warped cells: the warped cells are $\alpha < 75^\circ$;
- 3) Avoid non-orthogonal cells near the boundaries: there are not non-orthogonal cells near the boundary thanks to the triangulation of Delaunay;
- 4) Avoid the tetrahedral elements: there are not tetrahedral elements in boundary layers: because the simulation is 2D;
- 5) Avoid the discontinues there is not a presence of arbitrary mesh coupling because COMSOL imposes an algorithm to avoid this problem;
- 6) Avoid the presence of arbitrary mesh coupling: directly avoided by pre-set algorithm on COMSOL Multiphysics.

6.1.4 Grid independence

The best practices guidelines are used for the mesh selection [42].

The grid independence analysis is based on the approach developed by Roache and consists of six steps:

- 1) Definition of the representative cell for 2D calculations.

$$h = \left[\frac{1}{N} \sum_{i=1}^N \Delta S \right]^{\frac{1}{3}} \quad (29)$$

where ΔS is the surface of the i-th cell equal to $= 0.2519 \text{ m}^2$, and N is the total number of cells used in the simulation.

- 2) Selection of three significantly different sets of the grid.

The grid refinement factor is defined as:

$$r = \frac{h_{\text{corse}}}{h_{\text{fine}}} \quad (30)$$

For the grid independent analysis three different simulations are chosen respectively with 216842, 125038 and 107776 number of elements.

- 3) Evaluation of the apparent order of the method. Assumed that $h_1 < h_2 < h_3$ and $r_{21} = \frac{h_2}{h_1}$, $r_{32} = \frac{h_3}{h_2}$, the order is evaluated by the implicit equation:

$$p = \frac{1}{\ln r_{21}} \cdot \left| \ln \left| \frac{\varepsilon_{32}}{\varepsilon_{21}} \right| + \ln \frac{r_{21}^p - \text{sign} \left(\frac{\varepsilon_{32}}{\varepsilon_{21}} \right)}{r_{32}^p - \text{sign} \left(\frac{\varepsilon_{32}}{\varepsilon_{21}} \right)} \right| \quad (31)$$

Where $\varepsilon_{32} = \phi_3 - \phi_2$, $\varepsilon_{21} = \phi_2 - \phi_1$ and ϕ_k denotes the solution of interest on the k-th grid. As an initial guess, the term ε_{32} can be assumed. The ε_{32} , ε_{21} are calculated taking average speed and point speed at the inlet and at the outlet.

4) Calculated the extrapolated values as:

$$\phi_{\text{ext}}^{21} = (r_{21}^p \phi_1 - \phi_2) / (r_{21}^p - 1) \quad (32)$$

$$\phi_{\text{ext}}^{32} = (r_{32}^p \phi_3 - \phi_2) / (r_{32}^p - 1) \quad (33)$$

5) Calculation of the error:

$$e_a^{21} = \left| 1 - \frac{\phi_2}{\phi_1} \right| \quad (34)$$

$$e_{\text{ext}}^{21} = \left| 1 - \frac{\phi_1}{\phi_{\text{ext}}^{21}} \right| \quad (35)$$

which are the approximate relative error and the extrapolated error.

6) Grid Convergence Index (GCI) calculation:

$$\text{GCI} = \frac{1.25 e_a^{21}}{r_{21}^p - 1} \quad (36)$$

Two types of the variable were considered for the calculation of the grid convergence index, one local type, and one global type. For the local type was taken punctual speed, in the center of the tube, instead of for the global variable was taken the average speed in a line, the line must not be near the entry because the motion of the fluid must be fully developed. The GCI index for the two variables is reported in Figure 57, while the values of the local velocity and the surface average velocity are reported in Figure 58.

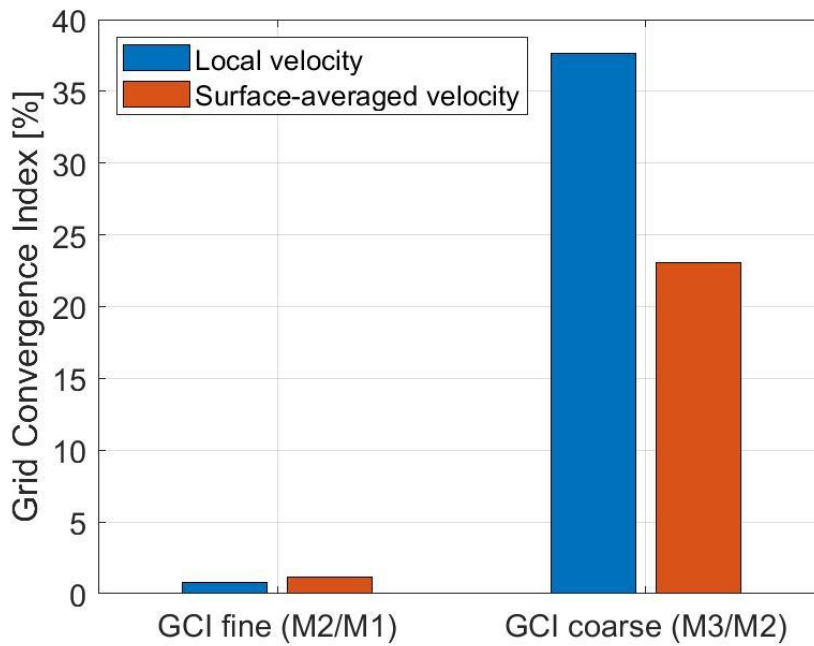


Figure 57 – Grid convergence index.

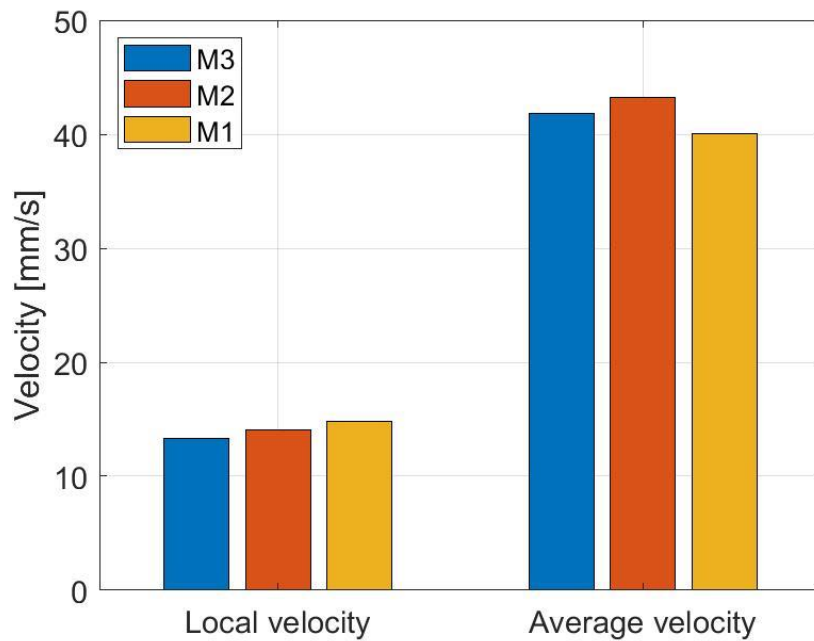


Figure 58 – Speed calculated with different meshes.

Against the previous analysis, the optimal mesh for the simulations is the M2 mesh, because despite being worse than the M1, it guarantees a good accuracy, saving on computational cost.

6.1.5 Validation of CFD model

For the validation of CFD simulations, the values of pressure drop detected on 30 April 2019 (Table 39), thanks to the differential pressure transducer positioned on the extractor, were considered. For the experiment, the gas injection line and the bypass valve PV601 were closed, while the PV601 valve was fully open. The flow rate of Pb-15.7Li has been changed by varying the number of revolutions of the pump from 0 to 654 [rpm] with a permanent pump.

L [kg/s]	DPT712 [barg]	T _{Pb-Li} [°C]
0	0	400
0,68	0	400
1,15	0	400
1,55	0	400
1,9	0	398
2,55	0,01	398
3,1	0,02	398
3,54	0,03	398
4,02	0,05	398
4,25	0,09	398

Table 39 – Test matrix for the characterization of the extractor.

For a value of Pb-15.7Li the mass flow rate lower than 2 [kg/s], the pressure drop is negligible, and for higher values, the pressure drop is up to 0.09 [barg] for the mass flow rate of 4.25 [kg/s] Figure 59.

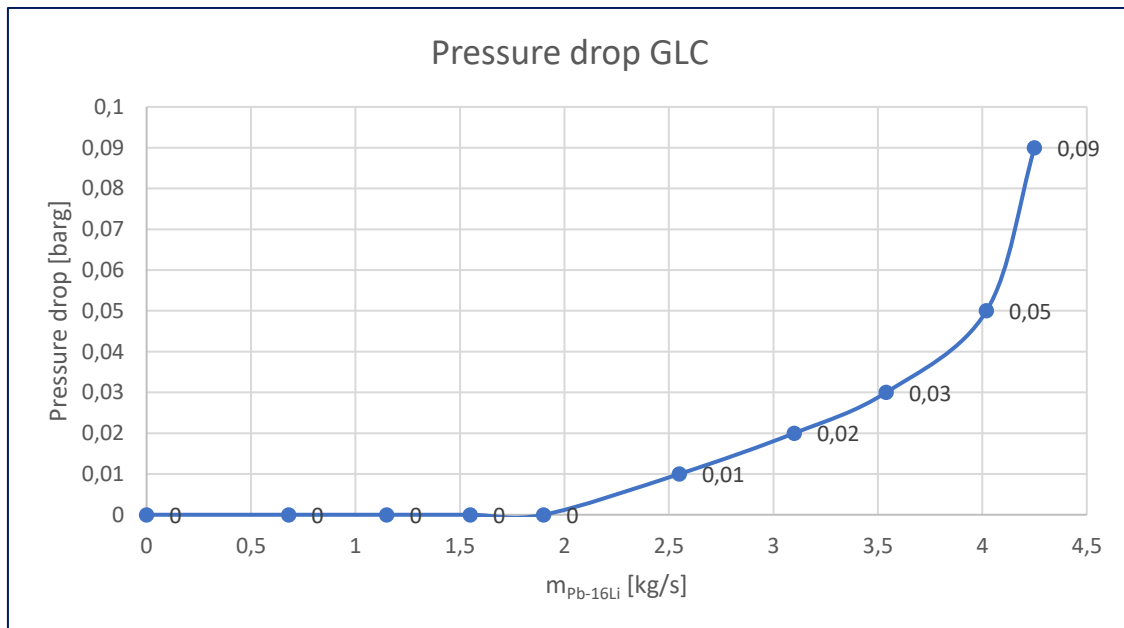


Figure 59 – Pressure drop trend of the extractor.

The relative error to compare the experimental tests (Figure 59) with the simulated values was estimated using the formula:

$$e_{rel} = 1 - \frac{\Delta p_{num}/p_0 + 1}{\Delta p_{mes}/p_0 + 1} \quad (37)$$

Where the numerical Δp is given by the difference between the pressure at the inlet and the outlet, subtracting the value of the hydrostatic door equal to 1.47 [barg], the p_0 is the atmospheric pressure equal to 1.01325 [bar].

The Δp measured, Δp theoretical and the estimated relative error are reported in Table 40.

Pb-15.7Li mass flow	Δp measured [barg]	Δp theoretical [barg]	Relative error [%]
0.68	0	0.05	4.98
1.55	0	0.028	2.79
2.55	0.01	0.016	2.58
3.1	0.02	0.049	6.71
4.25	0.09	0.19	25.07

Table 40 – Comparison between the simulation and experiment.

The pressure drop is reported in Figure 60, with the relative errors respect to the simulation one.

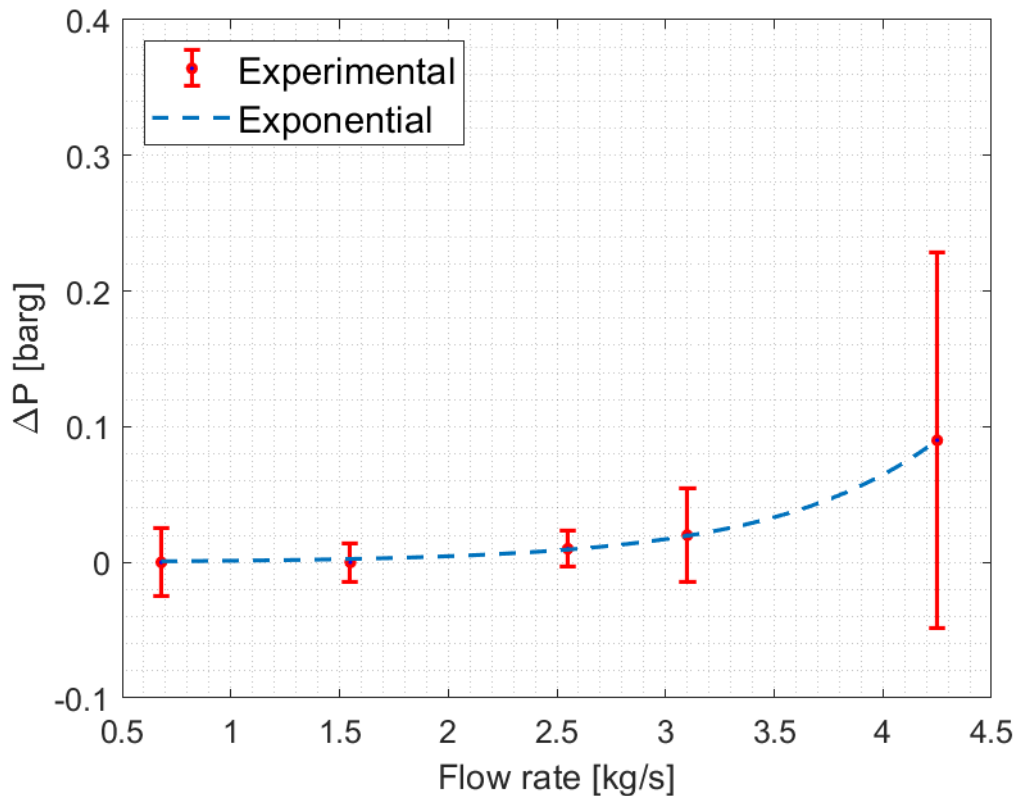


Figure 60 – Validation of the simulation.

The simulation has an error less than 7 [%] for the flow rate up to 3.15 [kg/s], while for higher mass flow rate the error increase up to 25 [%] for the flow rate of 4,25 [kg/s].

This increase of the error may be due to a too strong approximation of the set geometry and to the considerable complexity of the structured filling.

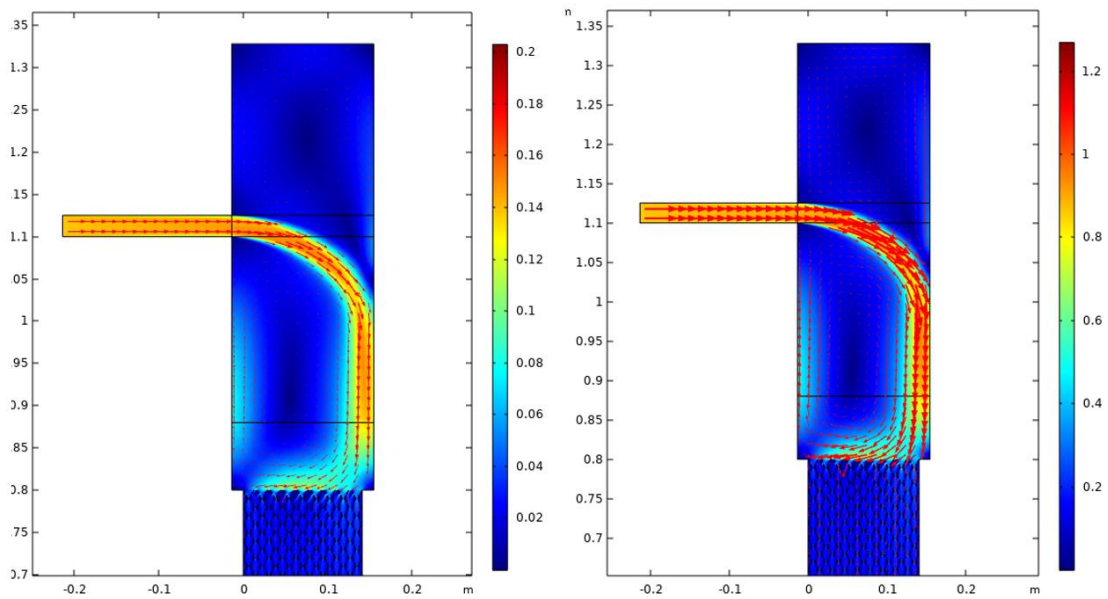


Figure 61 – Velocity field at the inlet [m/s]: on the left $L=0.68$ kg/s, on the right $L = 4.25$ kg/s.

the velocity profile of the liquid metal for the flow rate of 0.68 and 4.25 [kg/s] at the inlet is reported in Figure 61.

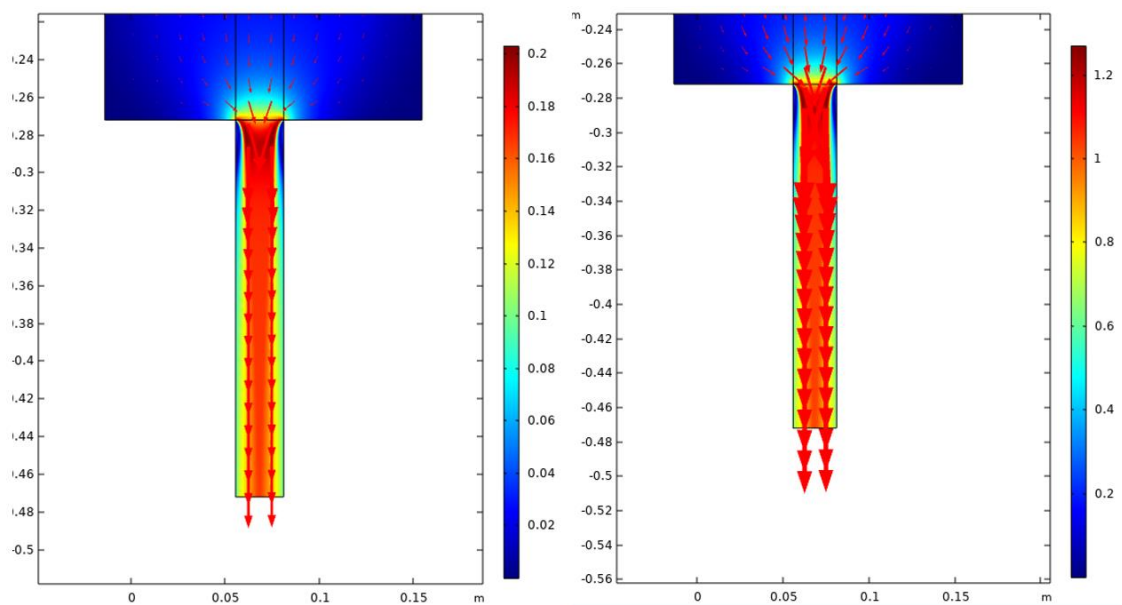


Figure 62 – Velocity field at the outlet [m/s]: on the left $L=0.68$ kg/s, on the right $L = 4.25$ kg/s.

The velocity profile of the liquid metal for the flow rate of 0.68 and 4.25 [kg/s] at the outlet of the extractor is reported in Figure 62.

6.2 Transport analysis

A transport model to evaluate the saturation and extraction times of the hydrogen, not only inside Pb-15.7Li but also inside the vessel and the packing filling, has been developed.

The velocity field calculated with the simulation CFD has been implemented in the simulation of the transport.

6.2.1 Transport model description of the extractor and the saturator

Both the saturator and the extractor work in equilibrium mode. In the saturator, the concentration of hydrogen inside the: Pb-15.7Li, vessel and packed filling at $t = 0$ is zero. For the extractor, the concentration of hydrogen in the Pb-15.7Li, vessel and the packed tower is equal to the square root of the equilibrium pressure multiplied by its Sieverts' constant.

The whole domain is assumed as 2D-axisymmetric to simplify the simulations Figure 63.

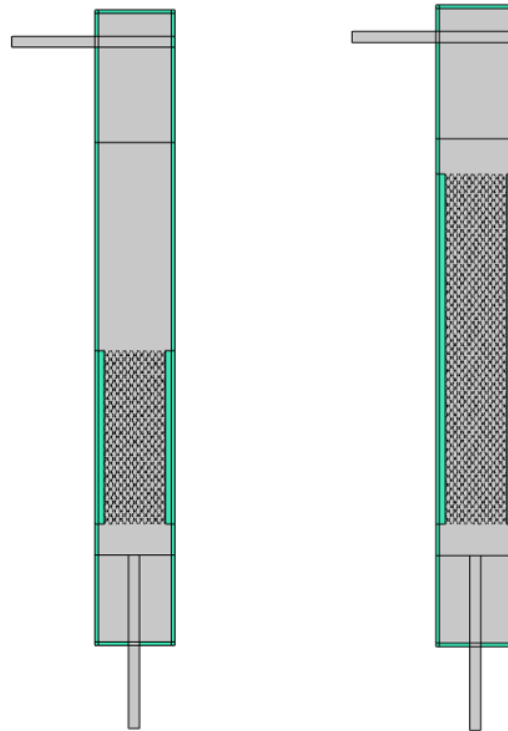


Figure 63 – Geometry of the saturator on the left and of the extractor on the right.

This model has posed a grave difficulty, how to represent a source or a well since because of the nature of the COMSOL Multiphysics software because it is impossible to create a multiphase simulation within the same domain.

A multilateral solution has been adopted to solve this problem: the creation of a source of shaft fictitious. This was possible by identifying a function depending on time and space $S(y, t) = f(t) * g(y)$.

The $f(t)$ was calculated using a Simulink 0-D model, where it was to identify a function that describes the evolution in time of both the extractor and the saturator phase.

$$f(t) = 10^{-5} \exp(-0.0004t) \quad (38)$$

For $g(y)$, a decreasing exponential function has been taken, with domain between 0 – 40 [mm] for saturator and between 0 – 80 [mm] for the extractor, where the two domains represent the structured filling domain.

$g(y)$ can be written as:

$$g(y) = \exp(-y/80) \quad (39)$$

A passive scalar transport equation can be written for the hydrogen species:

$$\frac{\partial c_i}{\partial t} = \nabla(D_i \nabla c_i) - \vec{u} \nabla c + S_i \quad (40)$$

where c_i [mol/m³] is the concentration in the i -th domain (Pb-15.7Li, α -iron, hydrogen gas), D_i [m²/s] is the diffusivity, \vec{u} [m/s] is the velocity and S_i [mol/(m³s)] is the source term. In this case, $\vec{u} = 0$ and $S_i = 0$, so the equation for each domain becomes:

$$\frac{\partial c_{H,PbLi}}{\partial t} = \nabla(D_{H,PbLi} \nabla c_{H,PbLi}) \quad (41)$$

$$\frac{\partial c_{H,316L}}{\partial t} = \nabla(D_{H,316L} \nabla c_{H,316L}) \quad (42)$$

$$\frac{\partial c_{H,EF}}{\partial t} = \nabla(D_{H,EF} \nabla c_{H,EF}) \quad (43)$$

$$\frac{\partial c_{H_2,H_2}}{\partial t} = \nabla(D_{H_2,H_2} \nabla c_{H_2,H_2}) \quad (44)$$

Hydrogen is monoatomic in solution with the metals and it recombines on the iron surface in contact with the vacuum side.

The solubility of hydrogen in metals obeys the Sieverts' law for the Pb-15.7Li, Eurofer, and for 316L.

$$c_{H,PbLi} = K_s \sqrt{p_{H_2}} \quad (45)$$

$$c_{H,EF} = K_s \sqrt{p_{H_2}} \quad (46)$$

$$c_{H,316L} = K_s \sqrt{p_{H_2}} \quad (47)$$

where $c_{H,PbLi}$ [mol/m³] is the concentration of hydrogen in the metal, K_s [mol/(m³ Pa^{0.5})] is the Sieverts' constant and p_{H_2} [Pa] is the partial pressure of hydrogen in the metal.

The net flux of hydrogen at 317_L/gas interface and the flux of hydrogen at 317_{EF}/gas interface can be written:

$$J_{H/316L} = 0 \quad (48)$$

$$J_{H/EU} = 0 \quad (49)$$

where J_H [mol/(m² s)] is the net flux of monoatomic hydrogen, K_{dH_2} [mol/(m² s Pa)] is the dissociation constant, p_{H_2} [Pa] is the pressure of hydrogen in the gas phase, K_{rH_2} [m⁴/(mol s)] is the recombination constant, $c_{H,Fe}$ [mol/m³] is the

concentration of hydrogen in iron at the boundary

The flux conditions are implemented directly by COMSOL-Multiphysics.

To solve the diffusion equation, the diffusivity of hydrogen in the different materials is needed.

6.2.2 Initial conditions

For the saturator at $t=0$ Pb-15.7 is saturated with hydrogen, and the concentration can be evaluated from Sieverts' law. Instead, the concentration is equal to zero inside the structured filling and in the vessel.

For the extractor, all the inventories are saturated at a certain concentration that can be evaluated with the Sieverts' law.

6.2.3 Boundary conditions

At the interface of Pb-15.7Li/316L and of Pb-15.7/EF, a pressure continuity condition between hydrogen in Pb-15.7Li and hydrogen in iron is imposed and it can be written as follows [1]:

$$\frac{C_{H,316L}}{C_{H,PbLi}} = \frac{K_{S,316L}}{K_{S,PbLi}} = K_{316L} \quad (50)$$

$$\frac{C_{H,EF}}{C_{H,PbLi}} = \frac{K_{S,EF}}{K_{S,PbLi}} = K_{EF} \quad (51)$$

In this way, a partition coefficient $K [-]$ is defined as the concentration of hydrogen in Eurofer divided the concentration of hydrogen in Pb-15.7Li, and the concentration of hydrogen in 316L divided the concentration of hydrogen in Pb-15.7Li.

The net flux of hydrogen at 316L/gas interface and the net flux of hydrogen at EU/gas interface can be written:

$$J_H = K_{d,H_2} p_{H_2} - K_{r_{316L},H} c_H^2 \quad (52)$$

$$J_H = 0 \quad (53)$$

$$J_H = K_{d,H_2} p_{H_2} - K_{r_{EU},H} c_H^2 \quad (54)$$

$$J_H = 0 \quad (55)$$

where J_H [mol/(m² s)] is the net flux of monoatomic hydrogen, K_{d,H_2} [mol/(m² s Pa)] is the dissociation constant, p_{H_2} [Pa] is the pressure of hydrogen in the gas phase, $c_{H,Fe}$ [mol/m³] is the concentration of hydrogen in in 316L and in EU at the boundary.

6.2.4 Validation of tritium transport model

For the validation of transport simulations, the values of Pb-15.7Li has detected thanks to the permeation sensors positioned on TRIEX-II. To validate the simulation, two experiments have been taken into account: the experiment of 30th April 2019 for the saturator, and the experiment of 18th – 19th April 2019 for the extractor. The two partial pressures of hydrogen are measured with the permeation sensor HLM 734.

- **Saturator**

To validate the simulation of the saturator, three types of errors are taken into account, the response time error, the integral error, and the accuracy error, the formula for calculating them are given in 5.4. In Figure 64, there is a comparison between the theoretical trend with the experimental trend, while the three errors are reported in Table 41 Note that the three calculated errors . just above 10 [%], this means that the numerical model is able to faithfully represent the physics of the extractor.

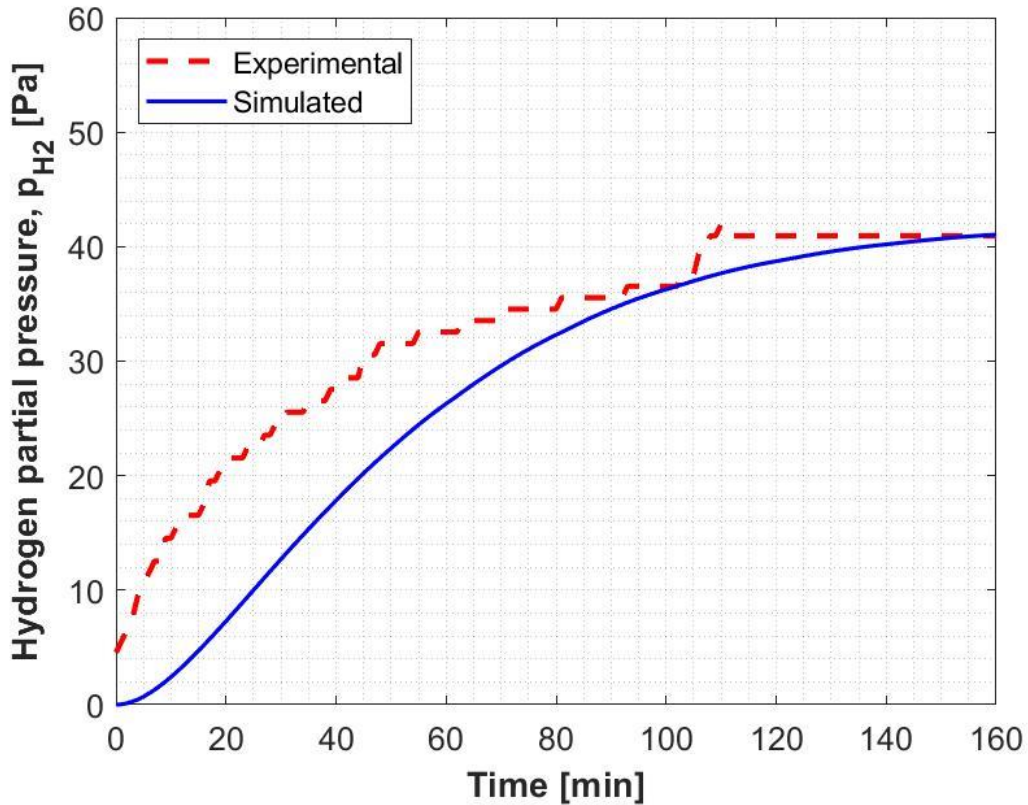


Figure 64 – Validation of the saturator.

ϵ_t [%]	ϵ_{int} [%]	ϵ_{acc} [%]
8	11	0.2

Table 41 – Errors results.

The trend of the partial pressure of the hydrogen in the vessel, packed filling and the PL-15.7Li is reported in Figure 65. As noted by the trend Experimental, the model manages to approximate well (the highest error is 10 [%]), the behaviour of the pb-Li, therefore it can be affirmed that even without experimental data, the trend in figure is coherent with real trend.

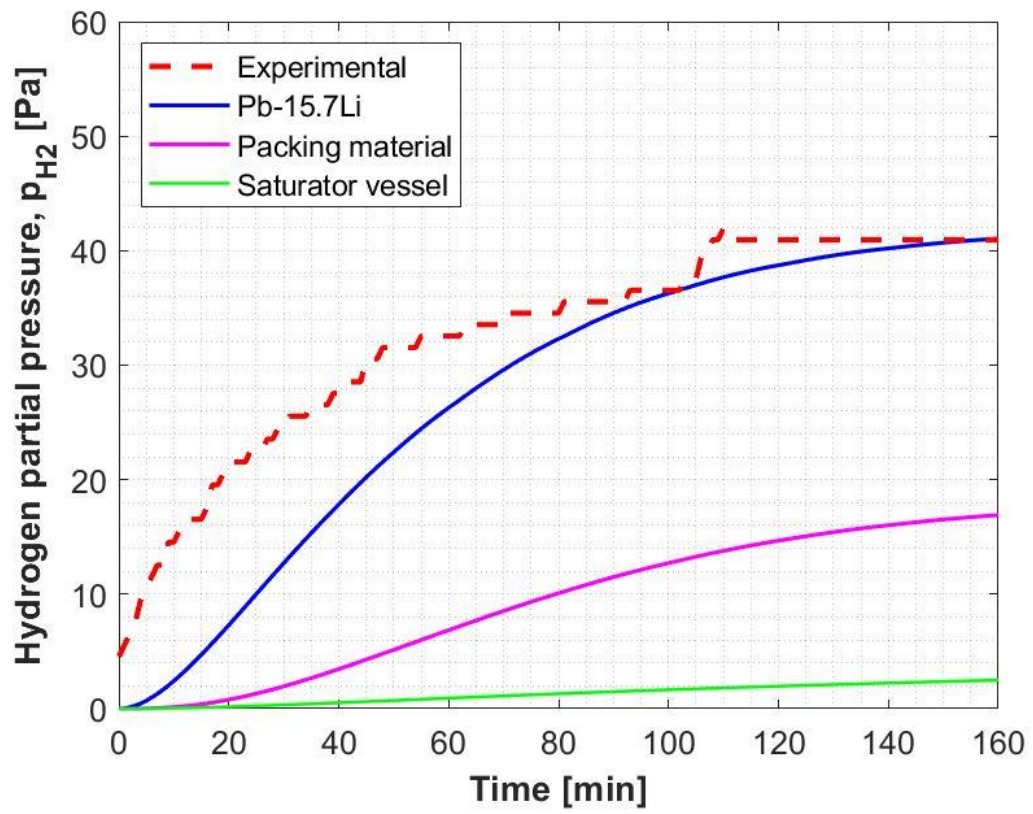


Figure 65 – All inventory of the Saturator.

- **Extractor**

Concerning the extractor, the time period in which the hydrogen pressure inside the Pb-15.7Li is stable for both the simulation and the experimental phase has been considered. The error between the two curves is calculated using the accuracy error and is equal to 12 [%].

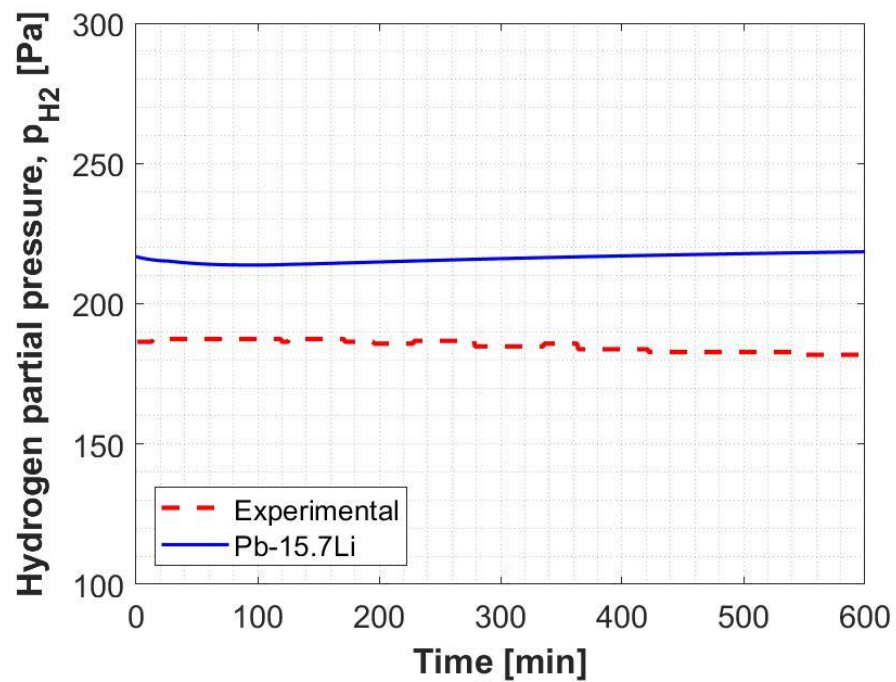


Figure 66 – Validation of the extractor.

The partial pressure of the simulation and the extractor are in Figure 66.

Conclusion

In the framework of fusion technologies, two main projects are under development for the design, manufacturing and qualification of a thermonuclear power plant: ITER (International Thermonuclear Experimental Reactor) and DEMO (DEMONstrating fusion power reactor). ITER is a nuclear fusion reactor devoted to study fusion from a physical and engineering point of view. DEMO will be ITER successor, and its key criterium is the production of electricity. In ITER it will be qualified four different Test Blanket Modules devoted to remove the heating power generated in the fusion reaction and to generate the tritium required in the fusion process. In DEMO reactor the two breeder Blanket concepts will be qualified, WCLL and HCPB BB. In particular, in Europe the Helium-Cooled Pebble Beds and the Water-Cooled Lithium-Lead Test Blanket Modules concepts (HCPB-TBM and WCLL-TBM) will be tested in ITER in order to characterise the tritium breeding and removal processes. One of the peculiarities of the WCLL TBM is the use of lithium-lead eutectic alloy, with the function of tritium breeder, neutron multiplier and tritium carrier. Once tritium has been produced, it must be extracted and purified in order to be used as a fuel. For this reason, tritium extraction systems play a key role. To fulfil this function, various technologies are being studied, such as Gas-Liquid Contactors (GLC).

In this context, this thesis has been developed focusing on the modelling and the qualification of a GLC mock-up for WCLL TBM of ITER. From this point of view, an experimental facility, TRIEX-II, has been built in ENEA C. R. Brasimone in 2018-2019 to qualify the GLC technology and the experimental campaign has been carried out and followed from January to mid-June 2019.

Two main aspects have been analysed in this work: a suitable way to measure hydrogen concentration in lithium-lead and the characterization of a GLC packed column in terms of extraction efficiency.

Concerning the way to measure hydrogen concentration in lithium-lead, permeation sensors, which were previously designed and qualified in a dedicated test facility, have been installed in TRIEX-II. Meanwhile, a model of the permeation sensors, dedicated to investigate different operational conditions and configurations, has been implemented. The main influencing parameters on the time to reach 90 % of the equilibrium pressure by the sensors are: the surface to volume ratio, Sieverts' constant and the wall membrane thickness. The first one is the most influencing parameter, in fact increasing the S/V, the contact surface will increase, and the hydrogen permeation surface will increase, giving the sensor a faster response time. For this reason, the helical sensor configuration has been chosen in the TRIEX-II facility rather than the cylindrical configuration as for TRIEX. As far as the Sieverts' constant is concerned, the different reached equilibrium times depend on the uncertainty of this parameter, that can change by two orders of magnitude. The last influencing parameter is the thickness of the membrane. Increasing the thickness of the sensor walls, the time to reach 90% of the equilibrium pressure increases, because the hydrogen will have to diffuse in a bigger thickness.

Concerning the GLC mock-up, it has been tested in two different operational modes: the operational mode with hydrogen, where hydrogen was firstly solubilized in the liquid alloy by means of a saturator column and then extracted in the mock-up by using helium as stripping gas, and the operational mode with deuterium, where deuterium was solubilized and a mixture of helium and hydrogen was used as a stripping gas. In this frame, 2D numerical models of saturator and extractor have been implemented. The CFD

analysis has been implemented to study the pressure drops and the velocity profiles. This analysis has produced results that are able to represent the fluid-dynamics of both the saturator and the extractor. In particular, regarding the extractor, it has been found that the pressure drops are almost negligible for lithium-lead mass flow rate lower than 2 kg/s, whereas they present an exponentially increasing behaviour for higher mass flow rates. This kind of behaviour has been validated with the experimental tests, with errors below 7% with the exception of the highest values of flow rate, where the error was about 25%. This increase of the error is probably correlated to the development of a 2D model, implementing a 3D CFD model a more precise representation should be achieved. Secondly, the transport model has been set up in order to assess the time and concentrations of hydrogen that are extracted or saturated. Finally, the validation between numerical and experimental data has been performed. Concerning the saturator, the maximum estimated error reaches 11 %. The agreement between numerical and experimental results is good. As far as the extractor is concerned, the time period in which the hydrogen pressure inside the Pb-15.7Li is stable for both the simulation and the experimental phase has been considered. The error has been calculated and is equal to 12 %.

The model of the saturator and extractor has been assessed in order to be used as a part of an integrated model, to be used by ENEA, so as to simulate the whole TRIEX-II system and to address the overall mass balance.

Bibliography

- [1] J.Freidberg, *Plasma Physics and Fusion Energy*, Springer, 2007.
- [2] Mondadori Scienza S.p.A., [Online]. Available: <https://www.focus.it/scienza/scienze/stellarator-e-fusione-nucleare>. [Accessed 5 July 2019].
- [3] N.Mitchell, "The ITER magnet system: configuration and conclusion status," *Fusion Engineering and Design*, vol. 123, pp. 17-25, 2017.
- [4] B.E.Nelson and A.Brooks, *Engineering Aspects of Compact Stellarators*, IAEA.
- [5] IPP Max Plank Institute for Plasma Physics, Max-Planck-Gesellschaft, [Online]. Available: <https://www.ipp.mpg.de/14824/magnetspulen>. [Accessed 9 July 2019].
- [6] Max-Planck Institute, "Max-Planck-Gesellschaft," [Online]. Available: <https://www.ipp.mpg.de/16931/einfuehrung>. [Accessed 2 July 2019].
- [7] P.E.Moroz, "Stellarator-spheromak," *PHYSICS LETTERS A*, vol. 236, pp. 79-83, 1997.
- [8] A.Raeisdana, "Computation of Mass Sweeping Efficiency Factor and Current Efficiency Factor in Z-pinch Devices," *Journal of Fusion Energy*, vol. 30, pp. 130-132, 2011.
- [9] S.Bathgate and M.M.M.Bilek, *Electrodeless plasma thrusters for spacecraft: A review*, IOP Publishing, 2017.
- [10] S.H.Glenzer and B.J.MacGowan, "Symmetric Inertial Confinement Fusion Implosions at Ultra-Higt Laser Energies," *Science*, vol. 327, pp. 1228-1231, 2010.
- [11] iter, "ITER ORGANIZATION," 2019. [Online]. Available: <https://www.iter.org/Glossary#69>. [Accessed 4 July 2019].
- [12] G.Federici and L.Boccaccini, "AnoverviewoftheEUbreedingblanketdesignstrategyasanintegralpart oftheDEMOfdesigneffor," *Fusion Engineering and Design*, vol. 141, pp. 30-42, 2019.
- [13] C. a. P.E.Stott, *Nuclear Fusion: Half a Century of Magnetic Confinement Fusion Research*, CRC Press, 2002.
- [14] M.Loughlin, "Status and verification strategy for ITER neutronics," *Fusion Engineering and Design*, vol. 89, pp. 1865-1869, 2014.
- [15] M. Merola, "Overview and status of ITER internal components," *Fusion Engineering and Design*, vol. 89, pp. 890-895, 2014.
- [16] K.Tobita, S.Nischo and M.Sakururai, "SlimCS—compactlowaspectratioDEMO reactor with reduced-size central solenoid," *Nuclear Fusion*, vol. 47, pp. 892-899, 2007.

- [17] G.Federici and R.Kemp, "Overview of EU DEMO design and R&D activities," *Fusion Engineering and Design*, vol. 89, pp. 82-889, 2014.
- [18] H.Zhang, *Modeling and Analysis of Tritium Transport in Multi-Region Lead-Lithium Liquid Metal Blankets*, Los Angeles : UCLA Electronic Theses and Dissertations , 2014.
- [19] M.Glugla, R.Lässer, L.Dörr and D.K.Murdoch, "The inner deuterium/tritium fuel cycle of ITER," *Fusion Engineering and Design*, vol. 69, pp. 39-43, 2003.
- [20] PhysicsOpenLab, 2019. [Online]. Available: <http://physicsopenlab.org/2016/02/07/trizio/>. [Accessed 5 July 2019].
- [21] U.Jauch and G.Haase, *Thermophysical Properties in the System Li-Pb*, Kernforschungszentrum Karlsruhe, 1986.
- [22] B.Gargiuño, D.Rapisarda and I.Fernández, "Design of a permeator against vacuum for tritium extraction from eutectic lithium-lead in a DCLL DEMO," *Fusion Engineering and Design*, vol. 117, pp. 226-231, 2017.
- [23] E. Martelli, *Thermal hydraulic design of DEMO Water Cooled Lithium Lead Breeding Blanket and integration with primary system and balance of plant*, Roma, 2018.
- [24] L.V.Boccaccini, G.Aiello and J.Aubert, "Objective and status of EUROfusion DEMO blanket studies," *Fusion Engineering and Design*, Vols. 109-111, pp. 1199-1206, 2016.
- [25] R.Perry and D.Green, *Perry's Chemical Engineers' Handbook*, 8th ed, McGraw-Hill, 2007.
- [26] V.D'auria, S.Dulla, P.Ravetto, L.savoldi and M.Utili, "Tritium Extraction from Lithium-Lead in the EU DEMO Blanket Using Permeator Against Vacuum," *Fusion Science and Technology*, vol. 71, pp. 537-543, 2017.
- [27] MediaWiki, "world Encyclopedia," 13 December 2018. [Online]. Available: https://www.newworldencyclopedia.org/entry/Nuclear_fusion. [Accessed 2 June 2019].
- [28] E.G.Gaddis, "Mass transfer in gas-liquid contactors," *Chemical Engineering and Processing*, vol. 38, pp. 503-510, 1999.
- [29] N.Kantarci, F.Borak and K.O.Ulgen, "Bubble column reactors," *Process Biochemistry*, vol. 40, pp. 2263-2283, 2004.
- [30] M.Götz, J.Lefebvre, F.Mörs and F.Ortloff, "Novel gas holdup correlation for slurry bubble column reactors operated in the homogeneous regime," *Chemical Engineering Journal*, vol. 308, pp. 1209-1224, 2017.
- [31] BOEGGER, "BOEGGER Industrial Limited," [Online]. Available: <https://www.demisterpads.com/demister-pad/packed-tower.html>. [Accessed 6 July 2019].

- [32] M.Utili, A.Aiello, L.Laffi and A.Malavasi, "Investigation on efficiency of gas liquid contactor used as tritium extraction unit for HCLL-TBM Pb-16Li loop," *Fusion Engineering and Design*, vol. 109, pp. 1-6, 2016.
- [33] j.f.Richardson, J.H.Haker and j.R.Backhurst, *Separation Columns (Distillation, Absorption and Extraction)*, Butterworth-Heinemann, 2002.
- [34] M.Utili, M.Kordac, A.Venturini and L.Candido, "Deliverable: D8 Seventh intermediate technical report," ENEA, Brasimone, 2019.
- [35] I.Di-Piazza, "HLM Thermal flow meters supply," ENEA, Brasimone, 2017.
- [36] TEAM ELCO, Elco Elettronica srl, 2019. [Online]. Available: <https://www.elcoteam.com/privati/fluke-86pk-ext.html>. [Accessed 4 July 2019].
- [37] M.Shimada and R.J.Pawelko, "Tritium permeability measurement in hydrogen-tritium system," *Fusion Engineering and Design*, vol. 129, pp. 134-139, 2018.
- [38] M.Utili, "Final Technical report," ANEA, Brasimone, 2019.
- [39] I.Ricapito, "PbLi/T database: status of the knowledge," IAE Workshop on PbLi-T, Idaho Falls, 2007.
- [40] J.H.Ferziger and M.Peric, *Computational Methods for Fluid Dynamics*, Stanford: Springer, 2002.
- [41] SAS IP, [Online]. Available: https://www.sharcnet.ca/Software/Ansys/17.0/en-us/help/wb_msh/msh_skewness.html. [Accessed 12 July 2019].
- [42] M.Casey and T.Wintergerste, *Best Practice Guidelines*, EUROFTAC, 2000.

DECLARATION

This thesis is a presentation of my original research work. The contributions of other others are involved, every effort is made to indicate this clearly, with the reference to the literature, and acknowledgement of collaborative research and discussion

Turin, July 2019